
Electronic Thesis and Dissertation Repository

6-11-2021 10:00 AM

Snapshot Three-Dimensional Surface Imaging With Multispectral Fringe Projection Profilometry

Parsa Omidi, *The University of Western Ontario*

Supervisor: Carson, Jeffrey, *The University of Western Ontario*

: Diop, Mamadou, *The University of Western Ontario*

A thesis submitted in partial fulfillment of the requirements for the Doctor of Philosophy degree in Biomedical Engineering

© Parsa Omidi 2021

Follow this and additional works at: <https://ir.lib.uwo.ca/etd>



Part of the [Bioimaging and Biomedical Optics Commons](#), [Biomedical Commons](#), [Biomedical Devices and Instrumentation Commons](#), and the [Signal Processing Commons](#)

Recommended Citation

Omidi, Parsa, "Snapshot Three-Dimensional Surface Imaging With Multispectral Fringe Projection Profilometry" (2021). *Electronic Thesis and Dissertation Repository*. 7852.
<https://ir.lib.uwo.ca/etd/7852>

This Dissertation/Thesis is brought to you for free and open access by Scholarship@Western. It has been accepted for inclusion in Electronic Thesis and Dissertation Repository by an authorized administrator of Scholarship@Western. For more information, please contact wlsadmin@uwo.ca.

Abstract

Fringe Projection Profilometry (FPP) is a popular method for non-contact optical surface measurements such as motion tracking. The technique derives 3D surface maps from phase maps estimated from the distortions of fringe patterns projected onto the surface of the object. To estimate surface profiles accurately, sequential acquisition of fringe patterns is required; however, sequential fringe projection and acquisition perform poorly if the object is in motion during the projection. To overcome this limitation, we developed a novel method of FPP named multispectral fringe projection profilometry (MFPP). The proposed method provides multispectral illumination patterns using a multispectral filter array (MFA) to generate multiple fringe patterns from a single illumination and capture the composite pattern using a single multispectral camera. Therefore, a single camera acquisition can provide multiple fringe patterns, and this directly increases the speed of imaging by a factor equal to the number of fringe patterns included in the composite pattern. Chapter 3 introduces this new technique and shows how it can be used to perform 3D profilometry at video frame rates. The first attempt at MFPP significantly improved acquisition speed by a factor of eight by providing eight different fringe patterns in four different directions, which permits the system to detect more morphological details. However, the phase retrieval algorithm used in this method was based on the spatial phase stepping process that had a few limitations, including high sensitive to the quality of the fringe patterns and being a global process, as it spreads the effect of the noisy pixels across the entire result. To overcome this limitation, Chapter 4 introduces an enhanced version of MFPP that utilized a specially designed multispectral illuminator to simultaneously project four $\pi/2$ phase-shifted fringe patterns onto an object. Combined with a spectrally matched multispectral camera, the refined MFPP method provided the needed data for the temporal phase retrieval algorithm using only a single camera exposure. Thus, it delivers high accuracy and pixel-wise measurement (thanks to the temporal phase stepping algorithms) while maintaining a high sampling rate for profilometry of moving objects. In conclusion, MFPP overcomes the limitations of sequential sampling imposed by FPP with temporal phase extraction without sacrificing data quality or accuracy of the reconstructed surface profiles. Since MFPP utilizes no moving parts and is

based on MEMS technology, it is applicable to miniaturization for use in mobile devices and may be useful for space-constrained applications such as robotic surgery.

Keywords

Fringe projection profilometry, off-axis digital holographic interferometry, phase retrieval algorithm, multispectral composite pattern, optical 3D surface measurement.

Summary for Lay Audience

Objects in our surroundings can be characterized as three-dimensional (3D) using the concepts of width, height, and depth. It is essential to quantify these dimensions for any system that attempts to represent our world in a realistic manner. Conventional cameras capture objects in two dimensions and generally do not sense depth. In contrast, a 3D camera lights the object with a beam of light shaped according to a known pattern and then infers the depth of the object from the changes in the light pattern. Generally, 3D cameras need to capture multiple camera snapshots to get enough data for a single 3D image. Therefore, they are not suitable for measuring fast-moving objects. During my Ph.D. research, I developed a new type of pattern generator that provides 3D cameras the ability to capture enough data for a 3D image from a single camera snapshot. The pattern generator uses a small filter to project multiple overlapping yet distinctive color patterns onto the object. The 3D camera incorporates a multispectral sensor that separates each distinctive color pattern. With this new technology, I was able to modify a 3D camera and measure fast-moving objects without motion blur. With further development, this new technology can be miniaturized for use in hand-held devices such as smartphones providing users a way to quickly measure the world around them in 3D.

Co-Authorship Statement

The thesis includes material from four publications, all of which had contributions from co-authors, as follows:

Chapter 2: Parsa Omid, Lawrence Yip, Hui Wang, Mamadou Diop, Jeffrey J.L. Carson, "PhaseWare: phase map retrieval for fringe projection profilometry and off-axis digital holographic interferometry," *SoftwareX*. (2021),13:100652.
doi:10.1016/j.softx.2020.100652.

My contributions to this chapter included designing the software architecture, developing algorithms, programming, simulating FPP data, and testing. I also analyze the results and wrote the scientific and technical concepts of this chapter. Lawrence Yip helped draft and edit the chapter. Hui Wang supplied the data for the off-axis DHI system. Dr. Diop read and edited this chapter and provided supervision. Dr. Carson helped design the software and analyze the numerical results. In addition, he read and edited the chapter, provided supervision, and provided fabrication and testing facilities at the Western University.

Chapter 3: Parsa Omid, Mohamadreza Najiminaini, Mamadou Diop, Jeffrey J.L. Carson, "Single-shot detection of 8 unique monochrome fringe patterns representing 4 distinct directions via multispectral fringe projection profilometry," *Scientific Reports*, 11, 10367 (2021).

My contributions included design and fabrication of the imaging setup. I also processed the data, analyzed the results, and wrote the chapter. Dr. Najiminaini designed and fabricated the MFA, provided the multispectral camera, and edited the chapter. The chapter was reviewed and edited by Dr. Diop, who also provided supervision. Dr. Carson provided the project concept and provided access to the fabrication and testing facilities at Western University. Dr. Carson edited and read the chapter and was the primary supervisor.

Chapter 4: Parsa Omid, Mohamadreza Najiminaini, Mamadou Diop, Jeffrey J.L. Carson, "Multispectral fringe projection profilometry for single-shot 3D surface imaging," Article submitted to *Journal of Optica*.

My contributions included design and fabrication of the imaging setup. I also processed the data, analyzed the results, and wrote the chapter. Dr. Najiminaini designed and fabricated the MFA, provided the multispectral camera, and edited the chapter. The chapter was reviewed and edited by Dr. Diop, who also provided supervision. Dr. Carson provided the project concept and access to the fabrication and testing facilities at Western University. Dr. Carson edited and read the chapter and served as the primary supervisor.

Chapter 5: Parsa Omid, Hui Wang, Mamadou Diop, Jeffrey J.L. Carson, “Algorithm for phase-displacement conversion from reflection digital holographic interferometry”. SPIE, (2019):25. doi:10.1117/12.2507566

My contributions to this chapter included developing the algorithms, analyzing the results, and writing the chapter. Hui Wang supplied the raw data. Dr. Diop reviewed and edited the chapter and provided advice. Dr. Carson provided conceptual design, access to fabrication and testing facilities at Western University. Dr. Carson read and edited the chapter and provided supervision.

Dedication

This thesis is dedicated to:

my parents, in loving memory;

my lovely wonderful wife, beloved family, and cherished friends; and

all of whom have always shown me unconditional love and support.

Acknowledgments

I would like to extend my sincere gratitude to my family for their continuous support and encouragement over the course of my Ph.D. The research I conducted would not have been possible without everyday support from my spouse, Samira Vakili.

My deepest gratitude goes out to my supervisor Dr. Jeffrey Carson, who taught me many essential scientific methods from the earliest stages of a research project to its completion. Without his guidance, patience, and his practical involvement in my research, I would not have been able to fulfill my Ph.D. I felt very privileged to work with Dr. Carson, and the experience really helped me see many opportunities in my current and future career. I am also grateful to my co-supervisor Dr. Mamadou Diop who provided me with his unlimited help, friendly encouragement, and professional assistance.

I would like to express my deepest appreciation to my committee members, Dr. Abass Samani and Dr. James Lacefield, for their positive encouragement, insightful comments, and thought-provoking questions. Thank you also, Dr. Nicole Ruitter, for giving me the opportunity to be a guest researcher in your groups and let me work on your exciting projects. Additionally, I enjoyed the chance to work with Dr. Kamran Avanaki and Dr. Hamid Behnam in the very beginning stages of my new research study. My first steps into biomedical imaging were assisted by them.

Special thanks to my great friend Dr. Mohamadreza Najiminaini for being such a fantastic mentor to me. I cannot forget all the kind support, valuable guidance, and lifesaver help that you have consistently provided, besides all of our “brainstorming” coffee times. I am grateful to Lawrence Yip, who has been a supportive friend and lab partner, and who has provided me with indispensable assistance. I also had the great pleasure of working with Dr. Astrid Chamson-Reig, Dr. Ivan Kosik, Hui Wang, and Elina Rascevska. Lastly, I would like to acknowledge the funding agencies NSERC and CIHR, and Lawson Health Research Institute for providing the financial support for this project.

Table of Contents

Abstract.....	ii
Summary for Lay Audience.....	v
Co-Authorship Statement	vi
Dedication	viii
Acknowledgments	ix
Table of Contents	x
List of Tables	xv
List of Figures.....	xvi
List of Appendices.....	xxiv
List of Acronyms and Glossary	xxv
Chapter 1	1
1 Introduction.....	1
1.1 Principle of fringe projection profilometry (FPP).....	3
1.1.1 Triangulation	4
1.2 Principle of off-axis digital holographic interferometry (DHI).....	5
1.2.1 Coherent light wave interference.....	7
1.2.1.1 Interference between two plane waves.....	7
1.2.1.2 Interference between a plane and a spherical wave	11
1.2.1.3 Interference between two spherical waves.....	12
1.2.2 Effect of scattering medium on interference fringe pattern	13
1.2.3 Reconstruction of the object beam	14
1.3 Fringe analysis	17
1.3.1 Phase retrieval	17
1.3.1.1 Spatial phase stepping.....	18
1.3.1.1.1 Fourier transform method	18
1.3.1.1.2 Wavelet transform method.....	22
1.3.1.1.3 Hilbert transform	24

1.3.1.2	Temporal phase stepping	26
1.3.2	Phase unwrapping.....	27
1.4	Applications.....	28
1.4.1	Static and quasi-static measurements	28
1.4.2	Dynamic measurements.....	29
1.4.2.1	Increasing the camera speed to capture the interferograms at fast frame rates	30
1.4.2.2	Capturing multiple interferograms in a single shot	30
1.4.2.3	Double-pulsed electronic speckle pattern interferometry (dp-ESPI)	31
1.5	Problem statement.....	31
1.6	Research objectives	32
1.7	Thesis outline	32
1.8	References	35
<i>Chapter 2</i>	<i>43</i>
2	PhaseWare: phase map retrieval for fringe projection profilometry and off-axis digital holographic interferometry	43
2.1	Abstract	43
2.2	Motivation and significance.....	43
2.3	Algorithms used in PhaseWare	44
2.3.1	Fringe projection profilometry	44
2.3.2	Off-axis digital holographic interferometry.....	46
2.4	Software description.....	47
2.4.1	Software architecture.....	48
2.5	Illustrative Examples.....	50
2.5.1	Fringe projection profilometry example	50
2.5.2	Off-axis digital holographic interferometry example	52
2.6	Impact.....	53
2.7	Conclusions	54
2.8	Conflict of Interest.....	55
2.9	Acknowledgements and funding sources.....	55
2.10	Code metadata	55

2.11	References	56
Chapter 3		59
3	Single-shot detection of 8 unique monochrome fringe patterns representing 4 distinct directions via multispectral fringe projection profilometry.....	59
3.1	Abstract	59
3.2	Introduction	60
3.3	Method.....	62
3.3.1	Fringe decomposition	63
3.3.2	Background and noise-free fringe generation.....	66
3.3.3	Fourier transform phase demodulation.....	68
3.3.4	Phase-to-height conversion.....	69
3.3.5	Post-processing.....	69
3.4	Results.....	70
3.5	Discussion	79
3.5.1	Major finding.....	79
3.5.2	Speed	79
3.5.3	Accuracy.....	80
3.5.4	Resolution.....	81
3.5.5	MFPP performance unaffected by object surface topography	82
3.5.6	MFPP mitigated degrading effects of glare	82
3.5.7	<i>MFPP has greater robustness to under sampling</i>	82
3.5.8	Limitations of this study	83
3.5.9	Implications for Future	83
3.6	Software.....	84
3.7	Acknowledgements	84
3.8	Conflict of interest	84
3.9	References	84
Chapter 4		90
4	Single-shot 4-step phase-shifting multispectral fringe projection profilometry	90
4.1	Abstract:.....	90
4.2	Introduction	90

4.3	Methods	93
4.3.1	Setup	93
4.3.2	Phase retrieval	94
4.4	Results.....	100
4.5	Discussion and conclusion.....	105
4.5.1	Overview	105
4.5.2	Major findings	105
4.5.3	Comparison to previous works	106
4.5.4	Procedure achievements	106
4.5.5	Limitations.....	107
4.5.6	Future works.....	107
4.6	Funding.....	107
4.7	Acknowledgments.....	107
4.8	Disclosures.....	108
4.9	References	108
Chapter 5		112
5	Algorithm for phase-displacement conversion from reflection digital holographic interferometry	112
5.1	Abstract	112
5.2	Introduction	113
5.3	Method and results	114
5.3.1	Digital holographic interferometry recording	114
5.3.2	Numerical reconstruction	115
5.4	Discussion and conclusion.....	123
5.5	References	124
Chapter 6		126
6	Summary.....	126
6.1	Overview.....	126
6.2	Contributions	126
6.2.1	Processing software	126

6.2.2	FPP	128
6.2.3	Off-axis DHI.....	131
6.3	Conclusion.....	131
<i>Appendix A</i>		<i>134</i>
1.	<i>Measurements of surface profile</i>	<i>137</i>
2.	<i>Measurements of dynamic out of plane displacements on a scattering surface</i>	<i>140</i>
3.	<i>Measurement of fast transient out of plane waves on a scattering surface</i>	<i>143</i>
<i>Curriculum Vitae</i>		<i>146</i>

List of Tables

Table 2-1: Code metadata for PhaseWare including: links for the software package, all the .m files used in the software, manual for the users, licensing information, and requirements.	55
--	----

List of Figures

<p>Figure 1-1: FPP system schematic and simulated patterns. a) Triangulation principle, b) simulated object example in MATLAB by peak function, c) a typical sinusoidal fringe pattern generated by the projector to illuminate the object consisting of 10 fringes in the y direction, and d) the frame detected by the camera which shows the deformed pattern.</p>	4
<p>Figure 1-2: Interference between two plane waves with an off-axis angle between their wave vectors and the resulting sinusoidal fringe pattern as the interference.</p>	9
<p>Figure 1-3: Off-axis interference when the screen is positioned perpendicular to the two wave vectors' bisector.</p>	10
<p>Figure 1-4: On-axis interference between a plane wave and a spherical wave with the same wavelength that produces a pattern of circular fringes.</p>	12
<p>Figure 1-5: Interference between two spherical waves with the same wavelength at three observation planes (OP1, OP2, and OP3).</p>	13
<p>Figure 1-6: Off-axis DHI. a) Recording, b) reconstruction, and c) coordinate system. This figure is adapted from [6] and [31].</p>	15
<p>Figure 1-7: An example of the Fourier phase wrapping method. a) Simulated fringe pattern modulated with peaks (internal MATLAB function) and gaussian background intensity (the fringe pattern frame size: 500×500 pixels and spatial frequencies: $(f_x = 20, f_y = 60)$). b) Fourier domain of the fringe pattern which shows three main components, c) selected +1 order component by a Butterworth filter, and d) wrapped phase map by applying inverse Fourier transform.</p>	21
<p>Figure 1-8: Remove carrier frequency with the Fourier transform for the example illustrated in Figure 1-7. a) Fourier domain of the fringe pattern which shows three main</p>	

components, b) selected +1 order component by a Butterworth filter and shifted to the origin, and c) wrapped phase map. 22

Figure 1-9: Morlet function 23

Figure 1-10: An example of the phase wrapping process with Wavelet transform for a simulated deformed fringe pattern with peaks function and gaussian background intensity (the fringe pattern frame size: 500×500 pixels and spatial frequencies: $(f_x = 20, f_y = 60)$). a) Selected row of the deformed fringe pattern along with the corresponding amplitude line profile. b) The amplitude and c) the phase of the Wavelet transform over the selected row (the mother function is Morlet and the applied scales are in the range of $[0.5, 32]$). d) The wrapped phase map was calculated based on finding the ridge of the Wavelet result along with the corresponding line profile. 24

Figure 1-11: An example of the phase wrapping process with Hilbert transform. a) Deformed fringe pattern with peaks function and the size of 500×500 pixels. b) Hilbert transform of (a) which shows $-\pi/2$ phase-shift to the input signal. c) The wrapped phase which is calculated by $\arctan((b)/(a))$. d-f) Line profiles of the indicated regions of (a-c), respectively. 25

Figure 1-12: M-steps temporal phase stepping with even phase steps.
 $I_m s (m = 1, 2, \dots, M)$ indicate camera acquisitions over a specific pixel and the width of the rectangles indicates the integration time for the acquisitions. Adapted from [49]. 27

Figure 1-13: Phase unwrapping. a) simulated wrapped phase map with the size of 500×500 pixels, b) a line profile for the wrapped phase corresponding to column 250, c) unwrapped phase map, and d) line profile corresponding to (b). 28

Figure 2-1: Diagram describing the phase retrieval processing algorithms implemented in PhaseWare..... 44

Figure 2-2: Diagram of PhaseWare software architecture. The imported data contains the required main data and optional reference data, which is passed to pre-processing, phase

retrieval, and post-processing algorithms. The software provides tools for data visualization, data saving, and report generation in Microsoft Word format. 48

Figure 2-3: Fringe projection profilometry example using data generated by processing a sinusoidal function with the MATLAB *peaks* function. Reference (a) and Main (b) Data for the noiseless pattern. Unwrapped phase maps retrieved using FT (c), WT (d), and HT (e). Reference (f) and Main (g) Data for data with added Gaussian noise. Unwrapped phase maps for the latter case retrieved using FT (h), WT (i), and HT (j).. 50

Figure 2-4: Peak signal-to-noise ratio comparison for the fringe projection profilometry example between the noiseless and noisy patterns. 51

Figure 2-5: Line profile analysis of the fringe projection profilometry example at pixel row 500 for noiseless (a) and noisy (b) images..... 52

Figure 2-6: Processing of a hologram obtained by an off-axis DHI system [23,24]. a) Raw hologram of a USAF resolution target etched into a gold-coated silicon wafer (features measure 80 nm in depth). b) Image after cropping, DC offset removal, zero padding, and filtering. c) Amplitudes of the reconstructed complex image containing real and virtual components. d) Wrapped phase map with Fourier method corresponding to the real component. e) Carrier-removed phase-demodulated image. f) Absolute phase map obtained by unwrapping data in panel (e). g) Phase-unwrapped image after background subtraction. h) 3D representation of the object based on the absolute phase map with background removed..... 53

Figure 3-1: a) Schematic illustration of the setup consisting of a halogen light source, MFA, focusing lens, object, and snapshot multispectral camera. b) MFA consisted of a 2D array of four distinct filters at different wavelengths: 580 nm, 660 nm, 735 nm, and 820 nm indicated by blue (F1), orange (F2), yellow (F3), and purple (F4), respectively. c) Schematic of 2 vertical MFPs generated by combining pairs of spectral images of the object to form 2 unique monochromatic fringe patterns. For clarity, a single 4×4 pixel area is shown for each filter type, but the concept extends across all pixel data in each spectral image. d) Schematic of all 6 MFPs, distinguishable as 8 unique monochromatic fringe patterns. 63

Figure 3-2: Fringe extraction method. a) From top to bottom: image of the combination of spectral images F1 and F3 showing a magnified view of a small region indicated by the red box; 2D fast Fourier transform (FFT) of data in upper panel showing ± 1 order frequency components (green arrows), and harmonics (red arrows); 2D inverse fast Fourier transform (IFFT) of data in upper panel that has been masked to only include the $(f_x, 0)$, $(-f_x, 0)$, and $(0, 0)$ frequency components. b) Extraction of horizontal fringes from the F1-F2 combination and c) extracting two diagonal fringes from the F2-F3 combination. A magnified view of a small region of the larger data set is indicated by the red box..... 65

Figure 3-3: Subtraction of the complementary fringe patterns to produce a background-corrected and noise-reduced fringe pattern. a) Images of a vertical fringe pattern, b) horizontal fringe pattern, c) 45-degree fringe pattern, and d) 135-degree fringe pattern relative to the x-axis. From top to bottom: Images of the first complementary fringe pattern, second complementary π -phase shifted fringe pattern, color-coded intensity line profiles for the corresponding dashed lines indicated in the complementary fringe patterns, the DFP resulting from the subtraction of the first complementary fringe pattern from the second complementary fringe pattern, and the line profile for the corresponding dashed lines indicated in the DFP..... 67

Figure 3-4: Phase demodulation for a head phantom. a) Photograph of the head phantom. b) Vertical fringe pattern acquired with MFPP method (top), the 2D frequency spectrum of the fringe pattern (second from top), wrapped phase computed from 2D frequency spectrum (second from bottom), and unwrapped phase (bottom) computed from the wrapped phase. c) Similar to (b), except results are for the vertical π -phase shifted fringe pattern complementary to (b). d) Similar to (b), except results are for the differential fringe pattern computed by subtracting the fringe pattern in (c) from the fringe pattern in b. e) 3D visualization of the object computed from the unwrapped phase in (d) after applying phase to height conversion..... 71

Figure 3-5: Accuracy test of MFPP. a) CAD model of the target consisting of a hemisphere with 100 mm diameter. b) and (c) Wrapped and unwrapped phase maps, respectively. d) 3D representation of the unwrapped phase after phase-to-height conversion. e) Color-coded error map between the measured height and the expected. f) Statistical error result against the orientation of the surface normal toward the MFPP optical axis. 73

Figure 3-6: Lateral resolution test of MFPP. a) CAD model of the target consisting of five groups of bars of varying width (1 to 5 mm in steps of 1 mm). b) and (c) Wrapped and unwrapped phase maps, respectively. d) FWHM of the measured width against the expected width of the bars for different groups. e) Profile of the measured height corresponding to the red dashed line in panel (c). 74

Figure 3-7: Axial resolution test. a) CAD model of the axial resolution target consisting of ten hemispheres of different radius (10, 5, 4.5, 4, 3.5, 3, 2.5, 2, 1.5, and 1 mm). b) and (c) Wrapped and unwrapped phase maps, respectively. d) Measured heights of the hemispheres against the expected values. e) Measured height corresponding to the red dashed line in (c). 74

Figure 3-8: Analysis of motion artifacts by scanning a rotating object. a) Reflective cylindrical object with 35 mm radius mounted on a rotational stage. The center of the cylinder was located 20 mm from the center of the stage. b-d) Wrapped phase map, unwrapped phase map, and the 3D plot of the unwrapped phase map for frame index 1 (when the cylinder was located on the right side of the stage from the perspective of the camera). e) Color-coded line profiles for continuous frame indices from 1 to 160. The blue area shows the first frame index, and the yellow lines show the line profiles for all indexes. The magnified area (right panel in (e)) shows frames 1 to 7 when the cylinder moved from right to left as the stage rotated. f) Color-coded height profiles of the cylinder corresponding to the select frame indices indicated in (e). 76

Figure 3-9: Dynamic 3D surface scanning of a rotating object. a) Wrapped and (b) unwrapped phase maps for five selected frames of a rotating head phantom at different stages of object's rotation. c) 3D visualization of the unwrapped phase maps. 77

Figure 3-10: Evaluating the sensitivity of the fringe patterns in their different directions. a-d) DFPs in the vertical, horizontal, 45°, and 135° directions, respectively. e-h) Unwrapped phase maps for DFPs. i-l) Detected edge features with Sobel method for maps illustrated in (a-d), respectively. m) CAD model of the target consisting of twelve spokes spaced 30° apart. n) Combination of edge features illustrated in (i-l). The arrows at the bottom left of the panels indicate in which direction the DFP was used in those panels. 78

Figure 4-1: Multispectral pattern generation. a) Schematic of the MFA (not to scale). b) Rendering of the optical setup consisting of a halogen light source, MFA, lenses, the object, and snapshot multispectral camera. c) Color image (Apple iPhone-6s) of the CP projected onto the surface of a white plastic object. 93

Figure 4-2: Normalization process for phase extraction from four spectral fringe patterns. a) Four adjacent pairs of FPs. b) Schematic of a pair of identical windows sliding over a pair of adjacent FPs. c) Example of intensity plots of I_2 against I_1 for a sliding window (25,25) pixels in size and centered at (100,400). d) Ellipse fitted with least squares method to data in panel (c). e) Normalized fitted ellipse computed from data in panel (d). f-i) Four FPs captured with the multispectral camera for a flat surface after filtering with a gaussian low pass filter. j) Intensity profiles along the dashed lines within the regions indicated in the magnified parts of (f-i). k-n) The normalized FPs corresponding to data in panels (f-i). o) Intensity profiles along the dashed lines within the regions indicated in the magnified parts of (k-n)..... 97

Figure 4-3: Example of the phase step estimation for all four FP pairs based on the normalized Lissajous figure..... 99

Figure 4-4: Simulations to test the performance of the pre-processing explained in the method section for a) normalization and b) angle offset detection..... 101

Figure 4-5: Phase retrieval process for a flat object. Wrapped phase map (a), unwrapped phase map (b), and line profiles obtained using Eq. (4-3) with FPs before normalization (c). d-f) Same as (a-c) after normalization over FPs. g-i) Same as (a-c) using Eq. (4-11) and FPs after normalization. j) Comparison of the profiles obtained using the different

phase retrieval methods to the ideal case (flat imaged object) which shows the phase error..... 102

Figure 4-6: 3D imaging of complex objects. The left column shows the raw images captured by the multispectral camera before demosaicing. The second column shows the wrapped phase maps. The third column shows the color-coded height maps. The right-most column shows 3D visualizations of the height map. a-d) A cube object, e-h) a plastic head phantom, i-l) back surface of a hand, and m-p) a hand holding two ping-pong balls. 104

Figure 5-1: Single FFT reconstruction for off-axis holographic interferometry. a) A raw hologram. b) The reconstruction of the high-pass-filtered raw hologram, which contains the twin images as well as the weakened zero-order information. c) The amplitude image of the indicated part of the reconstructed image in (b). d) The phase image of the indicated part of the reconstructed image in (b). 117

Figure 5-2: a) The original phase pattern acquired from the FFT reconstruction. Panels (b) and (c) show magnified areas indicated by the red dashed boxes. d) The contrast-enhanced image of the fringe pattern shown in panel (a). Panels (e) and (f) show magnified areas indicated by the red dashed boxes. 118

Figure 5-3: 3D visualization of the enhanced phase pattern shown in Figure 5-2(d)..... 119

Figure 5-4: The process of phase carrier removal. a) Fourier domain of the enhanced phase map shown in Figure 5-2 (d) and the Hamming window filter to select the spectrum (dashed red circle). b) The phase acquired after applying the inverse Fourier transform to the origin-shifted and filtered spectrum. c) The 2D unwrapped phase from panel (b). 120

Figure 5-5: a) 3D visualization of the unwrapped phase shown in Figure 5-4 (c). b) The line profile from $Y = 5000 \mu\text{m}$ in (a). 121

Figure 5-6: a) Estimated background phase for the unwrapped phase in Figure 5-4 (c). b) The estimated object phase computed by subtraction of the estimated background from the unwrapped phase in Figure 5-4 (c). 121

Figure 5-7: a) 3D visualization of the unwrapped phase shown in Figure 5-6 (b). b) The line profile from $Y = 5000 \mu\text{m}$ in (a). 122

Figure 5-8: a) A scanned image of the target quadrant with 33 nm etch depth. b) The full width at half maximum (FWHM) of the minor axis of each bar shown in panel (a). .. 123

List of Appendices

Appendix A: Dynamic surface tracking with off-axis digital holographic interferometry

..... 130

List of Acronyms and Glossary

2D	Two Dimensional
3D	Three Dimensional
CCD	Charge-Coupled Device
CP	Composite Pattern
DFP	Differential Fringe Pattern
DHI	Digital Holographic Interferometry
dp-ESPI	Double-Pulsed Electronic Speckle Pattern Interferometry
FFT	Fast Fourier Transform
FP	Fringe Pattern
FPP	Fringe Projection Profilometry
FPS	Frames Per Second
FT	Fourier Transform
FWHM	Full Width at Half Maximum
HT	Hilbert Transform
IFFT	Inverse Fast Fourier Transform
LED	Light Emitting Diode
LEF	Lissajous Figure and Ellipse Fitting
MEMS	Micro-electromechanical system
MFA	Multispectral Filter Array
MFPP	Multispectral Fringe Projection Profilometry
MSE	Mean Square Error
OP	Observation Plane
OPD	Optical Path Differences
PLA	Polylactic Acid
PMP	Phase Measuring Profilometry
PSP	Phase-Shifting Profilometry
PSNR	Peak Signal-To-Noise Ratio
QTH	Quartz Tungsten Halogen
RGB-D	Red Green Blue Depth

RoI	Region of Interest
RPM	Revolutions Per Minute
SNR	Signal-To-Noise Ratio
USAF	1951 United States Air Force
W	Watt
WFT	Windowed Fourier Transform
WT	Wavelet Transform
$F\{\cdot\}$	Fourier Transform Function
$iF\{\cdot\}$	Inverse Fourier Transform Function
$Im\{\cdot\}$	Imaginary Functions
$Re\{\cdot\}$	Real Functions

Chapter 1

1 Introduction

There is a rapidly growing need for fast and precise surface measurement in many industrial applications, especially in the medical industry [1]. For example, surface measurement techniques are crucial for 3D digitization of body surfaces, eye surface curvature measurement, manufacturing and testing of medical implants, monitoring surgical instruments during operations, and remote surgery. A major difference between other applications in industrial environments and those that involve patients is the requirement that these technologies should be completely safe to patients. This qualification severely limits medical applications [2]. Optical profilometers, however, provide a solution as they do not have this limitation, and have added benefits such as being non-contact, fast, and providing accurate measurements; they thus have the potential to develop customized products for medical applications [3]. Optical profilometry consists of a broad group of instruments that have attracted recent attention. Advancements in optical technology have directly influenced the development of profilometry. The core concept is to use light as an information carrier and light-sensitive devices as sensors. Roughly speaking, the method can be categorized into three types: time-of-flight, triangulation, and interferometry [4].

Time-of-flight refers to systems that use a transmitter to project electromagnetic waves towards an object and a receiver to detect the reflected waves. Then, by calculating the time-delay between the transmitted and received waves, the object's surface morphology can be estimated [5].

The triangulation principle generates a known triangle for every measurement point on the object's surface such that each point is one vertex. The other two vertices are specific locations either on two separate cameras or on one camera and one projector [4]. Using two cameras, which is known as a stereo system, is called passive triangulation.

Replacing one of the cameras by a projector turns the system into an active

triangulation [6]. It depends on the image target and the ambient light, either active or passive methods will produce satisfactory measurements.

Interferometry techniques are based on the principle of interference between a coherent light ray diffracted by an object and a version of the original light [7]. The interference signal encapsulates the characteristics of an object which caused the diffractions, making it possible to assess the object's characteristics using the interference. A reflective object may demonstrate diffraction due to its morphological features, while a transparent object may produce diffraction due to intrinsic refractive index differences. The first scenario is known as reflection interferometry and the second, transmission interferometry [8].

The aforementioned three methods are used in different applications since they have different range-of-measurement, accuracy, sensitivity, and speed of imaging. The motivation for this thesis is the need to design two optical profilometers suitable for two different tasks: macroscopic and microscopic 3D surface imaging. The application for the first task is digitizing dynamic surfaces [9]. The dynamic manner of the objects, e.g., an organ of the human body, specifies that the system must be robust to its movements. The application for the second task is the measurement of nanometer-scale features of a surface and eventually to use the system to measure nanometer-scale vibrations and deformations of a surface.

From the medical standpoint, nanometer deformation measurement is useful to analyze and track the behavior of tumors located close to the skin, e.g., measuring breast volumes and changes in skin appearance in order to analyze breast tumors in pre-surgical or post-surgical patients [10,11]. Also, vibration measurement can play a crucial role in medical applications, for example, to study ear and middle-ear response to the acoustic waves [12]. Another recently proposed application of vibration measurement is non-contact acoustic measurement. For conventional ultrasound systems, piezoelectric transducers are used to transmit and detect acoustic signals. An alternative to detect the acoustic signal is using optical vibration measurement devices to detect the vibrations caused by these acoustic signals [13]. This method of signal detection is non-contact, and it can also provide higher dynamic range detection and wider band frequency sensitivity

compared to piezoelectric transducers. This technique has been adapted as a signal detector in photoacoustic systems as well [14,15]. The photoacoustic systems generate acoustic waves inside the tissue by illuminating the tissue with laser light; therefore, optical measurements allow for full non-contact acoustic signal generation and detection.

In this thesis, the focus is on a well-known type of active triangulation class called fringe projection profilometry (FPP) and a type of reflection interferometry class called off-axis digital holographic interferometry (DHI). These two methods share a common data processing step which is phase retrieval based on the fringe analysis. The retrieved phase can be used to estimate the surface of the object in a static measurement, or the surface deformations and movement in dynamic measurement. This chapter discusses the principle of FPP and off-axis DHI, intuitive analysis of the fringe patterns, the potential applications of those two systems, the thesis objectives, and the thesis outline.

1.1 Principle of fringe projection profilometry (FPP)

Fringe projection profilometry (FPP) is an optical surface measurement method that is based on active triangulation. The system relies on three steps: 1) casting known structured light pattern(s) onto a target object using a light projector, 2) acquiring 2D image(s) of the patterns that have been deformed by the object's surface, and 3) processing the acquired image(s) to calculate 2D profile(s) of the surface [16]. The traditional FPP system uses fringe pattern(s) as the structured light illumination, such that the object's surface variation deforms the fringe pattern(s). This deformation modulates the phase of the fringes which can later be retrieved to demodulate the surface morphology [17].

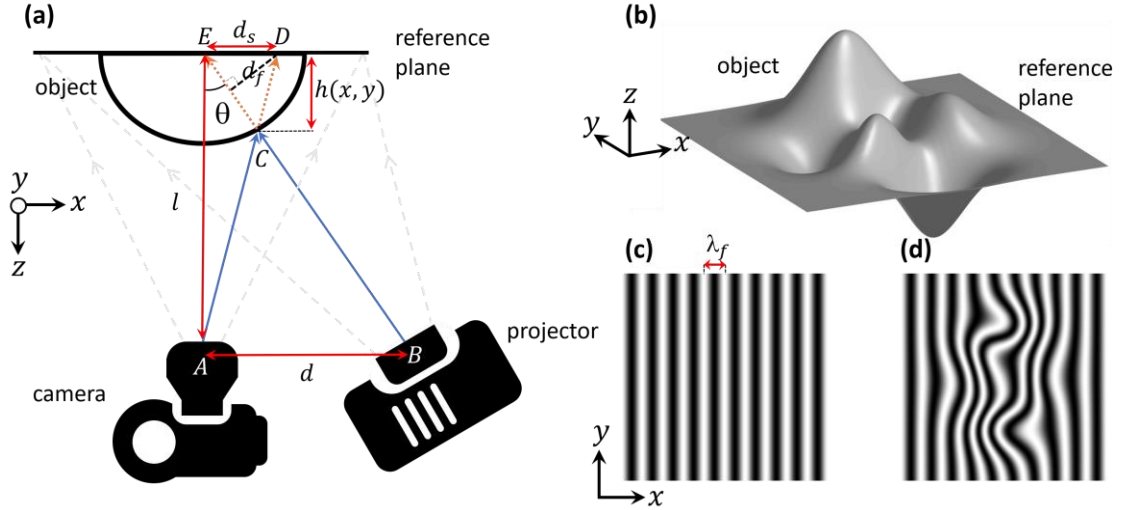


Figure 1-1: FPP system schematic and simulated patterns. a) Triangulation principle, b) simulated object example in MATLAB by peak function, c) a typical sinusoidal fringe pattern generated by the projector to illuminate the object consisting of 10 fringes in the y direction, and d) the frame detected by the camera which shows the deformed pattern.

1.1.1 Triangulation

The most common setup for FPP is depicted in Figure 1-1 (a) where a digital projector casts a fringe pattern onto the object and a camera distanced d from the projector captures the reflectance of the fringe pattern. The object is positioned on a reference plane parallel to the camera-projector line (\overline{AB}). Typically, the camera is positioned in such a way that its optical axis is directed to the normal of the reference plane and the projector has a θ degree inclination toward the reference normal. When illuminating an optically non-flat object (e.g., Figure 1-1 (b)) with a 2D straight fringe pattern, (e.g., Figure 1-1 (c)), what the camera sees is a deformed version of the fringe pattern, similar to what has been presented in Figure 1-1 (d). The reason for this event is simple. Assume a specific ray that is supposed to hit point E in the absence of the object gets reflected by point C on the surface of the object. From the camera's perspective, point C in the absence of the object is equivalent to point D on the reference plane. Therefore, the existence of an object with height h at the location of (x, y) in the cartesian coordinate system causes a shift of

$|\overline{ED}| = d_s$ into the illuminated pattern. Based on the similarities between the two triangles (Δ_{ABC} and Δ_{DEC}) the unknown h can be calculated as:

$$\frac{d}{d_s} = \frac{l-h}{h} \Rightarrow h = \frac{l \times d_s}{d + d_s} \quad (1-1)$$

Parameters l and d on the right side of the equation belong to the configuration design and d_s is the shift caused by the object which needs to be measured. Indeed, the rationale behind using a known structural pattern (e.g., a fringe pattern) to illuminate the object is to find these shifts. Fringe patterns, specifically, associate the shifts to the phase difference between the case that includes the object and the case that lacks it, such that:

$$d_s = \frac{d_f}{\cos(\theta)} = \frac{N \times \lambda_f}{\cos(\theta)} = \frac{\Delta\varphi \times \lambda_f}{2\pi \cos(\theta)} \quad (1-2)$$

where λ_f is the projected fringe wavelength and N is the number of fringes along with the shift distance, which is equal to the total phase shift divided by 2π . This is due to the fact that every fringe causes a 2π phase shift. Therefore, phase measurement is the key to FPP; in fact, another prevalent name for the FPP is phase measurement profilometry (PMP). There are several established methods to measure phase shifts based on the deformed fringe patterns which will be covered later.

1.2 Principle of off-axis digital holographic interferometry (DHI)

Waves propagating in space can interfere with one another at any surface located at their intersection. The interference between two monochrome wave beams emerges as an intensity pattern that encompasses both the amplitude and phase information of the two beams. The amplitude represents the irradiance of the wave and the phase represents the local propagation direction of the wave. Holographic interferometry, which is a branch of holography, applies this concept to perform 3D imaging of objects; this was first proposed by Gabor [18]. In the first proposed system, one of the beams was diffracted by an object, called the “object beam”, while the other was preserved, called the “reference beam”. A photographic plate was used to record the two beams’ interference and the

recorded plate was called the “interferogram”. Then by illuminating the interferogram with a replica of the reference beam, the 3D image of the object was reconstructed in the space. This Nobel Prize-winning invention ushered in a new era of imaging by giving us a way to measure the morphology of objects as well as track their movement and deformation.

However, there were three major problems with this Gabor’s system. First, the system needed wet-chemical photographic plates to record the interferograms [19], which reduced the imaging speed. The second problem was that the image reconstruction required a physical reference beam to illuminate the recorded interferogram [20]. Later, both these issues were solved by introducing digital camera sensors as the recorder for the interference phenomena [21]. Digital cameras are super-fast at measurements and as they collect the data in a digital format, the reconstruction can be performed in the computers numerically without physical re-illumination [22]. The third problem was related to reconstruction. By re-illuminating the interferogram with the reference beam, the reconstructed image of the object was contaminated with noise encompassing the twin image of the object and non-diffracted light [23]. Years later, this problem was solved by a small modification to the recording part of Gabor’s system. This was achieved by introducing a small angle between the reference beam and the object beam at the surface of the recorder [24]. This breakthrough approach, called off-axis holographic interferometry, separates the three reconstruction elements, i.e., the image, the twin image, and the non-diffracted light, such that they do not overlap each other.

The off-axis angle creates a fringe pattern in the interference pattern where the fringes show contours of the existing optical path differences (OPDs) for the rays through the interference beam. The periodic nature of the light waves turns the OPDs into constructive and destructive interferences between the electric fields of the two waves. Constructive interference happens when the two waves interact such that they are aligned and form a bigger wave, and the alignment occurs when the phase difference between the two waves is an even factor of π . Destructive interference, on the other hand, is the cancelation of two waves and happens when the phase difference is an odd factor of π [25].

The generated fringes act as information carriers, in such a way that any scattering medium in the path of the beams changes the phase of the fringes. Therefore, measuring the phase and monitoring the phase-change provides information about the behavior of the medium. To fully understand the concept of the interference pattern, it is worthwhile to briefly review light propagation theory.

1.2.1 Coherent light wave interference

Derived from the Maxwell equations, the electromagnetic wave equation in free space can be modeled as [22,26]:

$$\nabla^2 \mathbf{E} - \frac{1}{v^2} \frac{\partial^2 \mathbf{E}}{\partial t^2} \quad (1-3)$$

where \mathbf{E} is the electric field, v is the velocity of the wave, t is the time parameter, and ∇^2 is the Laplacian operator, equal to $\frac{\partial^2}{\partial x^2} + \frac{\partial^2}{\partial y^2} + \frac{\partial^2}{\partial z^2}$ in the cartesian coordinates. The complex traveling wave solution to this equation is:

$$E(\mathbf{r}, t) = A(\mathbf{r}, t) e^{i(\omega t - \mathbf{k} \cdot \mathbf{r})} \quad (1-4)$$

where $\mathbf{r} = (x, y, z)$ is the position vector in space, A is a complex amplitude value that encompasses the amplitude and the initial phase of the wave, ω is the angular frequency, and $\mathbf{k} = (k_x, k_y, k_z)$ is the wave vector, whose absolute value represents the wave-number ($k = |\mathbf{k}| = \omega/v = 2\pi/\lambda$, λ is the wavelength). The argument of the exponential term in Eq. (1-4) represents the phase of the propagated wave in space. Now we want to see what will happen if two waves interfere on a screen. The answer to this question is dependent on the shape of the waves. The following investigates three interference scenarios for two well-known wave shapes.

1.2.1.1 Interference between two plane waves

A plane wave is one form of propagation where the wave is traveling along the wave vector in the shape of planes perpendicular to the wave vector, such that the phase remains constant in every plane. The complex amplitude of the plane wave (with linear polarization) can be represented as:

$$E(\mathbf{r},t) = Ae^{j(\omega t - \mathbf{k} \cdot \mathbf{r})} \quad (1-5)$$

where A is constant over the entire space. Superposition of two propagated plane waves with certain conditions such as having a similar wavelength, existing off-axis angle between their wave vectors, and no scattering medium in the path of the beams provides an electric field on the screen equal to:

$$E_s(\mathbf{r},t) = E_1(\mathbf{r},t) + E_2(\mathbf{r},t) = A_1e^{j(\omega t - \mathbf{k}_1 \cdot \mathbf{r})} + A_2e^{j(\omega t - \mathbf{k}_2 \cdot \mathbf{r})} \quad (1-6)$$

where the subscript s represents the superposition, and the subscripts 1 and 2 represent the parameters belonging to the two beams. Light-sensitive tools such as photodiodes, cameras, or human eyes can detect the irradiance or “intensity” of light which is the average of the power transmitted per unit area over a short time (dependent on the tool) but longer than $1/\nu$. Based on the Maxwell equations, the intensity of the interference will be calculated as:

$$\begin{aligned} I(\mathbf{r}) &= \left\langle |E_s(\mathbf{r},t)|^2 \right\rangle_{time\ average} \\ &= \left\langle (A_1e^{j(\omega t - \mathbf{k}_1 \cdot \mathbf{r})} + A_2e^{j(\omega t - \mathbf{k}_2 \cdot \mathbf{r})}) \cdot (A_1e^{-j(\omega t - \mathbf{k}_1 \cdot \mathbf{r})} + A_2e^{-j(\omega t - \mathbf{k}_2 \cdot \mathbf{r})}) \right\rangle_{time\ average} \\ &= A_1^2 + A_2^2 + A_1A_2e^{j(\mathbf{k}_2 \cdot \mathbf{r} - \mathbf{k}_1 \cdot \mathbf{r})} + A_1A_2e^{-j(\mathbf{k}_2 \cdot \mathbf{r} - \mathbf{k}_1 \cdot \mathbf{r})} \end{aligned} \quad (1-7)$$

Averaging over time dissolves the ωt terms. Then, by using Euler’s formula and the intensity values of the two beams we have:

$$I(\mathbf{r}) = I_1 + I_2 + 2\sqrt{I_1I_2} \cos(\mathbf{k}_s \cdot \mathbf{r}) \quad (1-8)$$

where $\mathbf{k}_s = \mathbf{k}_2 - \mathbf{k}_1$ and $\mathbf{k}_s \cdot \mathbf{r} = \Delta\phi$ is the phase difference between the two beams. Equation (1-8) reveals that the interference pattern consists of three parts as follows:

1. $I_1 + I_2$: the autocorrelation term that indicates the background or DC component,
2. $2\sqrt{I_1I_2}$: the modulation amplitude, and
3. $\cos(\mathbf{k}_s \cdot \mathbf{r})$: the periodic term which shows the interference effect.

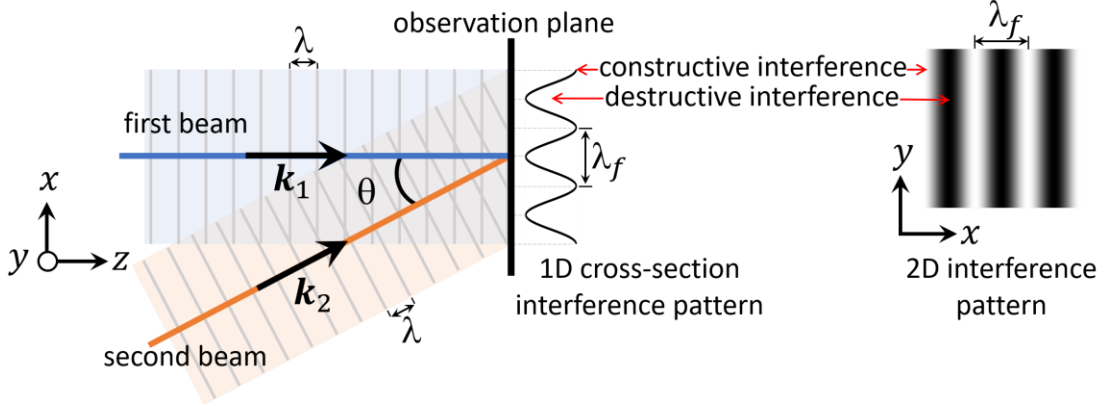


Figure 1-2: Interference between two plane waves with an off-axis angle between their wave vectors and the resulting sinusoidal fringe pattern as the interference.

Figure 1-2 shows an example of off-axis interferometry such that the first beam wave vector is in the z direction and the second beam wave vector is off by θ degree. The interference effect (the argument of the \cos function) can be rewritten as:

$$\Delta\phi = \phi_2 - \phi_1 = \mathbf{k}_s \cdot \mathbf{r} = (\mathbf{k}_2 - \mathbf{k}_1) \cdot \mathbf{r} = (k_{x_2} - k_{x_1}) \cdot x + (k_{y_2} - k_{y_1}) \cdot y + (k_{z_2} - k_{z_1}) \cdot z \quad (1-9)$$

Since the two waves have the same frequency, $|\mathbf{k}_1| = |\mathbf{k}_2| = k = \frac{2\pi}{\lambda}$, then we have:

$$\begin{cases} k_{x_1} = 0, & k_{y_1} = 0, & k_{z_1} = k \\ k_{x_2} = k * (\sin\theta), & k_{y_2} = k * (0), & k_{z_2} = k * (\cos\theta) \end{cases} \quad (1-10)$$

$$\mathbf{k}_s \cdot \mathbf{r} = \frac{2\pi}{\lambda} (\sin\theta) \cdot x + \frac{2\pi}{\lambda} (\cos\theta - 1) \cdot z \quad (1-11)$$

This shows that the interference pattern on a screen positioned at the xy -plane has a periodicity with a wavelength equal to $\lambda/\sin\theta$ in the x direction, analogous to a fringe pattern where the fringes are directed along the y axis. The same intensities alongside a specific fringe hold the same phase difference between the beams. The fringe spacing can be controlled in such a way that decreasing the θ will increase the fringe wavelength. Moreover, based on Eq. (1-10), there is another periodicity term in the z direction with a wavelength equal to $\lambda/(1 - \cos\theta)$, which means moving the observation plane (light sensitivity tools) in z can change the intensity of the interference fringe pattern. The

periodicity in the z direction will disappear if the screen is positioned perpendicular to the two wave vectors' bisector as in the setup shown in Figure 1-3.

$$\mathbf{k}_s \cdot \mathbf{r} = \frac{2\pi}{\lambda}(\sin\theta_1 + \sin\theta_2) \cdot x + \frac{2\pi}{\lambda}(\cos\theta_1 - \cos\theta_2) \cdot z = 2 * \frac{2\pi}{\lambda} \sin\left(\frac{\theta}{2}\right) \cdot x \quad (1-12)$$

Therefore, it can be seen that the fringe pattern wavelength is $\lambda / \left(2 \sin\left(\frac{\theta}{2}\right) \right)$. Comparing the two setups at first shows a significant difference between the results. However, for small off-axis angles that $\sin(\theta) \approx \theta$, the two setups provide fringe patterns with the same wavelength equal to $\lambda_f = \lambda / \theta$. Also, selecting a small angle is a requirement in case of detection, since increasing the θ will decrease the fringes' wavelength, or in other words, increase the fringes' frequency. The detection unit must be able to correctly sample the fringe pattern to fulfill the Shannon sampling theorem: that the sampling rate must be equal to or greater than twice the highest frequency in the pattern. For the case of using a camera as a detector we have:

$$\frac{1}{\Delta x} \geq 2 * \frac{1}{\lambda_f} \Rightarrow \theta \leq \frac{\lambda}{2\Delta x} \quad (1-13)$$

where Δx represents the camera's pixel size.

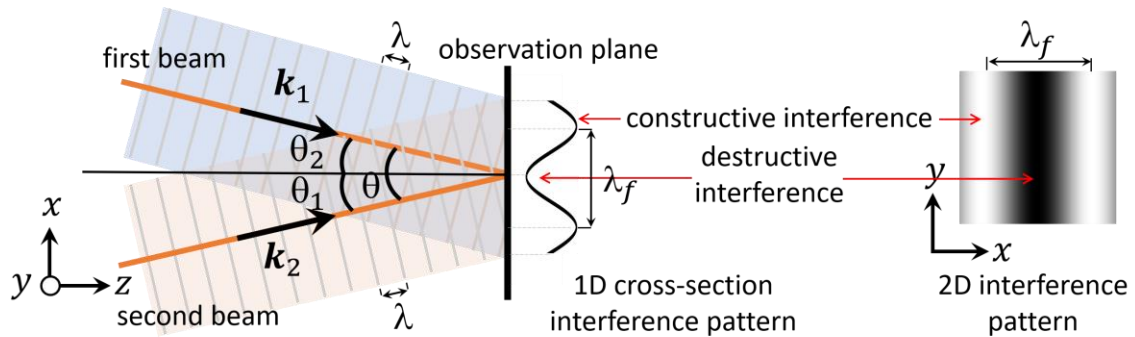


Figure 1-3: Off-axis interference when the screen is positioned perpendicular to the two wave vectors' bisector.

1.2.1.2 Interference between a plane and a spherical wave

When the light source is a point, the waves will propagate with spherical shape in space. At a given time, the waves are similar to a cluster of concentric spheres in which each spherical surface has a constant phase. In this case, the wave equation is:

$$E(\mathbf{r}, t) = \frac{A}{r} e^{j(\omega t - k \cdot r)} \quad (1-14)$$

When the observation plane is located parallel to the xy plane at z , the source of the spherical beam is located at the origin, and the reference beam wave vector is angled θ degree from x direction, the superposition of the two beams would be:

$$E_s(\mathbf{r}, t) = E_1(\mathbf{r}, t) + E_2(\mathbf{r}, t) = \frac{A_1}{z} e^{j(\omega t - k_1 \cdot \sqrt{x^2 + y^2 + z^2})} + A_2 e^{j(\omega t - k_2 \cdot r)} \quad (1-15)$$

By making the assumption that A_1/z is constant and equal to A_2 for the observation plane, we have:

$$\Delta\phi = k \cdot (x \sin \theta + 0 + z \cos \theta) - k \cdot \sqrt{x^2 + y^2 + z^2} \quad (1-16)$$

When there is no off-axis angle between the beams, i.e., θ is zero, the phase difference becomes:

$$\Delta\phi = k \cdot \sqrt{x^2 + y^2 + z^2} = k z \sqrt{1 + \frac{x^2 + y^2}{z^2}} \approx k \cdot \frac{(x^2 + y^2)}{2z} \quad (1-17)$$

In this equation, we have used the $\sqrt{1 + \varepsilon} \approx 1 + \frac{\varepsilon}{2}$ approximation (the first two elements of the Maclaurin's series expansion) and the fact that $z \gg x, y$. Equation (1-15) is a pattern of circular fringes in the observation plane centered at $(x = 0, y = 0)$ and fringe spacing decreases by going farther from the center (refer to Figure 1-4). Adding an off-axis angle shifts the center of the circular fringes along the off-axis direction.

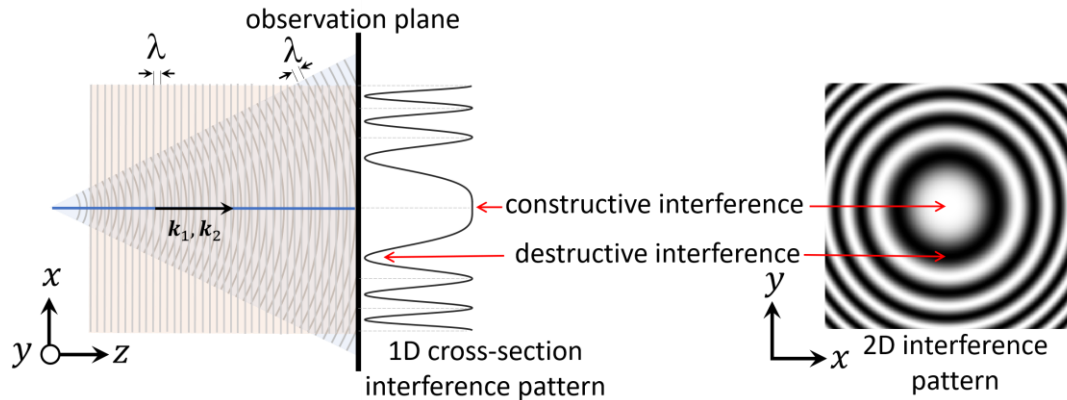


Figure 1-4: On-axis interference between a plane wave and a spherical wave with the same wavelength that produces a pattern of circular fringes.

1.2.1.3 Interference between two spherical waves

Depending on the different perspectives for the observation plane, the interference of two spherical waves can generate different forms of fringe patterns. Figure 1-5 shows three perspectives. The first case is when the observation plane is perpendicular to the line that connects the origin of the two beams (Figure 1-5, OP1). In this case, the interference appears as circular Newton rings. Figure 1-5, OP2, depicts the observation plane parallel to the connector of the two wave origins which shows non-straight open fringes. The third observation plane shows the interference in the plane of the two origins' connector and it is similar to OP2 (shown as OP3).

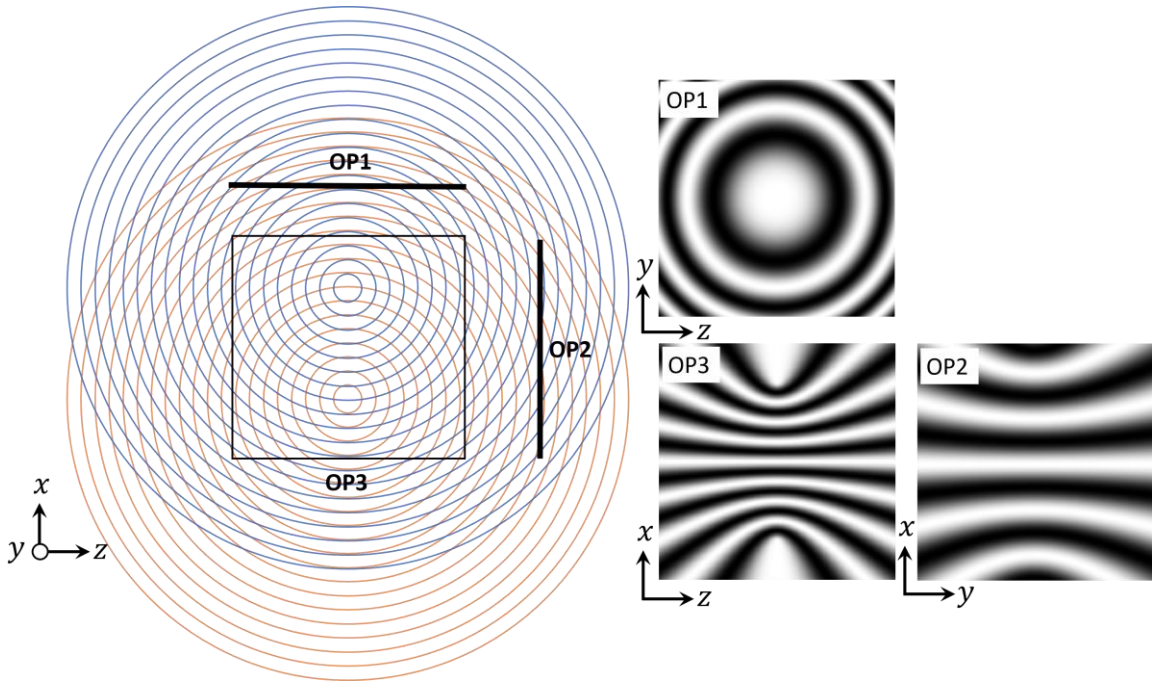


Figure 1-5: Interference between two spherical waves with the same wavelength at three observation planes (OP1, OP2, and OP3).

1.2.2 Effect of scattering medium on interference fringe pattern

Adding a scattering medium in the path of one of the coherent beams will affect the interference pattern. The wave can pass through the scattering medium (transmission interferometry) or be reflected by it (reflection interferometry). Both methods are based on the OPD of the light. In transmission, the thickness and absorption features of the translucent object change the OPD of the rays, and in reflection, the height variation changes the OPD. Alteration of the OPD modulates the phase of the corresponding beam; therefore, having the phase information can reveal information about the object's refractive indices or surface morphology. Therefore, analyzing the interference pattern can provide information about the object. From now on, we will refer to the beam that is altered by the object as “object beam” and the fixed beam as “reference beam”.

For the setup shown in Figure 1-2, and based on Eq. (1-7), the interference on the observation plane can be rewritten as:

$$I = |E_O + E_R|^2 = |E_O|^2 + |E_R|^2 + E_O^* E_R + E_O E_R^* = A_O^2 + A_R^2 + 2A_O A_R \cos(\varphi_R - \varphi_O) \quad (1-18)$$

where $E_o(x, y) = A_o e^{j(\omega t - \varphi_o(x, y))}$ and $E_R(x, y) = A_R e^{j(\omega t - \varphi_R(x, y))}$ are the electric fields for the object beam and the reference beam, respectively. The phase difference of the two beams is indicative of the phase of the interference fringe pattern so that any change of the object beam phase directly influences the phase of the fringe pattern.

1.2.3 Reconstruction of the object beam

Equation (1-18) shows that the acquired interference intensity provides a combination of the amplitude and phase information for both object and reference beams, while the goal is to extract the phase of the object beam. To do so, the first step is to reconstruct the object beam from the combination of the object and the reference beams. Reconstruction is equivalent to re-illuminating the interferogram with the reference beam, also known as the reconstruction beam. This event will cause diffraction of the light through space and reconstruct the object wave, which exhibits the object's morphological features in 3D at the reconstruction plane.

In digital cases, where the interferogram is recorded by a digital sensor, the whole process of the reconstruction can be performed numerically with computers, i.e., simulation of the reference beam, multiplication of the reference and the interferogram, and numerical diffraction of the product to refocus the wave at the intended reconstruction plane [27]. For a given time, the re-illumination provides a product consisting of three terms [28]:

$$E_R I = E_R \left[|E_o|^2 + |E_R|^2 \right] + E_o^* E_R^2 + E_o |E_R|^2 \quad (1-19)$$

The first term is called the zero-order and indicates the non-diffracted waves, the second term is the +1-order which represents the real image, and the third is -1-order which represents the virtual image. The zero-order term is directed to the reference beam and it is equal to a multiplication of the reference wave. The real image is proportional to the complex conjugate of the object wave, so it propagates at $-\theta$ angle (relative to the reconstruction beam) [29]. The virtual image is proportional to the object wave and forms a virtual orthoscopic image at the location of the object (with angle θ relative to the reconstruction beam) [30].

Diffraction caused by re-illuminating the interferogram separates these three terms gradually, as a result of the off-axis angle between the object and the reference beams. Therefore, in the reconstruction plane located at distance d from the observation plane, it is possible to isolate and extract the complex amplitude of the object (Figure 1-6 (b)).

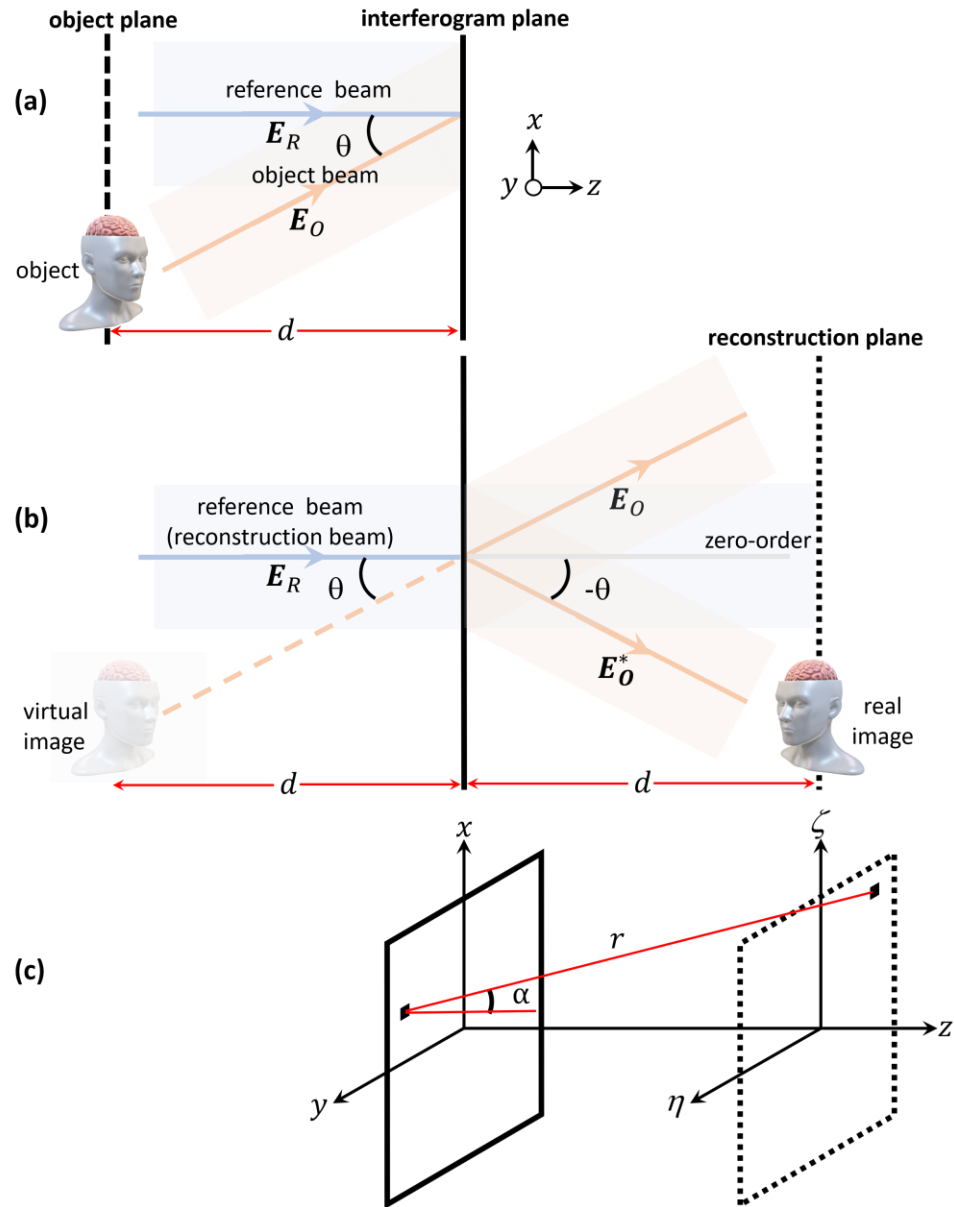


Figure 1-6: Off-axis DHI. a) Recording, b) reconstruction, and c) coordinate system.

This figure is adapted from [6] and [31].

Numerical holographic reconstruction attempts to simulate light propagation at the reconstruction plane by having the optical field at a specific aperture; here, the aperture is the part of the interferogram that has been re-illuminated by the reconstruction beam. The Huygens-Fresnel principle models light propagation such that every point of the aperture behaves similar to an individual light wave point source radiating uniformly in all directions, called secondary waves [32]. The optical field at any point beyond is equivalent to the integration over all the point sources while the backward waves interfere and cancel each other out [33]. This model can accurately describe the diffraction phenomenon [34]. The Fresnel-Kirchhoff and Rayleigh-Sommerfeld integrals model the wave diffractions mathematically as [31,35]:

$$\Gamma_{rec}(\zeta, \eta) = \frac{i}{\lambda} \int_{\square^2} E_{ap}(x, y) \frac{e^{-ikr}}{r} \left(\frac{1 + \cos(\alpha)}{2} \right) dx dy \quad (1-20)$$

where (x, y) and (ζ, η) denote the coordinates of the interferogram plane and the reconstruction plane, respectively, E_{ap} is the aperture field distribution which represents the re-illuminated interferogram (Eq. (1-19)), k is the wavenumber, α is the angle corresponding to the connector of the two coordinates and the z axis,

and $r = \sqrt{(x - \zeta)^2 + (y - \eta)^2 + d}$ is the Euclidean distance between the two coordinates (Figure 1-6 (c)).

Solving this integral requires considering some level of approximation. For example, Fresnel and Fraunhofer approximations are two models that simplify the parameter r in the denominator of the Eq. (1-21) by extending it [30]. Implementing these solutions is feasible by using the Fast Fourier Transform (FFT). The most common reconstruction algorithms are the discrete Fresnel transform, convolution, and angular spectrum, which are different based on the method of approximation and, subsequently, the number of FFTs used in their implementations [24,27–31,33,36].

1.3 Fringe analysis

A fringe pattern can be considered as a 2D intensity map with a series of ridge-valley structures. These structures can be linear, circular, or in complex forms, and the local intensity variation for every ridge-valley can be sinusoidal, triangle, square, etc. [37,38]. The structure of the fringes is related to the optics that generate them. For example, an FPP system usually employs a linear fringe pattern with sinusoidal intensity variations cast by a projector. Off-axis DHI with plane waves as reference and object beams provides a linear fringe pattern with sinusoidal intensity variations as well. DHI with a spherical wave as the reference, the object, or both beams provides circular-shaped fringes. In all cases, these fringes carry information. As with the structure, the information can vary based on the optical system and the operated applications; for instance, the information can be topography, motion, strain, or deformation of the object surface. A demodulation process is needed to extract this information from the fringe pattern. Many demodulation algorithms have been proposed for different systems that interpret the fringes based on a selection of the pattern's features such as phase, skeleton, orientation, shape, width, and length. Also, in terms of computation, the fringe pattern can be demodulated pixel-wise, locally, or globally. For the two systems that we cover in this thesis, i.e., FPP and off-axis DHI, the fringe pattern is linear, and the information is modulated in the phase of the fringes. Therefore, interpretation of the fringes is based on phase retrieval algorithms.

1.3.1 Phase retrieval

The ridge-valley structures of a sinusoidal linear fringe pattern consist of a set of sinusoidal straight paralleled fringes that can be modeled mathematically as [39]:

$$I(x, y) = a(x, y) + b(x, y) \cos[\varphi(x, y)] \quad (1-21)$$

where (x, y) denotes the camera pixel coordinates, and a and b are the background intensity and the modulation amplitude, respectively. These two parameters are constants, and their values are associated with the object's surface reflectivity index, the ambient lighting, and the acquisition system. Although these values indicate the quality of the

fringe pattern, in the case of employing the pattern to modulate the phase, they are less important than the third parameter, which is the phase of the pattern, shown as φ . The phase parameter encompasses two separate values: the phase of the carrier fringes and the modulated phase. The second term appears when the fringes are deformed.

The process of phase retrieval consists of a set of numerical methods to demodulate the phase map from single or multiple deformed fringe patterns. Phase retrieval algorithms can be categorized into two separate classes: spatial and temporal phase stepping [16,40,41]. The classification relies on the intensity of the pixels that allow the calculation of their phase. In spatial phase stepping, the phase is calculated for every pixel based on the values of its neighboring pixels, or even based on all pixels existing in the frame. On the other hand, temporal phase stepping algorithms are pixel-wise, such that they consider the value of a specific pixel in multiple frames while every frame encounters a distinct fringe pattern. The critical point is that the fringe patterns must be phase-shifted. Therefore, in Eq. (1-18), where for every pixel the unknowns are A , B , and φ , numerical solution require at least three independent equations. In this case, every phase-shifted fringe pattern provides an independent equation. Both classes possess advantages and disadvantages that will be explored below in more detail.

1.3.1.1 Spatial phase stepping

This class of phase demodulation is based on the global or local spatial carrier frequencies existing in a fringe pattern. The demodulation process is based on mathematical transform functions such as Fourier, wavelet, or Hilbert. They all use the concept of the spatial carrier frequency to calculate the complex fringe pattern that contains the phase quadrature components. Subsequently, the phase quadrature components can be used with an arctan function to obtain the wrapped phase map.

1.3.1.1.1 Fourier transform method

Fourier transform (FT) breaks the fringe pattern into its frequency components and selects the main component to wrap the phase [41]. To elaborate on this idea

mathematically, the expression of the fringe pattern with a modulated object phase can be rewritten as:

$$I(x, y) = a(x, y) + b(x, y) \cos[2\pi(f_x x + f_y y) + \varphi_o(x, y)] \quad (1-22)$$

where f_x and f_y are the spatial frequencies in the x and y dimensions of the fringe pattern, respectively, and φ_o is the modulated phase. Expanding this equation to its complex form by Euler's formula gives:

$$\begin{aligned} I(x, y) &= a(x, y) + b(x, y) \frac{e^{j(2\pi(f_x x + f_y y) + \varphi_o(x, y))} + e^{-j(2\pi(f_x x + f_y y) + \varphi_o(x, y))}}{2} \\ &= a(x, y) + c(x, y) e^{j(2\pi(f_x x + f_y y))} + c^*(x, y) e^{-j(2\pi(f_x x + f_y y))} \end{aligned} \quad (1-23)$$

where $c(x, y) = (1/2)b(x, y)e^{j\varphi_o(x, y)}$ is the term that contains the modulated phase and $*$ is the complex conjugate sign. Applying the Fourier transform to this equation provides the frequency spectrum expression of the pattern, as:

$$F\{I(x, y)\} = A(u, v) + C(u - f_x, v - f_y) + C^*(u + f_x, v + f_y) \quad (1-24)$$

where $F\{\cdot\}$ denotes the Fourier transform function, (u, v) are the coordinates in the Fourier domain, and A and C are the Fourier transforms of a and c , respectively. The right side of this equation shows the three main components where the first one is located at the origin $(u, v) = (0, 0)$ and is called the zero-order. This component represents the DC part of the fringe pattern plus low-frequency features such as background intensities. The second and third terms (± 1 orders) are symmetrical toward the origin and their centers are distanced $\sqrt{f_x^2 + f_y^2}$ from the origin (Figure 1-7 (b)). Therefore, raising the values of the spatial frequencies (i.e., (f_x, f_y)) assures the separation between these terms. Also, another condition to avoid overlap is to have slow spatial variations for the background (to limit the zero-order spatial frequency size), and slow spatial variations for the amplitude and phase (to limit the size of the symmetrical pair terms). Sufficient separation allows for easier filtering of the main components (Figure 1-7 (c)). Then,

applying the inverse Fourier transform (indicated as $\text{iF}\{\cdot\}$) over the selected main component provides:

$$\begin{aligned} \text{iF}\{C(u-f_x, v-f_y)\} &= c(x, y)e^{j(2\pi(f_x x + f_y y))} \\ &= \frac{b(x, y)e^{j\varphi_o(x, y)}}{2} e^{j(2\pi(f_x x + f_y y))} = \frac{b(x, y)}{2} e^{j(2\pi(f_x x + f_y y) + \varphi_o(x, y))} \end{aligned} \quad (1-25)$$

Then, the modulated phase can be extracted by:

$$2\pi(f_x x + f_y y) + \varphi_o(x, y) = \arctan \left[\frac{\text{Im}\{\text{iF}\{C(u-f_x, v-f_y)\}\}}{\text{Re}\{\text{iF}\{C(u-f_x, v-f_y)\}\}} \right] \quad (1-26)$$

where $\text{Im}\{\cdot\}$ and $\text{Re}\{\cdot\}$ are imaginary and real functions, respectively. Since this method uses the arctan function, the calculated phase is limited to the range of $(-\pi, \pi)$. This limitation causes 2π wrapping of the phase. The left side of this equation contains $\varphi_o(x, y)$ which is the modulated phase and $2\pi(f_x x + f_y y)$ which represents the spatial frequencies. This means that the arctan function results in a wrapped phase map containing the modulated phase and the carrier frequency (Figure 1-7 (d)).

The carrier frequencies can be removed in the process of phase retrieval by shifting the selected component to the origin of the Fourier spectrum (Figure 1-8). This shifting removes the carrier frequency from the spectrum. For example, shifting $C(u-f_x, v-f_y)$ to the origin gives $C(u, v)$ and applying the inverse Fourier transform to $C(u, v)$ provides $c(x, y) = b(x, y)e^{j\varphi_o(x, y)}/2$. Now the modulated phase can be extracted by:

$$\varphi_o(x, y) = \arctan \left[\frac{\text{Im}\{c(x, y)\}}{\text{Re}\{c(x, y)\}} \right] \quad (1-27)$$

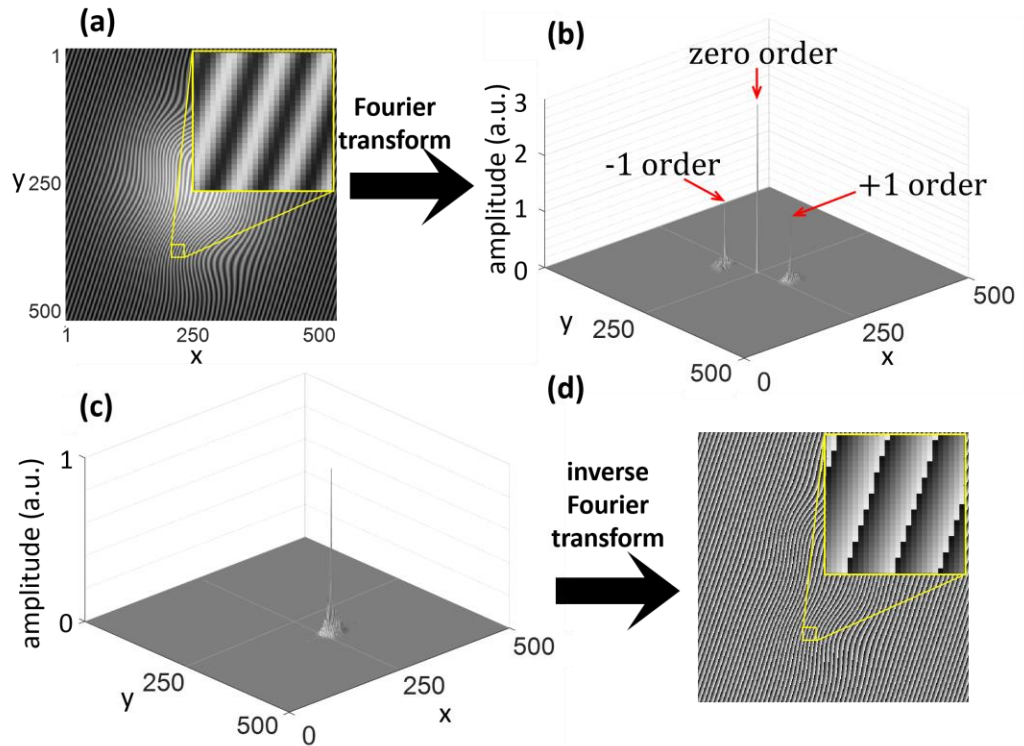


Figure 1-7: An example of the Fourier phase wrapping method. a) Simulated fringe pattern modulated with peaks (internal MATLAB function) and gaussian background intensity (the fringe pattern frame size: 500×500 pixels and spatial frequencies: $(f_x = 20, f_y = 60)$). b) Fourier domain of the fringe pattern which shows three main components, c) selected +1 order component by a Butterworth filter, and d) wrapped phase map by applying inverse Fourier transform

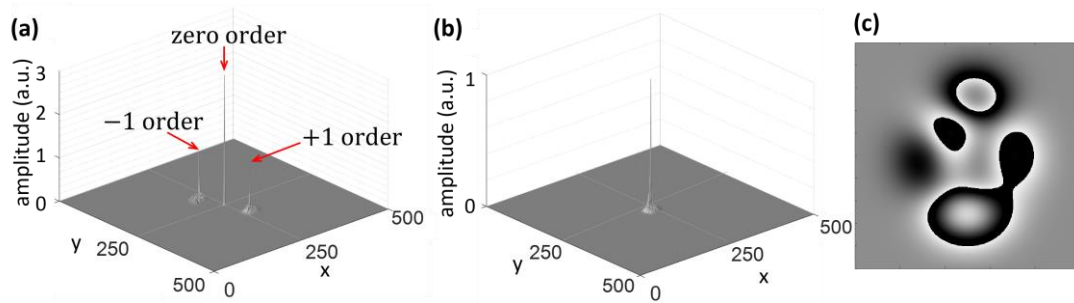


Figure 1-8: Remove carrier frequency with the Fourier transform for the example illustrated in Figure 1-7. a) Fourier domain of the fringe pattern which shows three main components, b) selected +1 order component by a Butterworth filter and shifted to the origin, and c) wrapped phase map.

The traditional Fourier method is the most popular method to wrap the phase since it is fast and reliable for smooth objects. However, this method requires accurate filtering to select the first order in the Fourier domain, which is performed manually. Moreover, the Fourier method extracts the phase map from the entire image at once; therefore, any non-stationary signals (such as shadowing or abrupt surface changes) can lead to a high level of phase ambiguity. Alternatively, as an extension of the FT method, the windowed Fourier transform (WFT) has been used to process the input fringe pattern window-by-window which helps to avoid spreading local phase ambiguities through the overall phase map [42]. In other words, this method localizes the frequency contents of the signal and does not need manual filtering.

1.3.1.1.2 Wavelet transform method

The wavelet is a well-known signal processing method with a variety of capabilities [43]. Recently, this method has been used as a tool to calculate the complex fringe pattern [43,44]. This method takes advantage of time and frequency multi-resolution analysis to alleviate the need for filters. The wavelet transform of a signal is a representation of that signal with a series of scaled and translated oscillating functions. The basis function is called the mother wavelet which must have a limited duration and shape to resemble the features of interest in the signal. Scaling the mother wavelet allows

altering the frequency of the function to match with the features of the signal, and translating permits finding the location of the feature [43]. Many pre-defined mother wavelets have been proposed which show potential in different applications. In the case of processing a sinusoidal fringe pattern, Morlet is a proper choice to represent the carrier of the fringe pattern since it is the product of a Gaussian window and a sinusoidal carrier wave (shown in Figure 1-9). Zhong et al. mathematically proved that the phase of the fringe pattern is equivalent to the phase of the ridge of the fringe pattern calculated by continuous wavelet transform [45]. The ridge is the maximum of the absolute value of the Wavelet transform which shows the coefficients that provide the best match between the mother wavelet and the signal. Therefore, the phase retrieval algorithm involves applying continuous Wavelet transform over the fringe pattern, finding the ridge, and then finding the phase corresponding to the ridge.



Figure 1-9: Morlet function

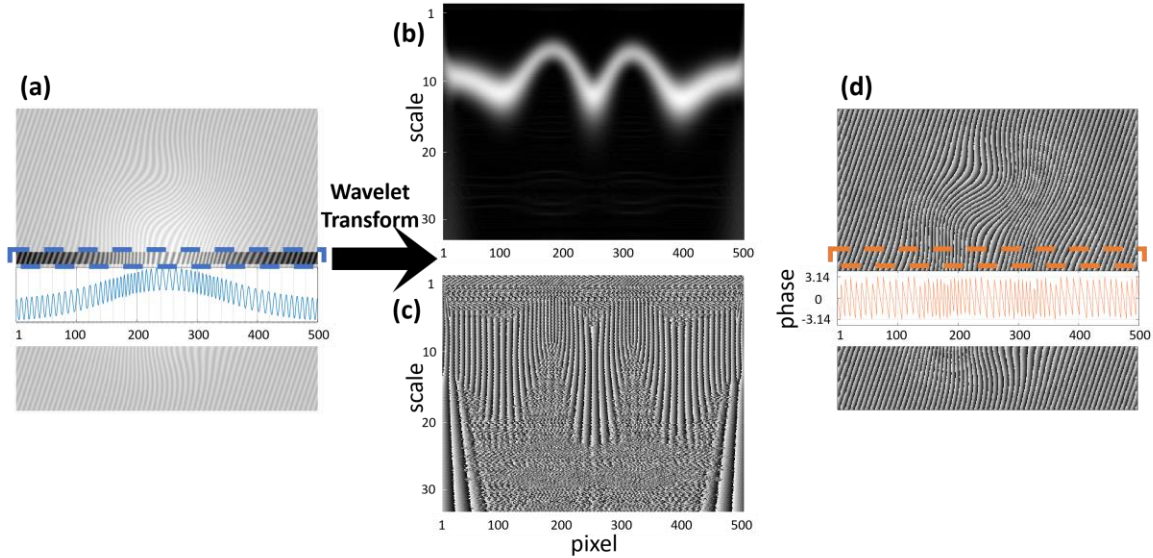


Figure 1-10: An example of the phase wrapping process with Wavelet transform for a simulated deformed fringe pattern with peaks function and gaussian background intensity (the fringe pattern frame size: 500×500 pixels and spatial frequencies: $(f_x = 20, f_y = 60)$). a) Selected row of the deformed fringe pattern along with the corresponding amplitude line profile. b) The amplitude and c) the phase of the Wavelet transform over the selected row (the mother function is Morlet and the applied scales are in the range of $[0.5, 32]$). d) The wrapped phase map was calculated based on finding the ridge of the Wavelet result along with the corresponding line profile.

1.3.1.1.3 Hilbert transform

Another method to calculate the complex amplitude of the fringe pattern is the Hilbert transform [46]. The Hilbert transform is a linear function that shifts all the frequency components of a signal by $-\pi/2$; in other words, it only alters the phase of the signal. Mathematically, the Hilbert transform of a signal $x(t)$ is the convolution of that signal with $1/\pi t$. Considering a fringe pattern as the input signal for this function (e.g., Figure 1-11 (a)), the result will provide the phase quadrature needed for wrapping the phase map (Figure 1-11 (b)). Then, applying an arctan function to the fringe pattern and the quadrature pattern provides the wrapped phase map (Figure 1-11 (c)). The simplicity of

the calculation and lack of the need for any filtering are the main advantages; however, the result is very dependent on the quality of the fringe pattern. Also, the Hilbert transform method requires that the fringe periods be completely contained within the image to avoid errors at the edges [47].

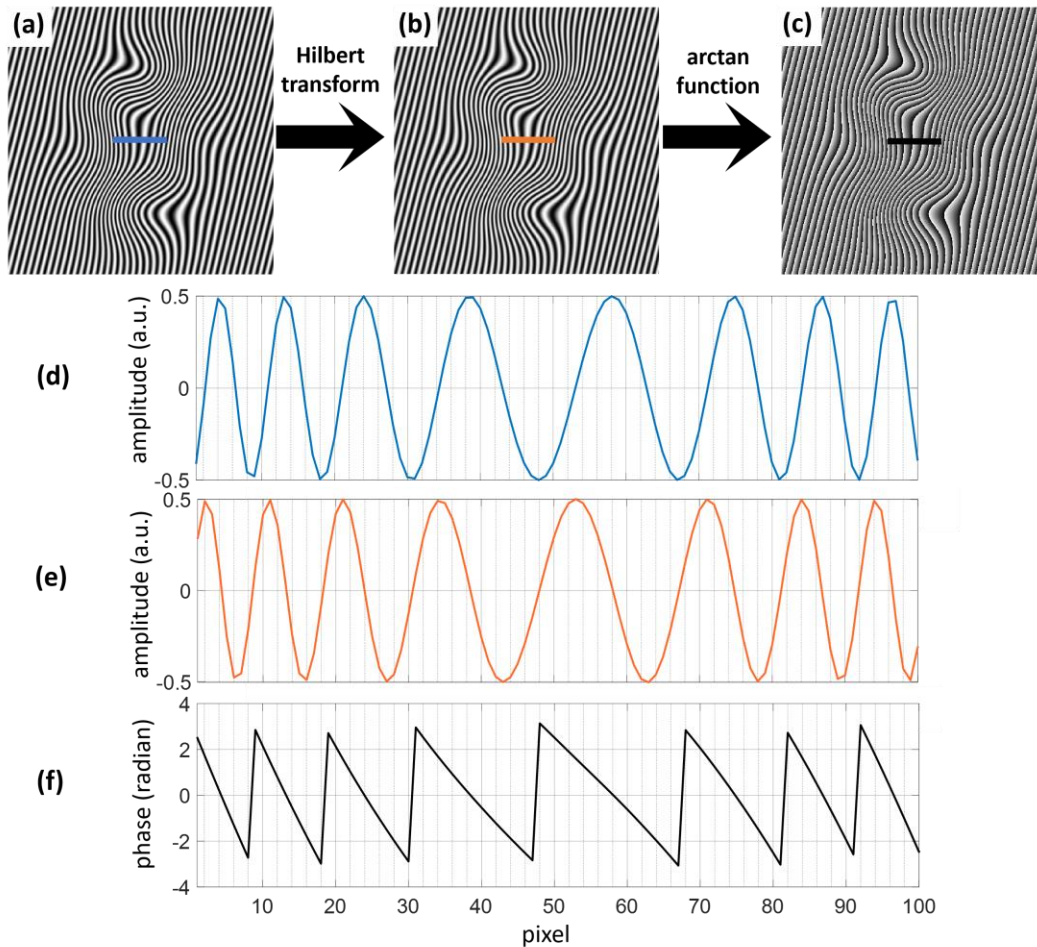


Figure 1-11: An example of the phase wrapping process with Hilbert transform. a) Deformed fringe pattern with peaks function and the size of 500×500 pixels. b) Hilbert transform of (a) which shows $-\pi/2$ phase-shift to the input signal. c) The wrapped phase which is calculated by $\arctan((b)/(a))$. d-f) Line profiles of the indicated regions of (a-c), respectively.

1.3.1.2 Temporal phase stepping

This group of techniques represents the demodulation of phase information based on solving a system of equations; it is also known as phase-shifting profilometry (PSP). The main advantages of such an approach are its capability for pixel-wise phase measurements and the fact that it is less reliant on the fringe pattern quality. The main disadvantage is the requirement for multiple acquisitions, which limits this approach to static and quasi-static measurements [40].

This method requires a series of phase-shifted fringe patterns to calculate a single wrapped phase map. The fringe patterns can be modeled as:

$$I_m(x, y) = a_m(x, y) + b_m(x, y) \cos[\varphi(x, y) + \delta_m] \quad (1-28)$$

where I_m indicates the acquired fringe pattern intensity in step number m ($m = 1, 2, \dots, M$), a_m is the background, b_m is the modulation intensity, φ is the phase of the object and the carrier, δ_m is the phase shift between step m and the first step, and δ_1 is assumed to be 0 (Figure 1-12). In this equation, the known variables are I_m and δ_m and the unknown variables are a_m , b_m , and φ . Systemically solving this equation with three unknowns requires at least three phase-shifted fringe patterns; therefore, the minimum number for M is three. The general solution for this system is in the form of [48]:

$$\varphi(x, y) = \arctan \left(\frac{\sum_{m=1}^M \alpha_m I_m}{\sum_{m=1}^M \beta_m I_m} \right) \quad (1-29)$$

where α_m and β_m are coefficients which are related to M , a_m , b_m , and δ_m . Many phase shifting scenarios have been proposed in the literature, most of which have been covered by Zuo's review paper [40]. Usually, it has been assumed that a_m and b_m are constant and equal for all phase-shifted fringe patterns, especially when the fringe projector is the same for all generated phase-shifted fringe patterns. Generally, all approaches differ based on three aspects: 1) the number of phase steps (i.e., M), 2) whether the number of

the phase steps are unknown or known, and 3) whether the phase steps are evenly distributed in the interval of $[0, 2\pi)$ or not.

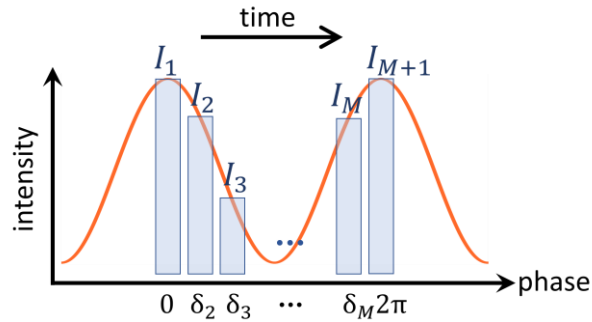


Figure 1-12: M-steps temporal phase stepping with even phase steps.

I_m s ($m = 1, 2, \dots, M$) indicate camera acquisitions over a specific pixel and the width of the rectangles indicates the integration time for the acquisitions. Adapted from [49].

1.3.2 Phase unwrapping

All previously explored phase retrieval algorithms produce a modulo- 2π phase map due to utilizing the arctan function. This means limiting the phase values to the range of $(-\pi, \pi)$ (Figure 1-13 (a) and (b)). Unwrapping algorithms are designed to detect the 2π indetermination values in the wrapped phase and compensate for them (Figure 1-13 (c) and (d)). This seems like a trivial procedure; however, a low-quality and noisy wrapped phase map can turn it into such a challenging task that for the past three decades, many researchers have continuously proposed different algorithms to improve the unwrapping procedure [50]. For more information on this field, refer to review articles such as [50–52].

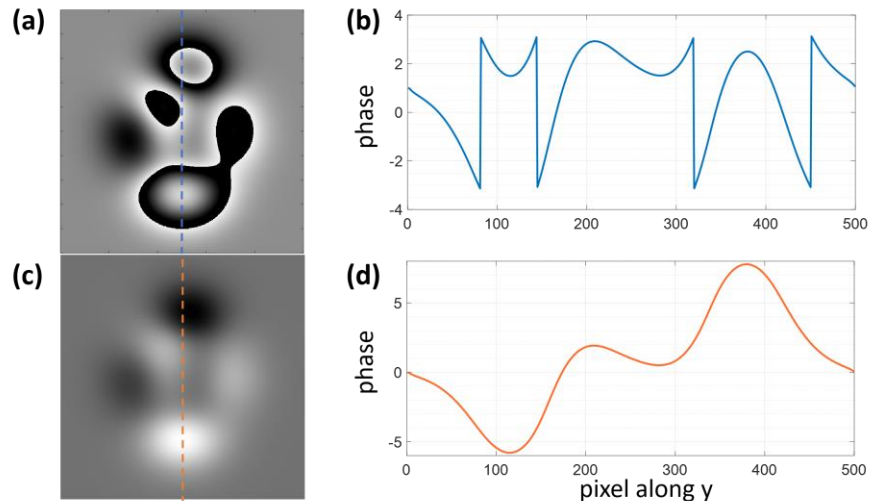


Figure 1-13: Phase unwrapping. a) simulated wrapped phase map with the size of 500×500 pixels, b) a line profile for the wrapped phase corresponding to column 250, c) unwrapped phase map, and d) line profile corresponding to (b).

1.4 Applications

The high demand for non-contact 3D measurements in biological imaging, production quality control, the entertainment industry, plastic surgery, etc., has led researchers to continue optimizing popular systems such as FPP and DHI. Usually, FPP systems are applicable for macroscopic imaging with millimeter-scale resolution and DHI systems have great potential for microscopic imaging with micrometer-scale and below resolution [4,53]. The topic of imaging speed has been of interest most recently and explored from the perspectives of static and quasi-static measurements and dynamic measurements.

1.4.1 Static and quasi-static measurements

In cases when the object is not moving or barely moving, the goal is to measure the surface topography, with the major concern of providing high accuracy and high lateral-axial resolution. Generally, sequential pattern projection is the best option to perform this task. In terms of processing methodology, the sequential patterns can be categorized into three techniques: 1) temporal phase stepping which is applicable for both DHI and FPP systems (refer to Section 1.3.1.2), 2) binary or grey level coding, only applicable for FPP

[54], and 3) temporal correlation method, only applicable for FPP [55]. In all cases, increasing the number of patterns can significantly improve the resolution at the expense of time.

1.4.2 Dynamic measurements

The main concerns for dynamic object measurements are the speed of pattern generation, the speed of image acquisition, and the robustness of the system to the motion artifacts. In the case of phase retrieval, the best method to satisfy dynamic imaging criteria is one that only needs a single fringe pattern to provide a reliable phase map (Section 1.3.1.1). However, these algorithms provide lower resolution and accuracy compared to the algorithms that use multiple fringe patterns. For algorithms that are based on carrier fringes, increasing the frequency of the fringes can improve the sensitivity of the system. However, this increase is limited by the spatial frequency of the detector, which means that the size of the fringe pattern must be distinguishable by the detector. Also, by increasing the fringe pattern frequency, the chance of phase ambiguity is increased. This is because by increasing the frequency it is more probable that a fringe will be deformed more than the pitch of the fringes, which is a common cause of phase ambiguity.

To increase the reliability of the system, researchers have tried to increase the number of patterns for a specific time slot. Two major methods that have been proposed are to increase the speed of the measuring system and to combine multiple patterns into a single acquisition. Because of the differences between FPP and DHI, we investigate the two systems separately.

- *FPP systems*

Since most FPP systems use digital projectors to cast fringe patterns, they have limited speed on the illumination side. Gong and Zhang have proposed a method to exceed projector speed by employing defocused binary stripes. However, the technique degrades fringe quality and affects the phase extraction performance [56]. In many cases, the fringe patterns have been produced using point light source projectors [57–61] or an array of point sources [62].

On the other hand, the speed of image acquisitions can be improved as well. To do so, researchers have adapted different methods such as using high-frame-rate cameras [59], one or multiple monochrome/color cameras where each camera acquires a single frame at a time [56–58,60–63], and multispectral cameras with the potential to capture multiple patterns that have been generated in different spectra in a single frame acquisition [64].

Moreover, another proposed method uses a composite pattern that modulates multiple fringe patterns in a single pattern [65]. By employing composite patterns, the purpose is to reduce the data acquisition time and maximize phase retrieval performance.

- *Off-axis DHI systems*

For off-axis DHI systems, there are three general approaches to increase the imaging speed.

1.4.2.1 Increasing the camera speed to capture the interferograms at fast frame rates

At this time, different groups have accomplished fast measurements by employing state-of-the-art technologies such as cameras with 4 000 [66], 100 000 [67], 500 000 [68], and even 1000 000 fps [69]. However, besides the fact that these technologies are costly, they also have a limited spatial resolution. This technical limitation occurs because decreasing the exposure time for the sensor limits the number of photons detected. Since an effective camera sensor must produce enough electronic charge from incident photons, the pixels must be increased in size to compensate for this shortcoming.

1.4.2.2 Capturing multiple interferograms in a single shot

For example, parallel phase-shifting can record multiple phase-shifted interferograms by a space-division-multiplexing technique, such that the temporal phase-stepping phase-retrieval algorithms can be applied [70,71]. Another example is multiwavelength DHI [69]. This method was developed primarily in order to obviate the phase wrapping problem and improve the resolution. For both of these examples, only a portion of the available pixels can be allocated to a single interferogram, which can adversely affect the spatial resolution.

1.4.2.3 Double-pulsed electronic speckle pattern interferometry (dp-ESPI)

This technique captures two speckle interferograms, one before the displacement and one at the moment of displacement. A speckle interferogram is a pattern of speckles that is the result of using a diffuse surface as the object in the interferometry system. A proper combination of the two speckle patterns reveals a fringe pattern that represents the contour of the displacement. dp-ESPI uses a pulsed laser to illuminate the surface and a double-exposure camera to sample vibrations in the scale of microsecond intervals. This method is more flexible than others for two reasons. First, it is less susceptible to environmental and mechanical noise. Since both speckle patterns share almost the same noise, the noise can be canceled out in the process of fringe generation. Second, the resolution of the recording medium is not a bottleneck for sensitivity [72].

1.5 Problem statement

Surface imaging in 3D has gained popularity in many fields, including the medical industry. It has been reported for use in plastic and reconstructive surgery, for the manufacturing and testing of implants, as well as for image guided and remote surgery. Depending on the size of the target and the required resolution, two methods are typically used. DHI provides highly accurate imaging of small targets. FPP handles large targets, but at a lower resolution. Both of these methods rely on phase modulation to perform the measurements. Despite the fact that these systems have been well documented in literature, there is still a lack of comprehensive processing software. A software package could be a leveraging point for the research in the field, where researchers (experts in coding or non-experts) could evaluate their own systems and compare their own processing algorithms to the well-known algorithms.

Traditional FPP techniques provide low-cost 3D macroscopic imaging, but with a tradeoff between accuracy and speed. To achieve greater accuracy, more fringe patterns must be projected onto the object, and more patterns require more time to produce, project, and capture. This could pose a problem if a real-time imaging system is needed to scan dynamic objects. Because objects of interest in medical applications are often

under motion (e.g. the beating heart), speed is critically important. Research in this field has proposed numerous systems to speed up imaging while keeping the accuracy at mm-scale, but as of yet it remains an open problem to be solved.

1.6 Research objectives

The aim of this research is twofold. First, to provide a comprehensive phase retrieval processing software. In this context, the first aim was to provide a user-friendly graphical-based software appropriate for both FPP and off-axis DHI systems. With FPP systems, the output typically consists of one or two fringe patterns and the goal is to extract topographical information from the fringe patterns retrieved phase map. As well, one or more interferograms are produced by off-axis DHI systems. In order to retrieve a phase map from an interferogram, it must first be reconstructed to find a focused wavefield of the object beam. Software for phase retrieval must have the ability to handle those two main tasks as well as all preparation and processing steps.

The second objective was to develop a 3D surface-shape measurement system based on FPP that is suitable for dynamic measurements. Multiple fringe patterns can be generated simultaneously by the proposed system. By having multiple fringe patterns in FPP, the measurement will be more accurate while reducing the need for multiple image captures. This will boost the functionality of FPP for dynamic and real-time imaging applications such as those of interest to the medical industry.

1.7 Thesis outline

This introduction is concluded by summarizing the contents of the thesis. Chapters 2 through 5 present individual studies that have been formatted in journal style. Chapter 2 presents a processing software tool designed for both FPP and off-axis DHI systems. Chapters 3 and 4 are associated with the FPP system and Chapter 5 describes an off-axis DHI system. These studies are described in more detail below.

The lack of both comprehensive and reliable software to retrieve a phase map from fringe patterns, and a reconstruction tool for DHI systems, motivated us to create an app that includes both these abilities. The app is presented in Chapter 2. It is designed with a

pipeline-based architecture and includes pre-processing (cropping, DC offset removal, filtering); fringe and phase extraction (hologram reconstruction, phase demodulation); and post-processing (denoising, masking, phase unwrapping, background removal, image enhancement). The app has been written in the MATLAB language. It brings together numerous algorithms for each step of the image processing pipeline and provides a graphical interface that can be used with or without expert knowledge in coding and algorithms. Moreover, the software supports add-ons for each step, which allows researchers with more advanced coding skills to either customize existing algorithms, or test their own custom algorithms, while remaining within the software pipeline. This software is intended for any and all users of FPP and off-axis DHI optical systems.

Chapter 3 presents multispectral fringe pattern profilometry. This novel method utilizes a multispectral filter array to generate multiple fringe patterns and uses a multispectral camera to capture all the patterns at once. Because in conventional FPP the quality of the phase map retrieved by phase demodulation algorithms is dependent on the orientation of the fringes (with respect to the object topographical features), we generate the fringe patterns oriented every 45° . This helps to assure a successful phase retrieval for at least one of the patterns when the object topography includes extreme slopes or sharp edges. Moreover, our method generates two complementary fringe patterns in every orientation. The complementary patterns are π -phase-shifted with respect to each other. Each pair of fringe patterns can be differenced to generate a differential fringe pattern that corrects for illumination offsets and mitigates the effects of glare from highly reflective surfaces.

As the number of phase-shifted fringe patterns in every orientation is less than three, we employed Fourier transform as a carrier-based phase demodulation method. In the process of Fourier phase retrieval, the lack of a DC offset enabled a wider bandwidth filter that extended toward lower frequencies without introducing a leak of the DC component into the chosen fundamental component. The wider bandwidth filter resulted in enhanced resolution during phase-demodulation and enabled lower frequency fringes to contribute to the extracted phase data. This resulted in a higher signal-to-noise ratio (SNR) for the phase map. This new multispectral method solves many practical problems

related to conventional fringe projection profilometry and doubles the effective spatial resolution. It is suitable for fast high-quality 3D profilometry at video frame rates.

In order to take advantage of the temporal phase stepping algorithms and avoid the requirement for manual filtering, we propose a new pattern for the FPP system, as explained in Chapter 4. This system is similar to that in the previous chapter, except that the multispectral array is designed to generate four phase-shifted fringe patterns in one orientation. Therefore, the phase retrieval computation uses temporal phase-shift algorithms in which the results are more accurate and automatic.

Together, Chapters 3 and 4 add a new composite pattern class named “multispectral composite pattern” to the existing classes that are categorized into grayscale and color composite patterns. Composite patterns allow for single-shot surface measurement applied to FPP systems. Single-shot imaging is a matter of concern when the object is moving. In these situations, the acquisition of all data that are required to retrieve a phase map should be less than the speed of the object movement or the object deformation. The multispectral composite pattern allows for the combination of more patterns without the problem of decomposition of the individual patterns, when compared to the other two composite pattern classes. Moreover, this new class alleviates the problem of leaking between different colors in the color composite pattern class.

Chapter 5 presents 3D static imaging with the off-axis DHI system. The algorithm that converted the acquired hologram into a 3D representation of reflective objects is presented in detail. The process includes the interferogram pre-processing, object wavefront reconstruction using discrete Fresnel transform, phase wrapping, phase unwrapping, background removal, and phase to height conversion.

The system was evaluated using a silicon-etched lateral-axial reflective resolution target that we have designed based on a standard resolution target named USAF. The system achieved 33 nanometer axial resolution and sub-pixel lateral resolution over a wide field of view of more than 10 mm x 10 mm. The algorithm will enable the digital holographic camera to be used for non-destructive testing of surface morphology at nanometer scales.

Chapter 6 summarizes our accomplishments and presents conclusions from the previous chapters. The conclusion is organized to reflect the initial objectives of the thesis.

1.8 References

1. M. Conroy and J. Armstrong, "A comparison of surface metrology techniques," *J. Phys. Conf. Ser.* 13, 458–465 (2005).
2. K. Schwenzer-Zimmerer, J. Haberstock, L. Kovacs, B. I. Boerner, N. Schwenzer, P. Juergens, H. F. Zeilhofer, and C. Holberg, "3D surface measurement for medical application - Technical comparison of two established industrial surface scanning systems," *J. Med. Syst.* 32, 59–64 (2008).
3. S. Van der Jeught and J. J. J. Dirckx, "Real-time structured light profilometry: A review," *Opt. Lasers Eng.* 87, 18–31 (2015).
4. G. Berkovic and E. Shafir, "Optical methods for distance and displacement measurements," *Adv. Opt. Photonics* 4, 441 (2012).
5. T. Bosch, M. Lescure, R. Myllyla, and M. Rioux, "Laser ranging: a critical review of usual techniques for distance measurement," *Opt. Eng.* 40, 10–19 (2001).
6. S. Zhang, "High-speed 3D shape measurement with structured light methods: A review," *Opt. Lasers Eng.* 106, 119–131 (2018).
7. V. S. Zapasskii, "the Talbot Effect: Recent Advances in Classical Optics," *Adv. Opt. Photonics* 5, 131–196 (2013).
8. C. Bond, D. Brown, A. Freise, and K. A. Strain, *Interferometer Techniques for*

Gravitational-Wave Detection (Springer International Publishing, 2016), Vol. 19.

9. S. Telfer and J. Woodburn, "The use of 3D surface scanning for the measurement and assessment of the human foot," *J. Addict. Nurs.* 3, 1–9 (2010).
10. K. C. Koban, L. Etzel, Z. Li, M. Pazos, S. Schönecker, C. Belka, R. E. Giunta, T. L. Schenck, and S. Corradini, "Three-dimensional surface imaging in breast cancer: A new tool for clinical studies?," *Radiat. Oncol.* 15, 1–8 (2020).
11. C. J. Moore, P. J. Sharrock, F. Lilley, and D. Burton, "3D body surface measurement and display in radiotherapy part II: Dynamic surface sensing and visualisation," *Proc. - Int. Conf. Med. Inf. Vis. - Biomed. Vis. MediVis 2006* 1, 103–108 (2006).
12. I. Dobrev, C. Furlong, J. T. Cheng, and J. J. Rosowski, "Optimization of a Lensless Digital Holographic Otoscope System for Transient Measurements of the Human Tympanic Membrane," *Exp. Mech.* 55, 459–470 (2015).
13. O. Volodarsky, Y. Hazan, and A. Rosenthal, "Ultrasound detection via low-noise pulse interferometry using a free-space Fabry-Pérot," *Opt. Express* 26, 22405 (2018).
14. X. G. Tian C, Feng T, Wang C, Liu S, Cheng Q, Oliver DE, Wang X, "Non-Contact Photoacoustic Imaging Using a Commercial Heterodyne Interferometer," *Physiol. Behav.* 176, 139–148 (2016).
15. X. Zhang, J. R. Fincke, C. M. Wynn, M. R. Johnson, R. W. Haupt, and B. W. Anthony, "Full noncontact laser ultrasound: first human data," *Light Sci. Appl.* 8, (2019).
16. Y. Hu, Q. Chen, S. Feng, and C. Zuo, "Microscopic fringe projection profilometry: A review," *Opt. Lasers Eng.* 106192 (2020).
17. S. S. Gorthi and P. Rastogi, "Fringe projection techniques: Whither we are?," *Opt. Lasers Eng.* 48, 133–140 (2010).

18. G. Fraenkel, M. Blewett, and M. Coles, "BT, a new vitamin of the B-group and its relation to the folic acid group, and other anti-anæmia factors," *Nature* 161, 981–983 (1948).
19. M. Andrulevičius, "Methods and applications of optical holography," *Medziagotyra* 17, 371–377 (2011).
20. H. Lichte, D. Geiger, and M. Linck, "Off-axis electron holography in an aberration-corrected transmission electron microscope," *Philos. Trans. R. Soc. A Math. Phys. Eng. Sci.* 367, 3773–3793 (2009).
21. M. K. Kim, "Principles and techniques of digital holographic microscopy," *SPIE Rev.* 1, (2010).
22. U. Schnars and W. Jüptner, "Direct recording of holograms by a CCD target and numerical reconstruction," *Appl. Opt.* 33, 179–181 (1994).
23. E. Cuche, P. Marquet, and C. Depeursinge, "Spatial filtering for zero-order and twin-image elimination in digital off-axis holography," *Appl. Opt.* 39, 4070–4075 (2000).
24. E. N. Leith and J. Upatnieks, "Reconstructed Wavefronts and Communication Theory," *J. Opt. Soc. Am.* 52, 1123–1130 (1962).
25. P. P. Urone, R. Hinrichs, K. Dirks, and M. Sharma, *Introduction to Wave Optics* (OpenStax, 2012).
26. G. Magyar, *Physical Optics* (SPRINGER SCIENCE+BUSINESS MEDIA, LLC, 1969), Vol. 20.
27. M. Kronrod, N. Merzlyakov, and L. Yaroslavskii, "Reconstruction of a Hologram with a Computer," *Sov. Phys. Tech. Phys.* 17, 333–334 (1972).
28. N. V. and M. Atlan and Institut, "Off-axis digital hologram reconstruction: some practical considerations N.," *Appl. Opt.* 50, 36–46 (2011).

29. C. S. Seelamantula, N. Pavillon, C. Depeursinge, and M. Unser, "Exact complex-wave reconstruction in digital holography," *J. Opt. Soc. Am. A* 28, 983–1011 (2011).
30. M. K. Kim, *Digital Holographic Microscopy Principles, Techniques, and Applications* (Springer, 2009).
31. U. Schnars and W. Juptner, "Digital recording and numerical," *Inst. Phys. Publ.* 13, 85–101 (2002).
32. E. Hecht, *Optics*, fourth (Addison Wesley, 2002).
33. M. Brezinski, "Optical Coherence Tomography: principles and applications," *J. Chem. Inf. Model.* 53, 1689–1699 (2006).
34. J. R. Mahan, N. Q. Vinh, V. X. Ho, and N. B. Munir, "Monte Carlo ray-trace diffraction based on the Huygens–Fresnel principle," *Appl. Opt.* 57, D56–62 (2018).
35. M. Janda, I. Hanák, and V. Skala, "Holography Principles Technical Report," no. DCSE/TR-2006-08 (2006).
36. M. Özcan and M. Bayraktar, "Digital holography image reconstruction methods," *Pract. Hologr. XXIII Mater. Appl.* 7233, (2009).
37. F. Wang, Z. Zeng, L. Wang, Y. Fu, G. Jiang, and H. Zhang, "A fast 3D shape measurement method based on sinusoidal and triangular fringe projection," *J. Mod. Opt.* 65, 136–144 (2018).
38. C. Y. Liu and C. Y. Wang, "Investigation of Phase Pattern Modulation for Digital Fringe Projection Profilometry," *Meas. Sci. Rev.* 20, 43–49 (2020).
39. S. Zhang, "Absolute phase retrieval methods for digital fringe projection profilometry: A review," *Opt. Lasers Eng.* 107, 28–37 (2018).
40. C. Zuo, S. Feng, L. Huang, T. Tao, W. Yin, and Q. Chen, "Phase shifting

- algorithms for fringe projection profilometry: A review," *Opt. Lasers Eng.* 109, 23–59 (2018).
41. M. Takeda and K. Mutoh, "Fourier transform profilometry for the automatic measurement of 3-D object shapes," *Appl. Opt.* 22, 3977–3982 (1983).
 42. Q. Kemao, "Two-dimensional windowed Fourier transform for fringe pattern analysis: Principles, applications and implementations," *Opt. Lasers Eng.* 45, 304–317 (2007).
 43. L. Chun-Lin, *A Tutorial of the Wavelet Transform* (2010).
 44. K. Pokorski and K. Patorski, "Separation of complex fringe patterns using two-dimensional continuous wavelet transform," *Appl. Opt.* 51, 8433–8439 (2012).
 45. R. Carmona, W. L. Hwang, B. Torresani, R. Carmona, W. L. Hwang, and B. Torresani, "Characterization of signals by the ridges of their wavelet transforms," *HAL* 45, 2586–90 (2015).
 46. M. Trusiak, Ł. Służewski, and K. Patorski, "Single shot fringe pattern phase demodulation using Hilbert-Huang transform aided by the principal component analysis," *Opt. Express* 24, 4221 (2016).
 47. P. K. Upputuri, K. M. Nandigana, and M. P. Kothiyal, "Single-shot interferometry techniques for optical testing," 24, 1317–1338 (2016).
 48. F. Willomitzer and G. Häusler, "Single-shot 3D motion picture camera with a dense point cloud," *Opt. Express* 25, 23451 (2017).
 49. P. de Groot and Zygo, "Principles of interference microscopy for the measurement of surface topography," *Adv. Opt. Photonics* 5, 131 (2014).
 50. X. Su and W. Chen, "Reliability-guided phase unwrapping algorithm: A review," *Opt. Lasers Eng.* 42, 245–261 (2004).
 51. T. R. Judge and P. J. Bryanston-Cross, "A review of phase unwrapping techniques

- in fringe analysis," *Opt. Lasers Eng.* 21, 199–239 (1994).
52. K. Rani and A. Shankar, "A Review on Phase Unwrapping Techniques in Interferometry," *Int. J. Adv. Res. Electron. Commun. Eng.* 6, 798–802 (2017).
 53. T. Luhmann, S. Robson, S. Kyle, and I. Harley, *Close Range Photogrammetry* (Whittles Publishing, 2015), Vol. 30.
 54. J. Geng, "Structured-light 3D surface imaging: a tutorial," *Adv. Opt. Photonics* 3, 128 (2011).
 55. A. Wiegmann, H. Wagner, and R. Kowarschik, "Human face measurement by projecting bandlimited random patterns," *Opt. Express* 14, 7692 (2006).
 56. Y. Gong and S. Zhang, "Ultrafast 3-D shape measurement with an off-the-shelf DLP projector," *Opt. Express* 18, 19743–19754 (2010).
 57. L. Chen, S. Yeh, A. Mario, and J. Chang, "3-D surface profilometry using simultaneous phase-shifting interferometry," *OPTICS* 283, 3376–3382 (2010).
 58. S. Heist, P. Lutzke, I. Schmidt, P. Dietrich, P. Kühmstedt, A. Tünnermann, and G. Notni, "High-speed three-dimensional shape measurement using GOBO projection," *Opt. Lasers Eng.* 87, 90–96 (2016).
 59. S. Heist, P. Dietrich, M. Landmann, P. Kühmstedt, G. Notni, and A. Tünnermann, "GOBO projection for 3D measurements at highest frame rates : a performance analysis," *Light Sci. Appl.* 7, 1–13 (2018).
 60. J. Hyun, G. Chiu, and S. Zhang, " High-speed and high-accuracy 3D surface measurement using a mechanical projector," *Optics express*, 26(2), 1474-1487 (2018).
 61. H. Zhang, Q. Zhang, Y. Li, and Y. Liu, "High Speed 3D Shape Measurement with Temporal Fourier Transform Profilometry," *Appl. Sci.* 9, 4123 (2019).
 62. N. G. Heist S, Mann A, Kühmstedt P, Schreiber P, "Array projection of aperiodic

- sinusoidal fringes for high-speed three-dimensional shape measurement," *Opt. Eng.* 53, 112208 (2014).
63. T. Wakayama, "High-speed three-dimensional shape measurements using multiwavelength spatiotemporal phase shifting," *Opt. Eng.* 53, 112207 (2014).
 64. C. Zhang, A. Breitbarth, A. Brahm, A. Breitbarth, M. Rosenberger, and G. Notni, "Single-frame three-dimensional imaging using spectral-coded patterns and multispectral snapshot cameras," *Opt. Eng.* 57, 123105 (2018).
 65. Z. H. Zhang, "Review of single-shot 3D shape measurement by phase calculation-based fringe projection techniques," *Opt. Lasers Eng.* 50, 1097–1106 (2012).
 66. C. Pérez-López, M. H. D. la Torre-Ibarra, and F. M. Santoyo, "Very high speed cw digital holographic interferometry," *Opt. Express* 14, 9709 (2006).
 67. J. Poittevin, P. Picart, F. Gautier, and C. Pezerat, "Design of a vibration probe based on high-speed digital holography," *Proc. Int. Conf. Struct. Dyn.*, 2121–2126 (2014).
 68. N. A. Buchmann, C. Atkinson, and J. Soria, "Ultra-high-speed tomographic digital holographic velocimetry in supersonic particle-laden jet flows," *Meas. Sci. Technol.* 24, 024005 (2013).
 69. P. Xia, Y. Awatsuji, K. Nishio, and O. Matoba, "One million fps digital holography," *Electron. Lett.* 50, 1693–1695 (2014).
 70. T. Tahara, R. Yonesaka, S. Yamamoto, T. Kakue, P. Xia, Y. Awatsuji, K. Nishio, S. Ura, T. Kubota, and O. Matoba, "High-speed three-dimensional microscope for dynamically moving biological objects based on parallel phase-shifting digital holographic microscopy," *IEEE J. Sel. Top. Quantum Electron.* 18, 1387–1393 (2012).
 71. Y. Awatsuji, M. Sasada, and T. Kubota, "Parallel quasi-phase-shifting digital holography," *Appl. Phys. Lett.* 85, 1069–1071 (2004).

72. L. Huff, "Holography and holographic instruments," in *OPTICAL INSTRUMENTS* (2010), pp. 1–30.

Chapter 2

2 PhaseWare: phase map retrieval for fringe projection profilometry and off-axis digital holographic interferometry

Publication status: The chapter has been published as a paper in the Elsevier journal, SoftwareX (<https://doi.org/10.1016/j.softx.2020.100652>).

2.1 Abstract

Non-contact optical surface measurement and movement tracking techniques have many applications but can be difficult to implement due to the complex software involved. We introduce a MATLAB-based graphical application that performs phase map retrieval for fringe projection profilometry and off-axis digital holographic interferometry. Designed with a pipeline-based architecture, PhaseWare assembles the most commonly used techniques and includes pre-processing (cropping, DC offset removal, filtering); fringe and phase extraction (hologram reconstruction, phase demodulation); and post-processing (denoising, masking, phase unwrapping, background removal, image enhancement).

2.2 Motivation and significance

Fringe projection profilometry (FPP) and off-axis digital holographic interferometry (DHI) are two optical techniques commonly used for non-contact 3D surface measurement. In FPP, fringe patterns are projected on to a target and distorted in shape by 3D surface features. The phase component of the distorted fringes, which encodes the 3D profile of the surface, can be retrieved from an image of the pattern captured with a 2-dimensional (2D) camera [1]. In off-axis DHI, a coherent light source is split into a reference and an object beam. After the object beam is scattered by a target object, the two beams are combined at a small angle, resulting in interferometric fringe patterns that contain information about the morphology of the 3D surface of the object [2]. Since both FPP and off-axis DHI result in similar fringe pattern measurements, they tend to use similar algorithms to extract 3D surface morphology, albeit FPP tends to be more suitable for macroscopic morphology and DHI for microscopic morphology [3].

2.3 Algorithms used in PhaseWare

The common feature of these two techniques is the requirement to demodulate the phase information from the fringes. There are currently many algorithms that can be used to extract the phase information generated by FPP and DHI. However, there is no single tool encompassing these systems in a user-friendly package. As such, there is a barrier to entry for these techniques for most research environments because of the need for an expert in the field to analyze the data. PhaseWare was designed to overcome this expertise barrier (Figure 2-1).

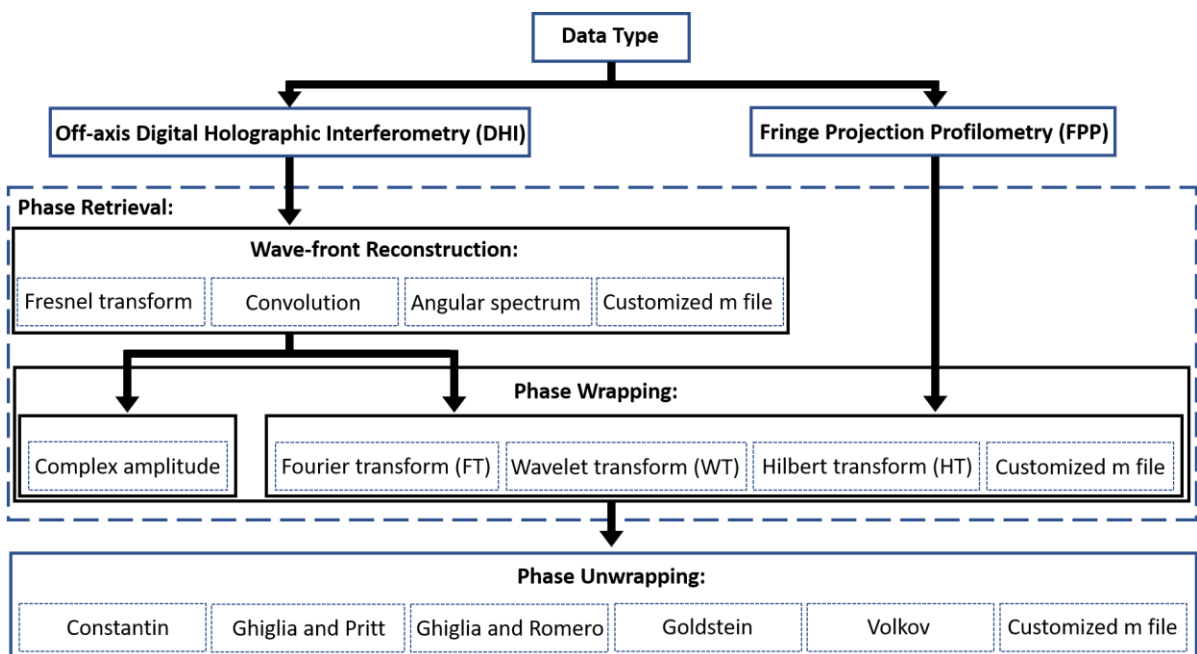


Figure 2-1: Diagram describing the phase retrieval processing algorithms implemented in PhaseWare.

2.3.1 Fringe projection profilometry

The output of an FPP system is a series of 2D fringe patterns distorted in shape by surface features on the object. To recover the encoded surface shape, a phase retrieval processing method is used to extract the phase map from the fringes based on either a single fringe pattern or multiple patterns. These phase demodulation algorithms are categorized into two classes: carrier-based and phase shift-based.

Carrier-based techniques (spatial phase stepping) only need a single acquisition of a distorted fringe pattern to retrieve the phase map [1] [4]. The most popular method, generally known as the Fourier transform (FT) method, uses the fast Fourier transform (FFT) and a bandpass filter and is fast and reliable for smooth objects [5]. However, the FT method extracts the phase map from the entire image at once; therefore, any non-stationary signals (such as shadows or abrupt surface changes) can lead to a high level of phase ambiguity [6]. Alternatively, wavelet transform (WT) is used for non-stationary signals to take advantage of time and frequency multi-resolution analysis to overcome the need for filters [7] [8]. The WT method relies on the fact that the phase of the optical fringe pattern is equivalent to the phase of the ridge of the fringe pattern calculated by WT [9]. Another method is the Hilbert transform (HT). The HT of a sinusoidal signal produces a $\pi/2$ shift in phase without changing the amplitude. This feature can be used to extract the phase of a distorted fringe pattern [10]. As with FT, HT requires that the fringe periods be completely contained within the image to avoid errors at the edges [11]. The HT method is computationally less complex than both WT and FT and in contrast to FT, does not require filtering.

Phase shift-based techniques (temporal phase stepping) require at least three acquisitions with different phase-shifted fringe patterns. Compared to carrier-based techniques, these methods provide pixel-wise phase measurement, more accurate results, and are less sensitive to the quality of the acquired fringes [12]. However, these techniques require longer acquisition times, which results in increased susceptibility to environmental noise and vibration. Phase retrieval algorithms for these techniques use straightforward numerical equations. Standard N-step phase shifting is the most common algorithm but requires that the phase steps be evenly spaced within a 2π period. Further, other algorithms for known and unknown numbers of phase steps have been reported in the literature [12].

The current version of PhaseWare focuses on spatial phase stepping and does not include functions to extract a phase map from images acquired through temporal phase stepping. However, this functionality could be added by advanced users with add-ons.

2.3.2 Off-axis digital holographic interferometry

As mentioned earlier, off-axis DHI uses an optical fringe pattern created by the interference between a reference beam and an object beam, scattered from the target object. The holograms are acquired in quadrature using carrier-based and phase shift-based techniques and contain both amplitude and phase information [2]. These are recorded on an image plane situated at a set distance from the object and need to be reconstructed to obtain the object phase at the reconstruction/object plane. The reconstruction involves numerically illuminating and diffracting the holograms to reveal the field distribution as a complex-valued map in the reconstruction plane. This map includes the real and virtual images of the object such that one of them contains the amplitude and phase information, while the other is discarded. The most common DHI reconstruction algorithms are the discrete Fresnel transform, convolution, and angular spectrum [13].

The Fresnel-Kirchhoff and Rayleigh-Sommerfeld integrals describe light wave diffraction. According to these equations, in the case of paraxial approximation, when the distance between the recording camera and the object is sufficiently long, the diffraction integral can be simplified with a Fresnel transform [2] [14]. Further, because of the nature of digital imaging, only discrete samples of the holograms are recorded; thus, a discrete Fresnel transform needs to be applied to find the complex amplitude of the hologram at the desired focal distance. A discrete Fresnel transform can be implemented with a single FFT [2].

Another implementation of the wave diffraction equation is through spatial convolution between the hologram and an exponential term representing the Fresnel impulse response. The convolution equation can be calculated by using two or three FFTs [2].

Wave propagation can be numerically modeled as an angular spectrum, a method that decomposes the field into multiple plane waves and propagates them separately. At each point in space, the field can be calculated by summing the propagated plane waves taking care to include phase differences. Applying an angular spectrum transform function to hologram reconstruction requires one FFT and one inverse FFT [15] [16].

Once the holograms have been reconstructed into fringe patterns, they are essentially the same as those obtained with FPP and require a similar phase demodulation process. As with FPP, the size of the fringes directly affects the resolution of the phase measurements such that larger fringes are insensitive to small surface changes. The downside of using finer fringes is that they are more sensitive to noise. In an off-axis DHI system, changing the off-axis angle alters the fringe size such that a larger angle produces smaller fringes. This angle should be chosen to satisfy the Shannon sampling theorem [17].

PhaseWare assembles many available algorithms for FPP and off-axis DHI, and puts them into the hands of any researcher with only a basic background in coding. As well, the software supports add-ons, which allows researchers with more advanced coding skills to either customize existing algorithms or test their own custom algorithms while remaining within the software pipeline. This software is intended for any and all users of FPP and off-axis DHI optical systems. Rather than needing to compile a full code base, users can simply validate their system by loading data into PhaseWare and executing the pipeline, thereby simplifying the data processing and reducing the time to results.

2.4 Software description

PhaseWare is a software package designed in MATLAB app designer 2019a. The main goal is to retrieve phase maps from FPP and off-axis DHI measurements. This phase information can be used to compute 3D images of an object or track the surface deformation of an object. This software can be installed in the MATLAB APPS section to take advantage of a graphic user interface. Note that MATLAB Image Processing, Wavelet, Optimization, and Deep Learning Toolboxes are prerequisites for some functions in this software package.

2.4.1 Software architecture

The software was designed as a multi-stage pipeline architecture (Figure 2-2). At each stage, the most commonly used algorithms available in the literature are made available along with the potential for user-supplied algorithms (add-ons) to customize the software. Custom algorithms allow users to adapt the software to their specific hardware circumstances, improve upon existing algorithms, and test new approaches.

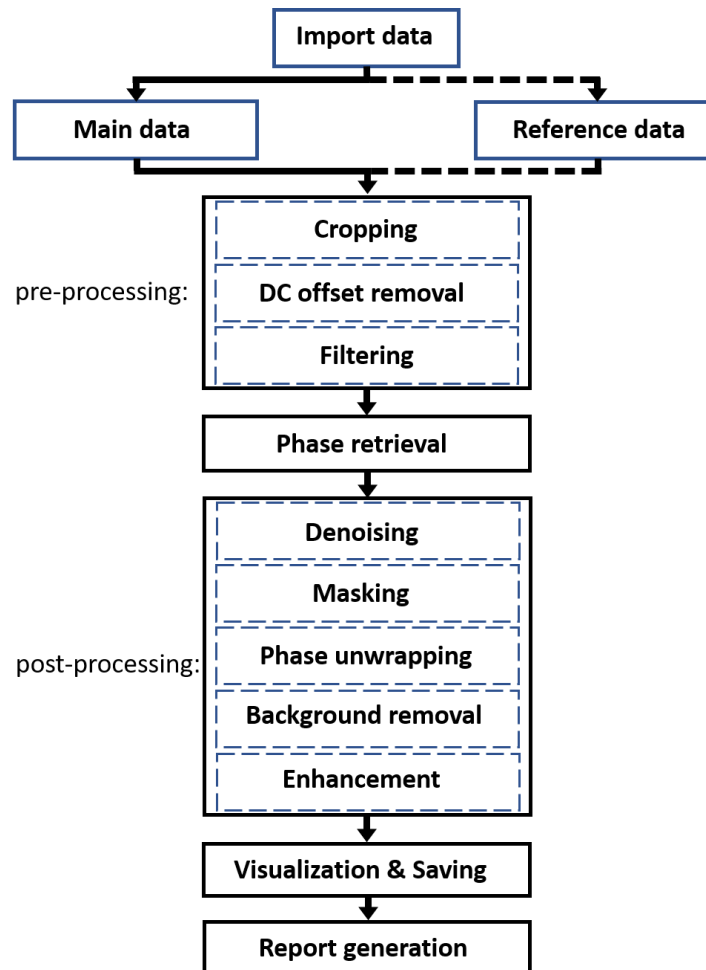


Figure 2-2: Diagram of PhaseWare software architecture. The imported data contains the required main data and optional reference data, which is passed to pre-processing, phase retrieval, and post-processing algorithms. The software provides tools for data visualization, data saving, and report generation in Microsoft Word format.

The available data input options include Main Data and Reference Data. The Main Data input is for the raw data captured from the imaging system for a specific object, and the Reference Data input is for the raw data captured from the imaging system without an object. The Main Data input can be a single image or a series of images and is required for the software to run. The Reference Data input must be a single image and is optional.

The first step of the process is to apply pre-processing to the raw input data. The pre-processing stage contains three modules: cropping the region of interest (RoI), DC offset removal, and filtering for noise-reduction.

After preparing the data, the phase retrieval stage extracts the phase map using an algorithm matched to the imaging system. The output of this step is a 2π -wrapped phase map with and without the carrier frequency.

The wrapped phase map may contain some level of noise that is dependent on the type of imaging system. Here, the software introduces a post-processing stage for noise reduction and a method to compute the absolute phase map. This stage can take a phase map with or without a carrier as an input and applies a user-selected denoising function. Next, the software introduces an optional mask selection step to mask out noisy regions of the signal, which is performed manually with user selection of a RoI through a pop-up graphical interface.

In the next step, the phase map is unwrapped to generate the absolute phase map. Five different algorithms are included in PhaseWare for phase unwrapping, with the option for user-defined algorithms. The included algorithms are adapted from the following works: Constantini [18], Ghiglia and Pritt [19], Ghiglia and Romero [20], Goldstein [21], and Volkov [22].

The non-uniformity of the illumination and imaging systems have effects on the calculated absolute phase. To negate these effects, PhaseWare provides a background removal tool with three options. First, manual background selection allows the user to select some indicative sampling points on the background and assign a polynomial fitting function, which is then interpolated to estimate the background. Second, automatic

background estimation attempts to find small variations in intensity and subtract them from the phase map. Finally, a reference input may also be used.

Results generated by PhaseWare are summarized in a software-generated report, which provides a log of the procedures performed on the input data for easy comparison between experiments.

2.5 Illustrative Examples

2.5.1 Fringe projection profilometry example

In this section, we generated two simulated sets of fringe patterns to demonstrate the capabilities of PhaseWare. In each case, FT, WT, and HT were used to estimate the wrapped phase maps, which were then unwrapped using the Ghiglia and Romero function. The first fringe pattern was a reference pattern of 100 vertical sinusoidal fringes in a 1,000 by 1,000 pixel image (Figure 2-3 (a)). This was then processed using the MATLAB *peaks* function to produce the Main Data (Figure 2-3 (b)). The second pattern set is identical, but with added Gaussian noise (zero-mean, variance at one percent of the original reference fringe patterns, Figure 2-3 (f), Figure 2-3 (g)).

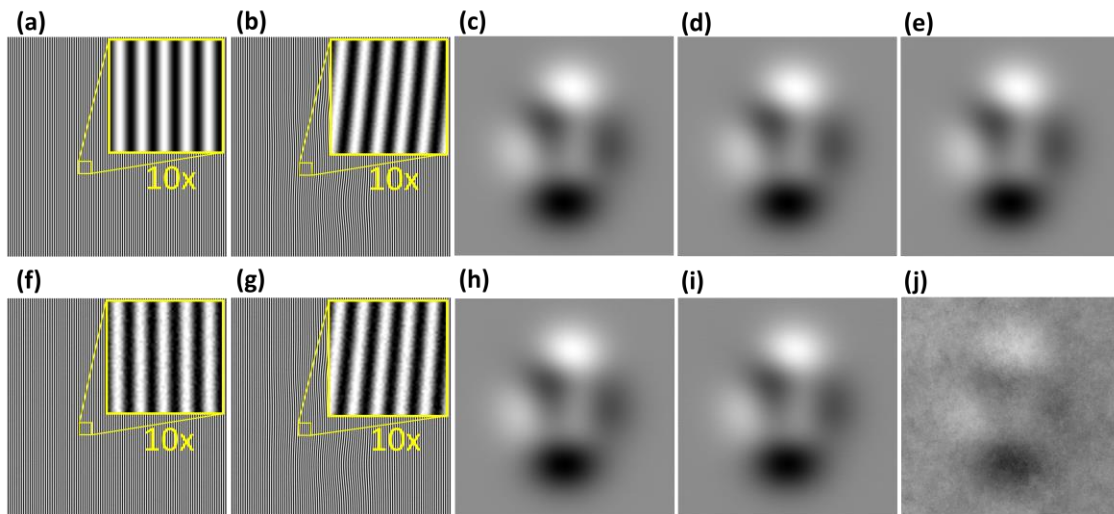


Figure 2-3: Fringe projection profilometry example using data generated by processing a sinusoidal function with the MATLAB *peaks* function. Reference (a) and Main (b) Data for the noiseless pattern. Unwrapped phase maps retrieved using

FT (c), WT (d), and HT (e). Reference (f) and Main (g) Data for data with added Gaussian noise. Unwrapped phase maps for the latter case retrieved using FT (h), WT (i), and HT (j).

For each set of fringe patterns, PhaseWare was used to retrieve the absolute phase maps and calculate the phase change. These maps were then wrapped using FT (Figure 2-3 (c), (h)), WT (Figure 2-3 (d), (i)), and HT (Figure 2-3 (e), (j)). In each case, the top image shows the original pattern and the bottom image shows the pattern with Gaussian noise. Figure 2-4 shows the peak signal-to-noise ratio (PSNR) in each case as a performance metric. As an example, in Figure 2-5 (a) and Figure 2-5 (b), the line profiles at pixel row 500 were compared between methods and to the original function.

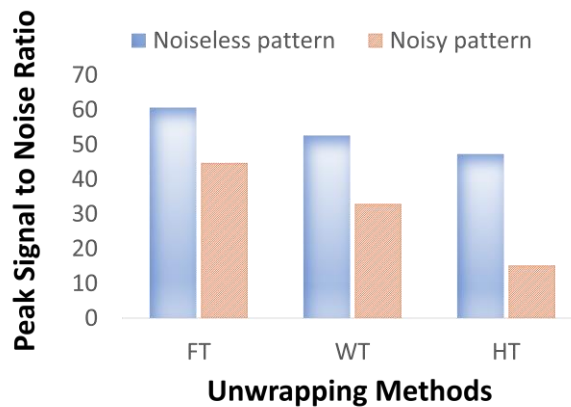


Figure 2-4: Peak signal-to-noise ratio comparison for the fringe projection profilometry example between the noiseless and noisy patterns.

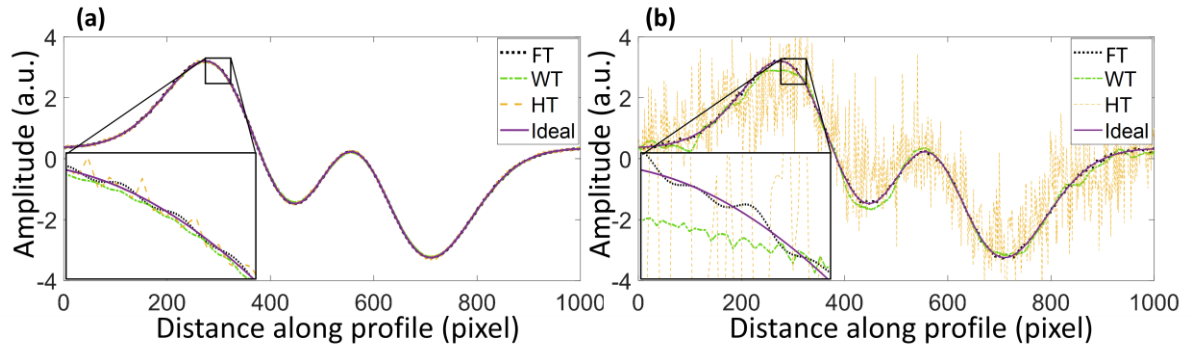


Figure 2-5: Line profile analysis of the fringe projection profilometry example at pixel row 500 for noiseless (a) and noisy (b) images.

2.5.2 Off-axis digital holographic interferometry example

For this example, we present a case where a raw hologram acquired using an off-axis DHI system was processed through the PhaseWare pipeline (Figure 2-6) [23,24]. As a target object, a reflective surface with 80-nm deep etched features was used (Figure 2-6 (a)). First, the raw hologram was imported and represents the Main Data. No Reference Data was used. The data was then cropped, the DC offset removed, padded with zeros, and filtered (Figure 2-6 (b)). Next, as shown in Figure 2-6 (c), the Fresnel reconstruction method resulted in an amplitude map of the reconstructed complex field containing both the virtual and real components. In this case, the in-focus image was in the real component, which was then used to generate the corresponding phase map (Figure 2-6 (d)). Using the FT method, the carrier frequencies were then removed from the image (Figure 2-6 (e)), after which the Goldstein algorithm was used to unwrap the remaining phase information (Figure 2-6 (f)). Finally, the background was subtracted with automatic background estimation resulting in Figure 2-6 (g) and Figure 2-6 (h).

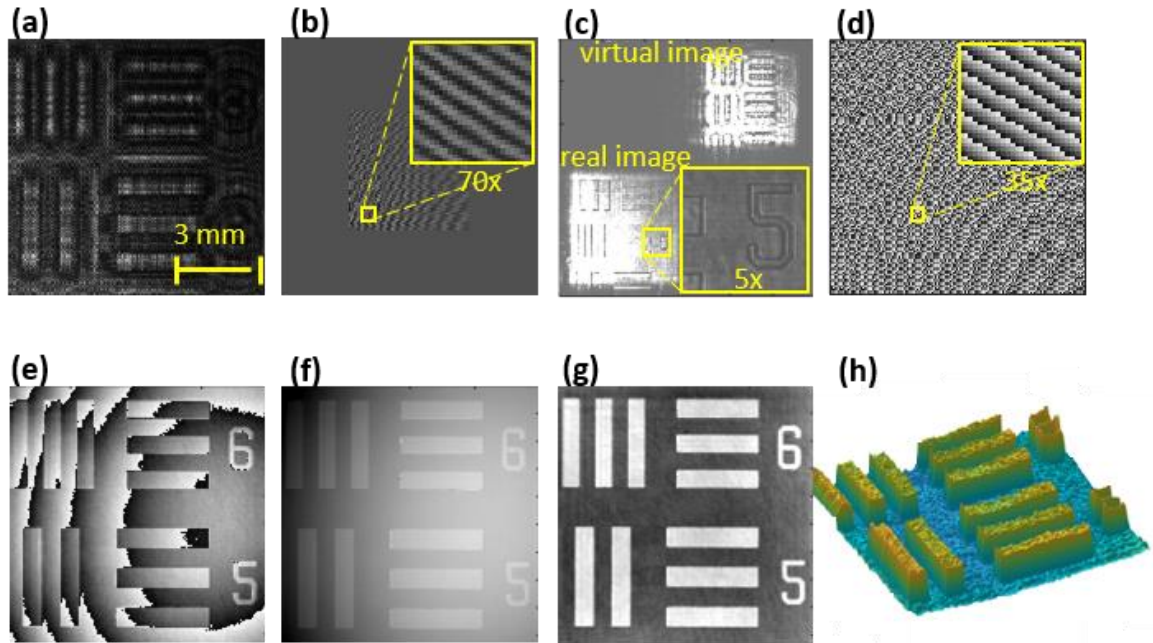


Figure 2-6: Processing of a hologram obtained by an off-axis DHI system [23,24]. a) Raw hologram of a USAF resolution target etched into a gold-coated silicon wafer (features measure 80 nm in depth). b) Image after cropping, DC offset removal, zero padding, and filtering. c) Amplitudes of the reconstructed complex image containing real and virtual components. d) Wrapped phase map with Fourier method corresponding to the real component. e) Carrier-removed phase-demodulated image. f) Absolute phase map obtained by unwrapping data in panel (e). g) Phase-unwrapped image after background subtraction. h) 3D representation of the object based on the absolute phase map with background removed.

2.6 Impact

PhaseWare is a platform for processing data from non-contact optical 3D measurement techniques. It facilitates image reconstruction, accelerates workflows, and is poised to assist non-expert researchers and experts alike. PhaseWare has the potential to accelerate research in FPP and DHI since it 1) brings together numerous algorithms for each step of the image processing pipeline and 2) provides a graphical interface that can be used with or without expert knowledge in coding and algorithms.

One area where we see PhaseWare providing benefit is for research groups just beginning to foray into non-contact optical 3D measurements, whether this is with FPP or off-axis DHI. There are two main barriers to entry for these groups. First, creating the desired imaging setup itself can be difficult without a method to validate the acquired data. PhaseWare can be used directly after data acquisition, at every step, and after each setup modification to assess system performance. Second, due to the complexity of the reconstruction algorithms, it can be difficult and time-consuming for researchers to decide which algorithms to use, find the relevant code, and adapt the code to the application. PhaseWare can potentially save researchers time and effort with an out-of-the-box solution that enables researchers to focus on the application rather than the complexities of algorithms needed for development of non-contact optical 3D measurement techniques.

Even for experienced researchers with coding expertise, it makes sense to have an easy-to-use and readily accessible software solution. PhaseWare benefits these advanced users by providing a plug-in architecture that allows custom user-created algorithms to be inserted at key steps of the pipeline. Users can easily plug-in their preferred methods and benefit from PhaseWare's graphical interface allowing easy comparison between a custom algorithm and established methods.

With this software available on Github, the research community will be able to contribute to the project. As new algorithms are investigated and published, they can be incorporated into PhaseWare enabling rapid adoption by a much broader community of users.

2.7 Conclusions

Non-contact interferometric surface measurements have many applications but have been traditionally difficult to implement due to the complexity of both the instrumentation and the data processing and reconstruction algorithms. PhaseWare seeks to simplify the data processing and image reconstruction procedures by providing an easy-to-use graphical

front-end to many commonly used techniques and algorithms in the field of non-contact 3D optical measurement.

2.8 Conflict of Interest

We wish to confirm that there are no known conflicts of interest associated with this publication and there has been no significant financial support for this work that could have influenced its outcome.

2.9 Acknowledgements and funding sources

This work was supported by the Natural Sciences and Engineering Research Council [grant number RGPIN-2014-04769] and the Canadian Institutes of Health Research [grant number 356794]. PO and HW were also supported through studentship awards provided by the Lawson Health Research Institute, while LY was supported through a studentship funded by the Breast Cancer Society of Canada.

2.10 Code metadata

Table 2-1: Code metadata for PhaseWare including: links for the software package, all the .m files used in the software, manual for the users, licensing information, and requirements.

Current code version	v0.3
Permanent link to code/repository used for this code version	https://github.com/ElsevierSoftwareX/SOFTX-D-20-00036
Code Ocean compute capsule	Not applicable
Legal Code License	GNU General Public License v3.0
Code versioning system used	Github
Software code languages, tools, and services used	MATLAB

Compilation requirements, operating environments & dependencies	MATLAB 2019a or newer; Image Processing, Wavelet, Optimization, and Deep Learning Toolboxes
If available Link to developer	https://github.com/Lawson-Optics-Lab/PhaseWare/tree/master/docs
Support email for questions	jcarson@lawsonimaging.ca

2.11 References

1. S. S. Gorthi and P. Rastogi, "Fringe projection techniques: Whither we are?," *Opt. Lasers Eng.* 48, 133–140 (2010).
2. N. V. and M. Atlan and Institut, "Off-axis digital hologram reconstruction: some practical considerations N.," *Appl. Opt.* 50, 36–46 (2011).
3. H. I. Luhmann T, Robson S, Kyle S, "Close range photogrammetry. Close range photogrammetry: Principles, techniques and applications.," Revis. Ed. Whittles Publ. 528 (2006).
4. M. J. Badulescu C, Bornert M, Dupré JC, Equis S, Grédiac M and V. V. Picart P, Rotinat R, "Demodulation of spatial carrier images: Performance analysis of several algorithms using a single image. *Exp Mech*," 53, 1357–70 (2013).
5. X. U. Su, "Fourier transform profilometry: a review," *Opt. Lasers Eng.* 35, 263–284 (2001).
6. J. Zhong and J. Weng, "Spatial carrier-fringe pattern analysis by means of wavelet transform: Wavelet transform profilometry," *Appl. Opt.* 43, 4993–4998 (2004).
7. J. Zhong and J. Weng, "Phase retrieval of optical fringe patterns from the ridge of a wavelet transform," *Opt. Lett.* 30, 2560 (2005).

8. C. Jiang, S. Jia, J. Dong, Q. Lian, and D. Li, "Multi-frequency fringe projection profilometry based on wavelet transform," *Opt. Express* 24, 11323 (2016).
9. L. Huang, Q. Kemao, B. Pan, and A. K. Asundi, "Comparison of Fourier transform, windowed Fourier transform, and wavelet transform methods for phase extraction from a single fringe pattern in fringe projection profilometry," *Opt. Lasers Eng.* 48, 141–148 (2010).
10. M. T. Nguyen, Y. S. Ghim, and H. G. Rhee, "Single-shot deflectometry for dynamic 3D surface profile measurement by modified spatial-carrier frequency phase-shifting method," *Sci. Rep.* 9, 1–15 (2019).
11. P. K. Upputuri, K. M. Nandigana, and M. P. Kothiyal, "Single-shot interferometry techniques for optical testing," 24, 1317–1338 (2016).
12. C. Zuo, S. Feng, L. Huang, T. Tao, W. Yin, and Q. Chen, "Phase shifting algorithms for fringe projection profilometry: A review," *Opt. Lasers Eng.* 109, 23–59 (2018).
13. T. M. Kreis, M. Adams, and W. P. Jüptner, "Methods of Digital Holography : A Comparison," 3098, 224–233 (1997).
14. N. Verrier and M. Atlan, "Off-axis digital hologram reconstruction: Some practical considerations," *Appl. Opt.* 50, (2011).
15. K. Matsushima and T. Shimobaba, "Band-Limited Angular Spectrum Method for Numerical Simulation of Free-Space Propagation in Far and Near Fields," 17, 1668–1670 (2009).
16. K. M. Yu L, "Wavelength-scanning digital interference holography for tomographic three-dimensional imaging by use of the angular spectrum method," 30, 2092 (2005).
17. N. Demoli, H. Halaq, K. Šariri, and M. Torzynski, "Undersampled digital holography," 17, 15842–15852 (2009).

18. M. Costantini, "Based on Network Programming," October 36, 813–821 (1998).
19. P. M. Ghiglia DC, *Two-Dimensional Phase Unwrapping : Theory, Algorithms, and Software*. (WILEY, 1998).
20. R. L. Ghiglia DC, "Robust two-dimensional weighted and unweighted phase unwrapping that uses fast transforms and iterative methods.," *J Opt Soc Amer* 11, 107 (1994).
21. W. C. Goldstein RM, Zebker HA, "Satellite radar interferometry: Two-dimensional phase unwrapping.," *Radio Sci* 23, 713–20 (1988).
22. Z. Y. Volkov VV, "Deterministic phase unwrapping in the presence of noise.," *Opt Lett* 28, 2156 (2003).
23. H. Wang, P. Omid, J.J.L. Carson, M. Diop "Holographic camera for non-contact measurement of nanoscale surface heights.," *Bjelkhagen HI, Bove VM, Ed. Pract. Hologr. XXXIII Displays, Mater. Appl.* 10944, SPIE; 32 (2019).
24. P. Omid, H. Wang, M. Diop, J.J.L. Carson "Algorithm for phase-displacement conversion from reflection digital holographic interferometry.," *Bjelkhagen HI, Bove VM, Ed. Pract. Hologr. XXXIII Displays, Mater. Appl.* SPIE; 25 (2019).

Chapter 3

3 Single-shot detection of 8 unique monochrome fringe patterns representing 4 distinct directions via multispectral fringe projection profilometry.

Publication status: The chapter has been published as a paper in the Scientific Reports journal, (<https://www.nature.com/articles/s41598-021-88136-4>).

3.1 Abstract

Spatial resolution in three-dimensional fringe projection profilometry is determined in large part by the number and spacing of fringes projected onto an object. Due to the intensity-based nature of fringe projection profilometry, fringe patterns must be generated in succession, which is time-consuming. As a result, the surface features of highly dynamic objects are difficult to measure. Here, we introduce multispectral fringe projection profilometry, a novel method that utilizes multispectral illumination to project a multispectral fringe pattern onto an object combined with a multispectral camera to detect the deformation of the fringe patterns due to the object. The multispectral camera enables the detection of 8 unique monochrome fringe patterns representing 4 distinct directions in a single snapshot. Furthermore, for each direction, the camera detects two π -phase shifted fringe patterns. Each pair of fringe patterns can be differenced to generate a differential fringe pattern that corrects for illumination offsets and mitigates the effects of glare from highly reflective surfaces. The new multispectral method solves many practical problems related to conventional fringe projection profilometry and doubles the effective spatial resolution. The method is suitable for high-quality fast 3D profilometry at video frame rates.

3.2 Introduction

Fringe projection profilometry (FPP) is a three-dimensional (3D) surface imaging technique that employs optical deflectometry to detect surface morphology of specular objects [1]. The technique has been successfully used in machine vision and medical imaging applications, where non-contact, full-field, and high-speed capabilities are needed. The FPP method projects fringe patterns on to an object and derives depth and height information from the phase distribution of the deformed fringes captured by one or more cameras. Generally, capturing more patterns leads to more accurate phase estimates, but the sequential projection of the patterns lengthens acquisition time and may not be suitable for highly dynamic measurements [2]. This situation has motivated many groups to develop methods to improve the speed of FPP through the use of fast switching digital projectors that cast fringes using monochromatic or RGB colored light [3–9]. To further enhance FPP speed, attempts have been made to generate multiple fringe patterns simultaneously. For example, groups have superimposed multiple fringe patterns each with a different spatial frequency [10,11], a different color [12,13], or different orientation [3,4,14–16]. Other groups have replaced the digital projector with faster devices. For example, Wakayama et al. (2014) used a fringe generation method that used three laser diodes and an electronically-controlled mirror to generate temporally phase-shifted fringe patterns at different wavelengths [17]. Zhang et al. performed multiwavelength fringe illumination with eight different light-emitting diodes in combination with a multispectral camera [18]. The main advantage of this approach was that multiple fringe patterns were acquired in a single snapshot with each camera exposure, thereby overcoming the limitations of sequential pattern projection and imaging. However, the system was large due to the large number of separate projection coordinates.

Phase distribution maps are computed from FPP data using a phase-demodulation algorithm. Algorithms can be categorized as phase-shifting (temporal phase stepping) and carrier-based (spatial phase stepping). The former requires at least three fringe patterns with known phase-step and generates accurate pixel-wise phase maps with minimal computational effort [19]. Phase maps retrieved from snapshots of fringe patterns can be

computed with transform-based algorithms that utilize the Fourier transform (FT) [20], windowed FT [3,21], Wavelet transform [22], or Hilbert transform [23]. Since these methods result in phase maps from individual camera frames, they are well-suited for dynamic 3D imaging; however, the methods have difficulty handling phase ambiguities. Phase ambiguities are dependent on many factors including low contrast fringe modulation, glare, shadows, stray light, noise, and surface discontinuities that cause phase shifts of more than 2π [24]. There have been attempts to mitigate the effects of phase ambiguities. Double-frame is one such method that uses a two-step phase shift approach [24–33]. Another method is to use aperiodic sinusoidal fringe patterns with cross-correlation between the measured intensity images [7,34]. The use of aperiodic fringe patterns solves the problem of 2π phase ambiguity for stereo based measurement systems but requires many images of unique fringe patterns.

Here, we report on a dynamic 3D FPP method that provides up to 8 unique fringe patterns during a single exposure. Our system employs a single light source equipped with a 4-band multispectral filter array (MFA) manufactured on a glass substrate. The MFA was comprised of four bandpass filters in a repeating mosaic arrangement with each filter $11\ \mu\text{m} \times 11\ \mu\text{m}$ in size. With the MFA in the illumination path, a multispectral structured light pattern was generated on the object. We then utilized a multispectral camera to differentiate the light patterns at each band. After multispectral image processing, unique fringe patterns oriented every 45° with two complementary fringe patterns π -phase shifted with respect to each other at each orientation were recovered. The method provided the necessary object data to take advantage of robust reconstruction algorithms that implement π -phase shifted fringe patterns, but with the advantage of acquiring the data in a single camera exposure with a single light source from a single projection coordinate. Below, we introduce the multispectral fringe pattern profilometry (MFPP) method and provide the first performance tests.

3.3 Method

A setup of the apparatus is shown in Figure 3-1 (a). Light from a halogen lamp was focused onto a MFA (Spectral Devices Inc., London, Canada). The MFA was comprised of a 2×2 arrangement of square bandpass filters that was repeated in a 2D Bayer-like pattern [35,36]. The filters had peak optical transmission at 580 nm (F1), 660 nm (F2), 735 nm (F3), and 820 nm (F4) (Figure 3-1(b)). An image of the MFA was focused onto the target using a 20x microscope objective resulting in a multispectral dot pattern that completely covered the target. An image of the pattern on the target was acquired with a snapshot multispectral camera with identical spectral response characteristics to the MFA (MSC-AGRI-1-A, Spectral Devices Inc., London, Canada [37]). With this setup, combinations of spectral dot patterns generated 6 distinct multispectral fringe patterns (MFP) directed in the vertical, horizontal, and diagonal directions (Figure 3-1 (c) and (d)). From these 6 MFPs, eight monochrome fringe patterns were extracted using a fringe extraction algorithm based on the Fourier transform [11]. The algorithm was capable of reliably extracting vertical, horizontal, and diagonal monochromatic fringe patterns from the vertical, horizontal, and diagonal MFPs, respectively.

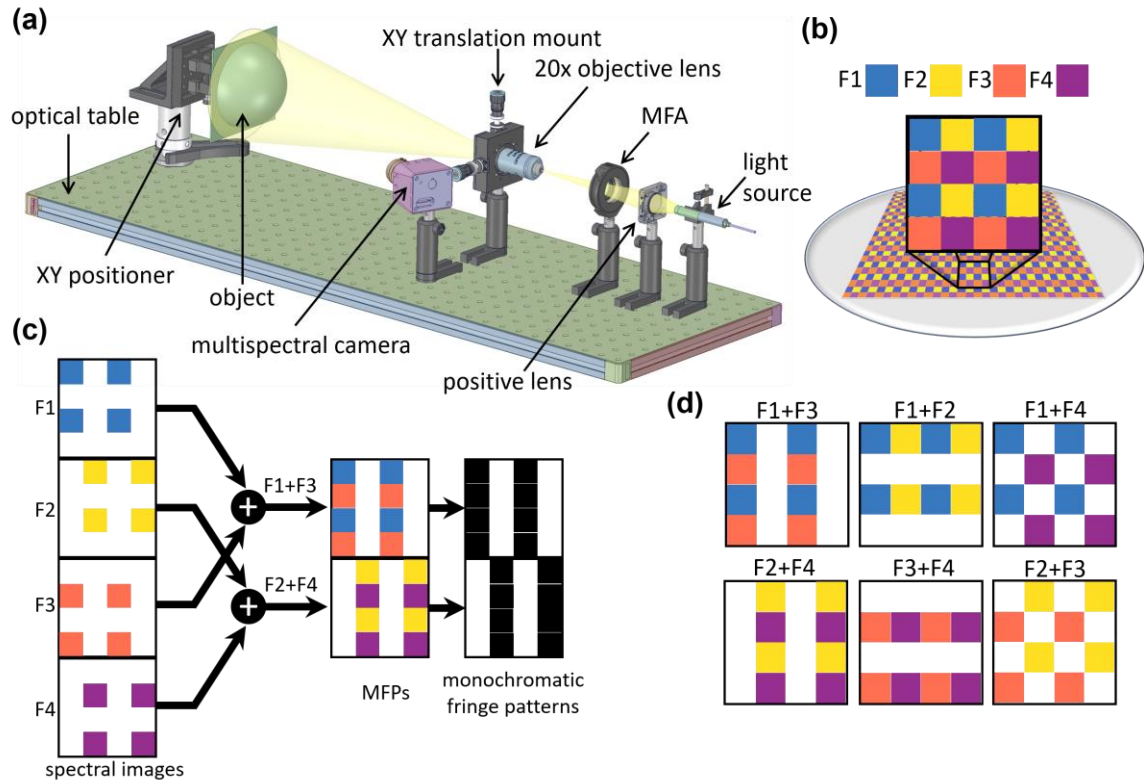


Figure 3-1: a) Schematic illustration of the setup consisting of a halogen light source, MFA, focusing lens, object, and snapshot multispectral camera. b) MFA consisted of a 2D array of four distinct filters at different wavelengths: 580 nm, 660 nm, 735 nm, and 820 nm indicated by blue (F1), orange (F2), yellow (F3), and purple (F4), respectively. c) Schematic of 2 vertical MFPs generated by combining pairs of spectral images of the object to form 2 unique monochromatic fringe patterns. For clarity, a single 4×4 pixel area is shown for each filter type, but the concept extends across all pixel data in each spectral image. d) Schematic of all 6 MFPs, distinguishable as 8 unique monochromatic fringe patterns.

3.3.1 Fringe decomposition

The combination of a pair of spectral dot patterns will generate an MFP in vertical, horizontal, 45° , and 135° , relative to the x-axis. Thus, the four spectral patterns provide six combinations. To extract continuous fringes out of these disjointed MFPs, we applied a fringe extraction method based on Fourier transform [11]. It should be noted that the fringe extraction method does not contribute to the FP phase-demodulation procedure and

is only used to illustrate the mathematics of the proposed method. The 2D Fourier transform of an image provides the frequency spectrum containing all spatial frequency components of the image. For an ideal 2D sinusoid fringe pattern, the frequency spectrum expresses three fundamental components for +1, -1, and 0 order terms, which indicate the spatial frequency of the intensity variations, its conjugate, and the low variation in background intensity, respectively. For a non-ideal sinusoidal fringe pattern, the Fourier spectrum shows additional terms indicating other frequency orders, e.g., harmonics, and artifacts. Applying inverse Fourier transform over the selected ± 1 and 0 order terms gives an ideal sinusoidal fringe pattern. **Error! Reference source not found.** illustrates the sinusoidal fringe pattern decomposition method. Each direction associates with distinct frequency terms in the Fourier spectrum. For example, the combination of F1 and F3 yields a vertical MFP relative to the x-axis (see Figure 3-1(c)), which results in two fundamental spatial frequency components that are symmetrical about the y-axis. The dot-shape of the MFPs causes some spurious frequency components in the Fourier domain. Therefore, relevant terms that need to be selected are $(f_x, 0)$, $(-f_x, 0)$, and $(0, 0)$, where f_x is the spatial frequency of the MFP in x-direction also called carrier frequencies in x (Figure 3-2(a)). Figure 3-2(b) demonstrates the filtering for horizontal fringes with the relevant frequency terms of $(0, f_y)$, $(0, -f_y)$, and $(0, 0)$ where f_y is the spatial frequency (or carrier frequencies) in the y-direction. The diagonal MFPs provide five fundamental components at (f_x, f_y) , $(f_x, -f_y)$, $(-f_x, f_y)$, $(-f_x, -f_y)$, and $(0, 0)$. In this case, it is possible to select two different sets of frequencies to extract the fringes directed in 45-degree and 135-degree (Figure 3-2(c)). By doing so, all six combinations generate eight monochrome sinusoidal fringes.

The mathematical representation of a captured image of a sinusoidal fringe pattern projected on an object can be described as:

$$I(x, y) = a(x, y) + b(x, y) \cos \left[2\pi (f_x x + f_y y) + \varphi(x, y) \right] \quad (3-1)$$

where I , a , and b denote the fringe pattern, background, and amplitude modulation, respectively, and (x, y) is the pixel coordinates. The argument of the cos function contains two parts. The first term represents the initial phase of the fringes, shown as $2\pi(f_x x + f_y y)$. The second term is the phase distribution caused by the surface morphology, shown as φ .

Equation (1) represents the eight fringe patterns discussed earlier. Since all fringe patterns are derived from the same system with the same light source and at the same time, the background variation can be considered identical for all patterns. However, the individual patterns may have different modulation depths due to the variation in response of the camera at each band. The major differences between these eight fringe patterns is the carrier frequency and the phase. Also, for the complementary fringe patterns, the carrier frequencies are equal, but their phase have a difference of π radians.

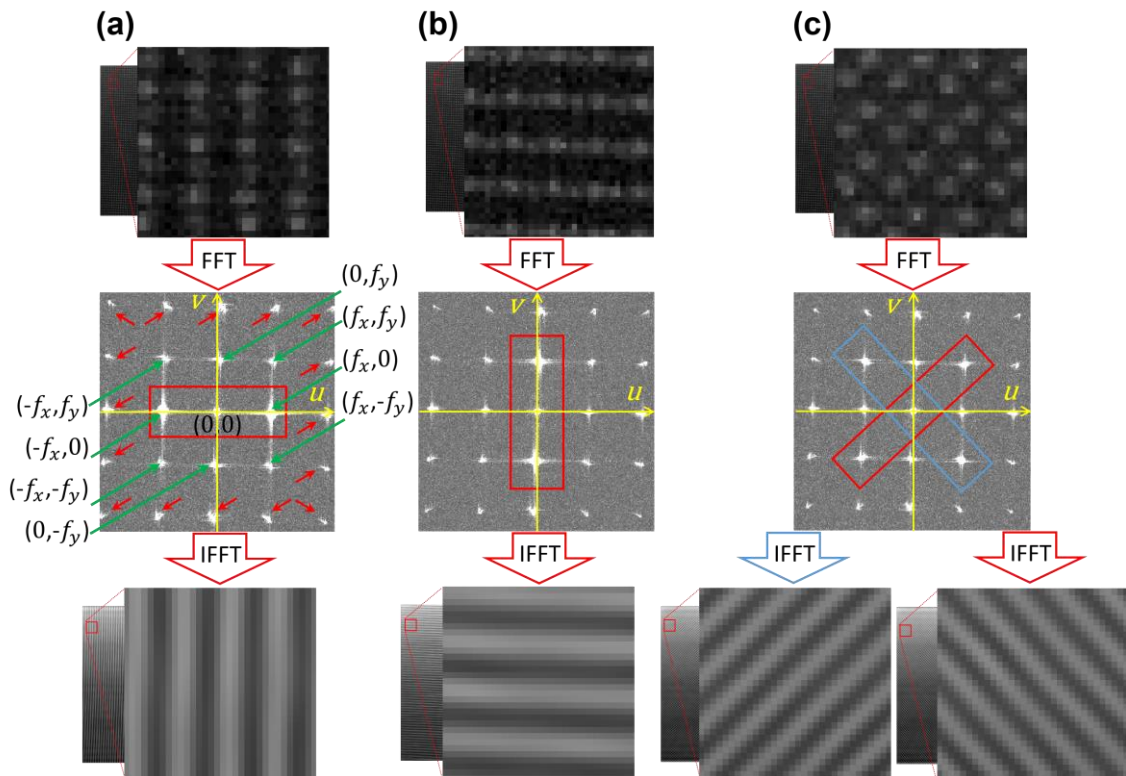


Figure 3-2: Fringe extraction method. a) From top to bottom: image of the combination of spectral images F1 and F3 showing a magnified view of a small

region indicated by the red box; 2D fast Fourier transform (FFT) of data in upper panel showing ± 1 order frequency components (green arrows), and harmonics (red arrows); 2D inverse fast Fourier transform (IFFT) of data in upper panel that has been masked to only include the $(f_x, 0)$, $(-f_x, 0)$, and $(0, 0)$ frequency components.

b) Extraction of horizontal fringes from the F1-F2 combination and c) extracting two diagonal fringes from the F2-F3 combination. A magnified view of a small region of the larger data set is indicated by the red box.

3.3.2 Background and noise-free fringe generation

For each direction, the pair of complementary fringe patterns were π -phase shifted with respect to each other. Subtraction of one fringe pattern from its complement resulted in a differential fringe pattern (DFP) that was corrected for DC offset and had enhanced contrast (Figure 3-4 **Error! Reference source not found.**). Removal of the DC offset is known to improve the phase-demodulation performance of the FT algorithm [38]. In the FT phase-demodulation algorithm, the fringe pattern was first converted to the frequency domain, which provided two fundamental components due to the periodicity of the sinusoidal fringes. One fundamental component was selected and transferred back to the spatial domain. The lack of a DC offset, thanks to this filter selection process, enabled a wider bandwidth that extended toward lower frequencies without introducing leakage of the DC component into the chosen fundamental component. The wider bandwidth filter resulted in enhanced resolution during phase-demodulation and enabled lower frequency fringes to contribute to the extracted phase data. Sensitivity to lower fringe frequencies also provided the opportunity to image more distant targets, since the divergence of the illumination pattern resulted in larger fringes as the illuminator to object distance increased. Figure 3-4 shows an example of 4 pairs of complementary fringe patterns obtained within a single camera exposure of a rigid flat plate as the object. The intensity line profiles clearly show the π -phase shift between the complementary fringe patterns. Processing of the complementary fringe patterns resulted in differential fringe patterns with lower background and higher contrast.

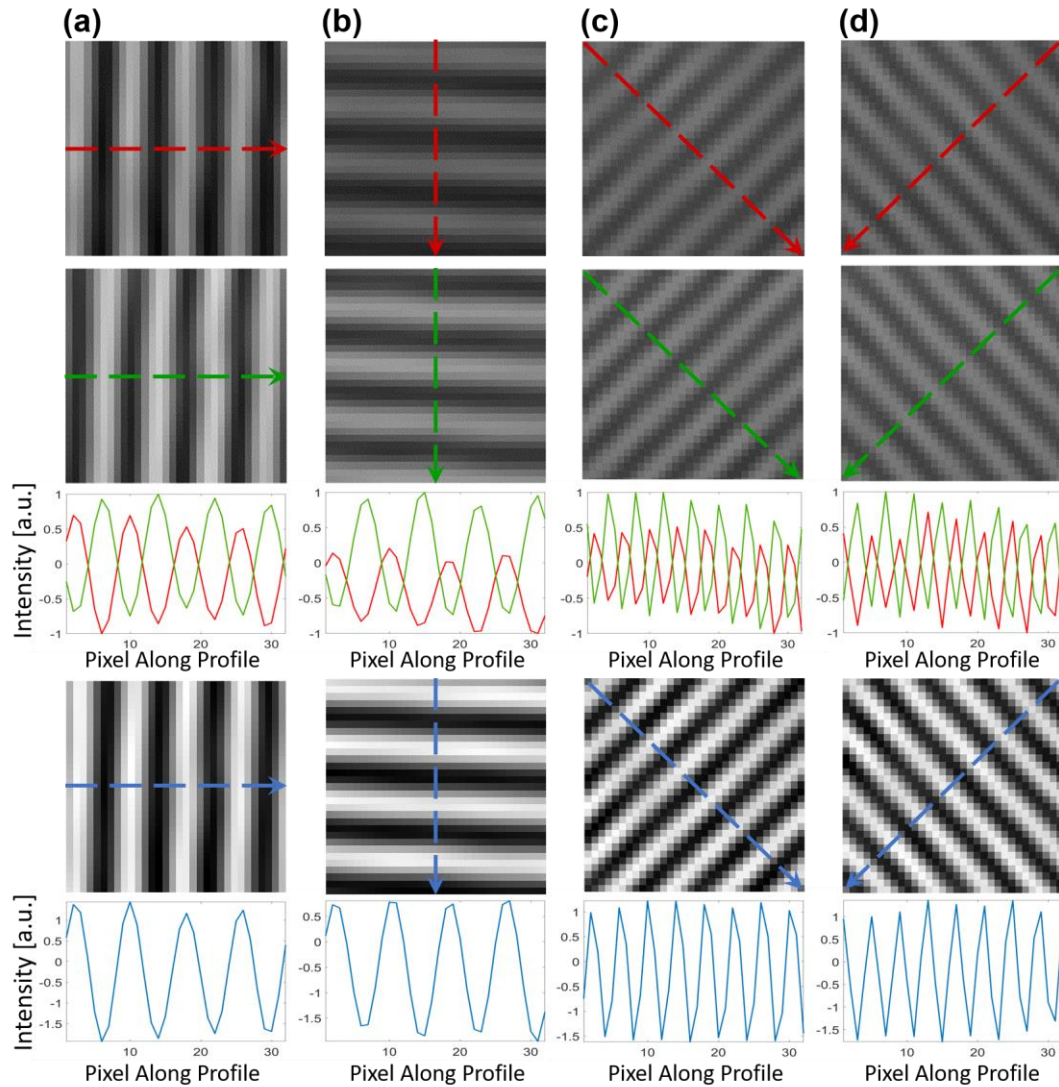


Figure 3-3: Subtraction of the complementary fringe patterns to produce a background-corrected and noise-reduced fringe pattern. a) Images of a vertical fringe pattern, b) horizontal fringe pattern, c) 45-degree fringe pattern, and d) 135-degree fringe pattern relative to the x-axis. From top to bottom: Images of the first complementary fringe pattern, second complementary π -phase shifted fringe pattern, color-coded intensity line profiles for the corresponding dashed lines indicated in the complementary fringe patterns, the DFP resulting from the subtraction of the first complementary fringe pattern from the second complementary fringe pattern, and the line profile for the corresponding dashed lines indicated in the DFP.

For each direction, the complementary fringe patterns can be considered as double frame two-step phase shifted fringe patterns with a phase step equal to π . In the current work, we utilize these two fringe patterns as independent patterns to generate the DFP. As an example, the vertical complementary fringe patterns produce a DFP as:

$$I_{DFP-Vertical} = I_{F1+F3} - I_{F2+F4} = (b_{13} + b_{24}) \times \cos(2\pi f_x x + \varphi) \quad (3-2)$$

where $I_{DFP-Vertical}$ is the DFP intensity map, I_{F1+F3} and I_{F2+F4} are the extracted complementary fringe patterns such that the indices show the combination of the multispectral frames. Figure 3-1 (c) shows schematically different combinations of the multispectral frames and Figure 3-4 demonstrates the complementary and the corresponding DFPs for all four directions.

3.3.3 Fourier transform phase demodulation

Fourier transform algorithm is a method of phase-demodulation, which is based on the spatial phase stepping information of the fringe pattern [42,43]. The algorithm follows three steps. Step 1: Apply FT on the pattern:

Rewriting Eq. (1), using Euler's rule provides:

$$I(x, y) = a(x, y) + c(x, y) e^{j(2\pi(f_x x + f_y y))} + c^*(x, y) e^{-j(2\pi(f_x x + f_y y))} \quad (3-3)$$

where $c(x, y) = (1/2)b(x, y)e^{j\varphi_o(x, y)}$ which encompasses the phase information and * denotes the complex conjugate. By taking the FT of this equation we obtain:

$$F\{I(x, y)\} = A(u, v) + C(u - f_x, v - f_y) + C^*(u + f_x, v + f_y) \quad (3-4)$$

where (u, v) represents the spatial frequencies, $F\{\cdot\}$ is 2D Fourier transform, and capital letters are the Fourier transformed of the corresponding small letters. The three components in Eq. (3-4) will be well separated in the Fourier domain when the carrier frequencies are higher than the maximum spatial frequencies of the object.

Step 2: Filter C or C^* to extract the object phase distribution, transfer the filtered component to the origin of the Fourier domain to eliminate the carrier frequency, and apply the inverse Fourier transform to get the analytical signal:

$$\text{iF}\{C(u, v)\} = c(x, y) = (1/2)b(x, y)e^{i\phi} \quad (3-5)$$

where $\text{iF}\{\cdot\}$ is 2D inverse FT function.

Step 3: Extract the mod 2π wrapped phase by finding the angle of the signal obtained from step 2 and unwrapping the phase to get the absolute phase map.

3.3.4 Phase-to-height conversion

The phase-to-height conversion is a systematic calibration procedure to extract the surface morphology based on the object phase distribution. Mapping the phase distribution to the surface height can be considered as linear or non-linear operations. Many parameters affect this mapping, including the distance between camera and projector, the orientation of the object/reference planes toward the camera sensor, camera and projector lens distortion, and the diverging nature of the projected fringes. Jia et al. (2007) compared linear and non-linear mapping procedures and concluded that the linear procedure would be more appropriate for objects with shallow depths [44]. On the other hand, nonlinear mapping has the same performance for objects with a small range of heights and is more accurate for objects with a greater range of heights. We have selected the nonlinear approach to convert the phase distribution to a height distribution. This requires measuring the phase distribution of a reference plane located at known distances from the camera. We have used the same procedure for phase estimation as described in Jia et al. (2007) with 20 steps in 2 mm distance increments.

3.3.5 Post-processing

In some cases, phase maps were multiplied with a binary mask to remove background artifacts. The masks were obtained by thresholding the sum of all four images captured in different spectral bands.

3.4 Results

System performance was examined through a series of experiments with complex test objects using FT phase-demodulation algorithm. In our system configuration, the vertical direction was perpendicular to the projector-camera baseline and was the most sensitive fringe pattern direction [39]. By implementing phase demodulation with only vertical fringe patterns, we evaluate the maximum performance of the system response with a set of complementary patterns. Figure 3-4 shows results from an experiment with the MFPP system using a head phantom. A photograph of the head phantom is shown in Figure 3-4 (a). Figure 3-4 (b) shows one complementary vertical fringe pattern obtained from the head phantom, the frequency spectrum computed from the fringe pattern, the resulting wrapped phase, and the resulting unwrapped phase from top to bottom, respectively. The results for the complementary π -phase shifted vertical fringe pattern are shown in Figure 3-4 (c) and presented in a similar order to Figure 3-4 (b). Similarly, the results for the DFP computed on the complementary vertical fringe patterns in Figure 3-4 (b) and Figure 3-4 (c) are shown in Figure 3-4 (d). From the frequency spectra, it was apparent that the background illumination, present as low-frequency components near the center of the 2D spectra, was diminished after subtraction of the complementary fringe pair. Furthermore, glare was greatly reduced. For example, the bright features above the eye and below the nose in the top row of Figure 3-4 (b) and Figure 3-4 (c) were not as evident in the DFP (Figure 3-4 (d) top row). The glare was unavoidable since a directional illuminator was used for fringe projection, which is prone to generating specular reflections. Since the two complementary patterns result in similar specular reflections, the resulting glare patterns detected by the multispectral camera were nearly identical, thereby enabling glare removal by simple subtraction. Figure 3-4 (e) shows the 3D visualization of the head phantom after applying a non-linear phase to height conversion to the unwrapped phase obtained from the subtracted pattern.

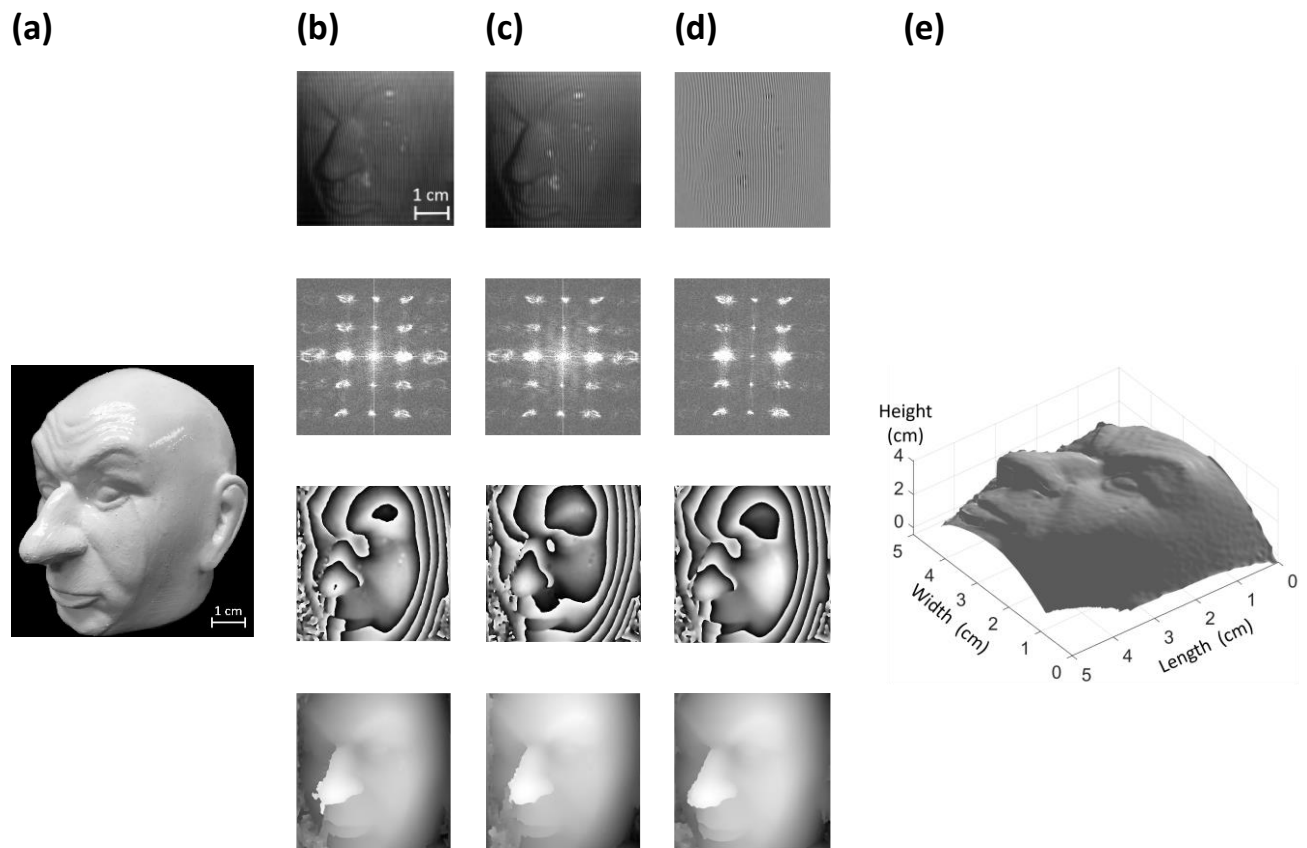


Figure 3-4: Phase demodulation for a head phantom. a) Photograph of the head phantom. b) Vertical fringe pattern acquired with MFPP method (top), the 2D frequency spectrum of the fringe pattern (second from top), wrapped phase computed from 2D frequency spectrum (second from bottom), and unwrapped phase (bottom) computed from the wrapped phase. c) Similar to (b), except results are for the vertical π -phase shifted fringe pattern complementary to (b). d) Similar to (b), except results are for the differential fringe pattern computed by subtracting the fringe pattern in (c) from the fringe pattern in b. e) 3D visualization of the object computed from the unwrapped phase in (d) after applying phase to height conversion.

Figure 3-5, Figure 3-6, and Figure 3-7 show the accuracy, lateral resolution, and axial resolution tests of the MFPP system that were acquired using a set of stationary targets. The targets were 3D printed with PLA and had a dimensional accuracy of 0.2 mm. Figure 3-5 contains a hemispherical target with a diameter of 100 mm (3D model shown in

Figure 3-5 (a)). The target represents a smooth object without any sudden changes to avoid Fourier phase demodulation algorithm intrusions in the results. Using MFPP, the wrapped and unwrapped phase estimates (Figure 3-5 (b) and Figure 3-5 (c), respectively) were obtained using a single 10 ms camera exposure. The overall shape of the hemisphere was reproduced accurately, except near the base which was susceptible to phase ambiguity due to shadowing. Also, the bandpass filter used in FT removed higher frequencies in the Fourier domain which led to a loss of sharpness at the edges. Moreover, the vertical fringe pattern under-sampled the left and right sides of the hemisphere and resulted in degradation of the phase maps in these areas; yet the largest error was $\sim 10\%$. A 3D visualization of the unwrapped phase map is shown in Figure 3-5 (d). Figure 3-5 (e) shows a color-coded error map where the measured height was compared with the expected height. Figure 3-5 (f) represents the statistical result of the error map. In this representation, the image was segmented into six different regions based on the orientation of the surface normal toward the optical axis of the illuminator and the camera. The results of the lateral resolution are shown in Figure 3-6. The target is shown in Figure 3-6 (a) and had five different groups of bars; each group consisted of six bars. Across the groups, the bar width varied from 1 to 5 mm in steps of 1 mm, the bar length was five times the bar width, and all bars had a height of 2 mm. Figure 3-6 (b) and (c) show the estimated wrapped and unwrapped phase, respectively. In Figure 3-6 (d) full width at half maximum (FWHM) of the measured widths of the bars for different groups are represented against the expected values. Figure 3-6 (e) shows a line profile that passed through the smallest group and corresponds to the red dashed line in Figure 3-6 (c). The system could accurately detect the phase changes for elements with a width of 2 mm or greater.

The target represented in Figure 3-7 (a) was designed to measure the axial resolution of the system and contained ten hemispheres of different radius from 1 to 10 mm. Similar to the results shown in Figure 3-5, shadowing and under-sampling was evident in the wrapped and unwrapped phase maps of the hemispheres (Figure 3-7 (b) and (c)). A plot of the measured height of the hemispheres vs the expected height is represented in Figure 3-7 (d). The line profile shown in Figure 3-7 (e) passes through the center of the seven smallest hemispheres. The smallest hemisphere in the target had a 1 mm height, which

was correctly estimated by the system. Since a 20x objective lens was used with a pupil-object distance of 60 cm, the dot size on the surface of the object was 1 mm and only two dots covered the smallest hemisphere.

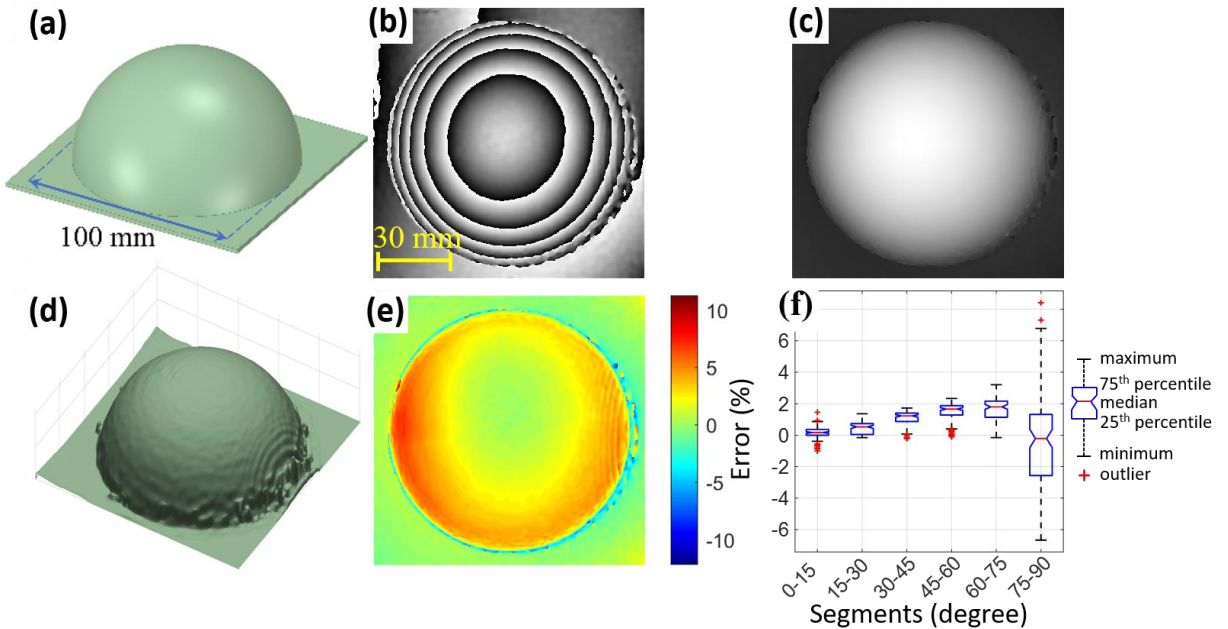


Figure 3-5: Accuracy test of MFPP. a) CAD model of the target consisting of a hemisphere with 100 mm diameter. b) and (c) Wrapped and unwrapped phase maps, respectively. d) 3D representation of the unwrapped phase after phase-to-height conversion. e) Color-coded error map between the measured height and the expected. f) Statistical error result against the orientation of the surface normal toward the MFPP optical axis.

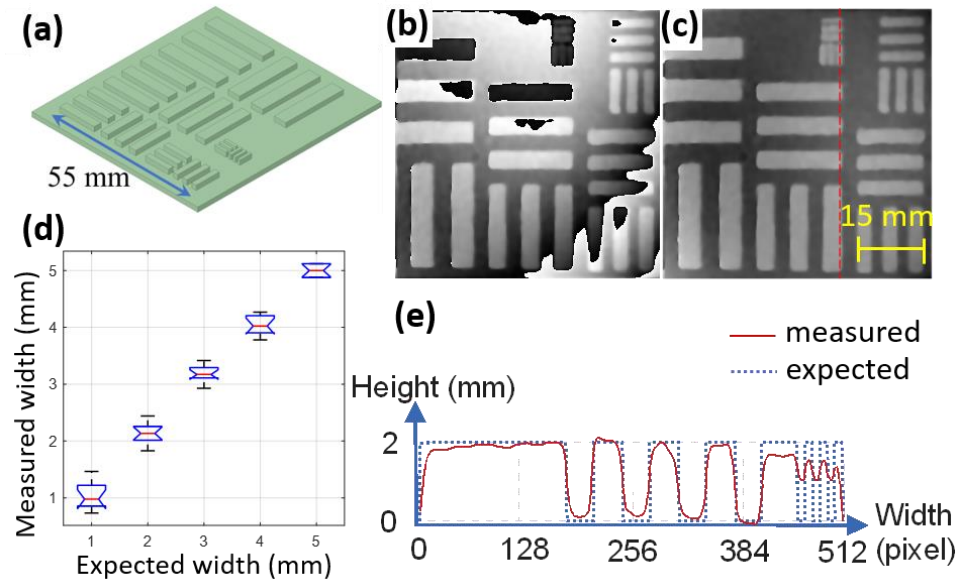


Figure 3-6: Lateral resolution test of MFPP. a) CAD model of the target consisting of five groups of bars of varying width (1 to 5 mm in steps of 1 mm). b) and (c) Wrapped and unwrapped phase maps, respectively. d) FWHM of the measured width against the expected width of the bars for different groups. e) Profile of the measured height corresponding to the red dashed line in panel (c).

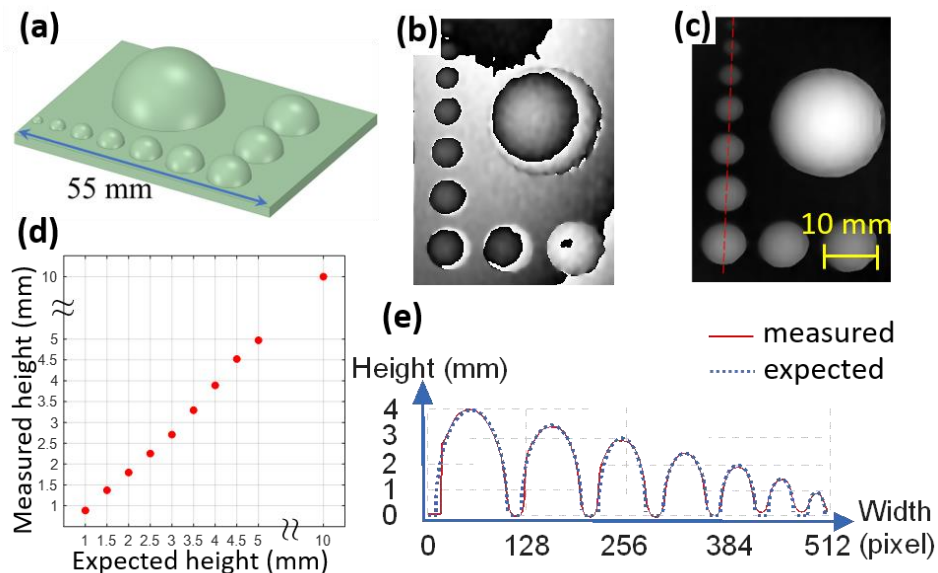


Figure 3-7: Axial resolution test. a) CAD model of the axial resolution target consisting of ten hemispheres of different radius (10, 5, 4.5, 4, 3.5, 3, 2.5, 2, 1.5, and 1 mm).

mm). b) and (c) Wrapped and unwrapped phase maps, respectively. d) Measured heights of the hemispheres against the expected values. e) Measured height corresponding to the red dashed line in (c).

We next tested the ability of MFPP to capture dynamic 3D surface maps by mounting an object on the platform of a rotation stage and spinning the stage platform at 10 RPM. The reflected MFPPs were captured from the object at 30 FPS during one 360° rotation giving rise to 180 frames for analysis.

Figure 3-8 shows an experiment with a rigid cylinder (radius = 35 mm) that was placed on the rotation stage approximately 20 mm off the axis of rotation (Figure 3-8 (a)). This setup was designed to estimate motion artifacts that might arise due to perspective errors. In principle, reconstruction of each snapshot should result in a cylinder, even though the location of the object in the field of view moves with each frame. Figure 3-8 (b), (c), and (d) show the wrapped phase map, unwrapped phase map, and 3D plot of the surface from the first acquired frame, respectively. The stack of line profiles acquired from each frame clearly shows the sinusoidal movement of the object, which is expected due to rotation at constant angular velocity. The left side of the line profiles is noisier likely due to shadowing resulting from the fact that the illuminator was located on the right side of the cylinder. Figure 3-8 (f) shows selected height profiles for the corresponding frames indicated in Figure 3-8 (e). As the cylinder rotates, the left side of the cylinder becomes more visible as the lateral position of the cylinder becomes more central to the optical axis of the camera.

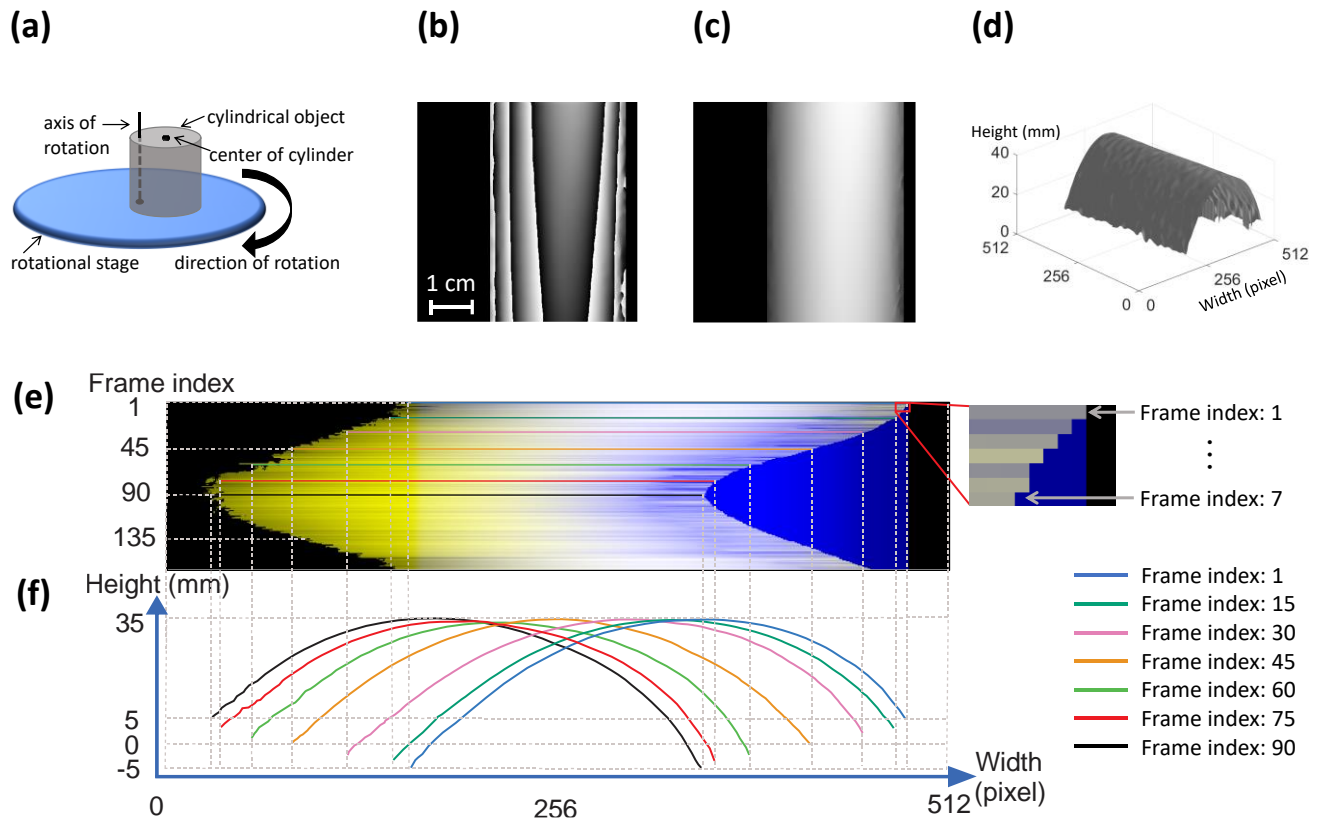


Figure 3-8: Analysis of motion artifacts by scanning a rotating object. a) Reflective cylindrical object with 35 mm radius mounted on a rotational stage. The center of the cylinder was located 20 mm from the center of the stage. b-d) Wrapped phase map, unwrapped phase map, and the 3D plot of the unwrapped phase map for frame index 1 (when the cylinder was located on the right side of the stage from the perspective of the camera). e) Color-coded line profiles for continuous frame indices from 1 to 160. The blue area shows the first frame index, and the yellow lines show the line profiles for all indexes. The magnified area (right panel in (e)) shows frames 1 to 7 when the cylinder moved from right to left as the stage rotated. f) Color-coded height profiles of the cylinder corresponding to the select frame indices indicated in (e).

The next experiment shows a quality measurement where the stage is spinning the head phantom about its center inferior-superior axis. Figure 3-9 (a) and (b) show the wrapped and unwrapped phase for five frames captured at different stages during the rotation.

Figure 3-9 (c) shows a 3D visualization of the unwrapped phase maps. The system could easily track the object and was unaffected by motion artifacts. However, the results show some artifacts caused by poor illumination in high slope areas (e.g., the edges of the head) and shadowing (e.g., the ear in the frame index 110). Nevertheless, these results clearly illustrate the snapshot capability of MFPP and demonstrate its ability to provide video rate 3D surface mapping.

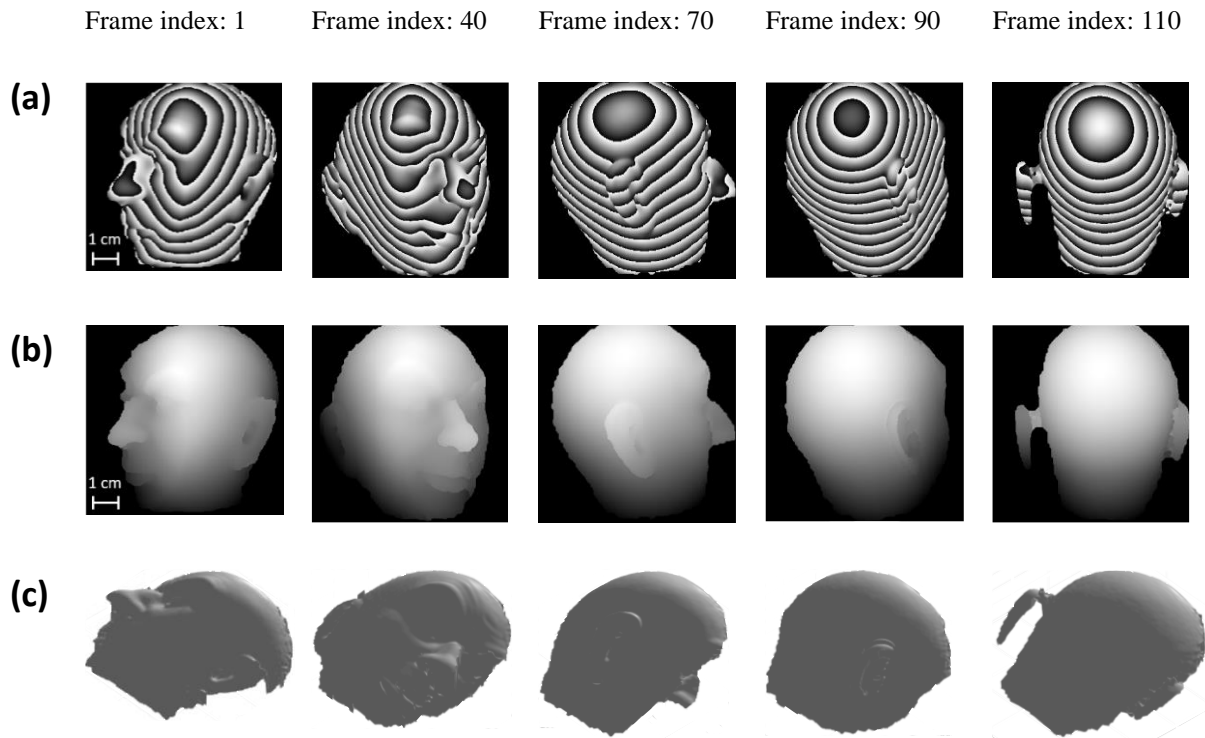


Figure 3-9: Dynamic 3D surface scanning of a rotating object. a) Wrapped and (b) unwrapped phase maps for five selected frames of a rotating head phantom at different stages of object's rotation. c) 3D visualization of the unwrapped phase maps.

In order to assess the sensitivity of the fringe patterns with regard to the directional morphological features, we have tested the system on a target that contains several edges in various directions. A CAD model of the target has been shown in Figure 3-10 (m) that contains twelve radially directed spokes with the height of 4mm regarding to the background plane. The unwrapped phase-maps of using the phase-demodulations for DFPs in vertical, horizontal, 45° , and 135° are presented in Figure 3-10 (e-h),

respectively. These results were then processed by the Sobel edge detection method to extract the sensed edge for each DFP (shown in Figure 3-10 (i-l)). It was found that each DFP was blind to the edges almost parallel to its direction. In this context, a summing of all sensed edges produced by individual DFPs could yield a nearly complete picture of all edges (Figure 3-10 (n)).

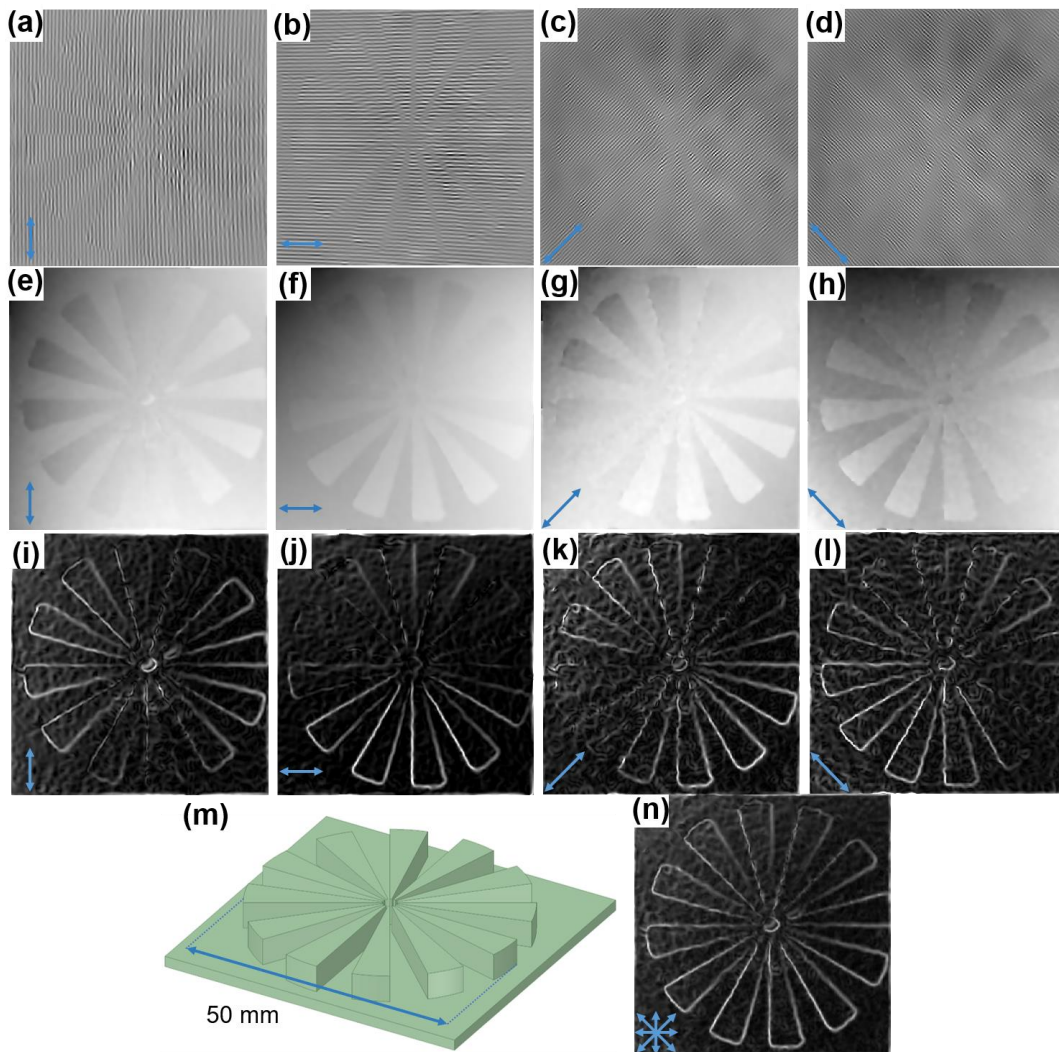


Figure 3-10: Evaluating the sensitivity of the fringe patterns in their different directions. a-d) DFPs in the vertical, horizontal, 45°, and 135° directions, respectively. e-h) Unwrapped phase maps for DFPs. i-l) Detected edge features with Sobel method for maps illustrated in (a-d), respectively. m) CAD model of the target consisting of twelve spokes spaced 30° apart. n) Combination of edge features

illustrated in (i-l). The arrows at the bottom left of the panels indicate in which direction the DFP was used in those panels.

3.5 Discussion

3.5.1 Major finding

This is the first report of a multispectral FPP method capable of snapshot operation for 3D measurement. In addition, this is the first study to demonstrate the use of a multispectral filter array and multispectral camera for fringe generation and measurement, respectively. Furthermore, the multispectral dot projection pattern provided a novel technique to extract up to 8 unique fringe patterns that resulted in full sampling from a single snapshot and a single projection point. The dot pattern resulted in 4 pairs of complementary π -shifted fringe patterns that were used to increase image resolution and mitigate object glare. Unlike color camera approaches, the higher spectral selectivity of the multispectral camera and MFA provided access to a greater number of unique color channels, had lower cross-talk between color channels, and offered flexibility in dot projection patterning through MFA customization. Also, unlike a color camera, the multispectral camera used near-infrared bands, which are invisible to human vision.

3.5.2 Speed

The main advantage of MFPP over other FPP methods was that with each camera exposure one 3D representation of the object was acquired. Therefore, the MFPP system was limited only by technical limits imposed by the camera, such as the maximum frame rate and the minimum exposure time. Our camera had a frame rate of 30 FPS, however, cameras with high frame rate would work as well, since there were no limitations imposed by our single point MFA projector. The camera frame rate controls the sampling frequency. Based on the Nyquist theorem, all object movements with a frequency up to half of the frame rate can be sampled without aliasing. The results in Figure 3-8 and Figure 3-9 were captured at 30 FPS and a Nyquist frequency of 15 FPS. The camera was

capable of up to 94 FPS with a Nyquist frequency of 47 FPS. Much higher frame rates (up to several thousand FPS) were possible for small regions of interest. For these experiments, an exposure time of 10 ms was used to capture each frame, thereby freezing objects with motion within very short timescales. These could be objects that were moving at high speed through the field of view. The maximum detectable speed was inversely dependent on the camera exposure time and was directly dependent on the projector magnification. However, 3D profilometry of objects with motion at even faster timescales is possible since our camera had a minimum exposure time of 100 μ s. The main limitation was the availability of light from the MFA illuminator to provide sufficient camera exposure at these fast time scales. Flashed xenon and LED MFA light sources could be used to achieve these fast timescales with our camera setup. Compared to the methods that use digital projectors [3–6], which have limited speed and spectral properties as well as more complex instrumentation, our method encoded and detected multiple fringe patterns simultaneously.

3.5.3 Accuracy

Accuracy was assessed by the MSE between the measured height and the expected height for a hemisphere target (Figure 3-5). We found the accuracy to be very high ($< 1\%$) for areas on the object that were facing the MFPP system with poorer accuracy for surfaces that were oblique to the MFPP system. Even still, the accuracy was within $\pm 10\%$ for even the most oblique surface features. This was evident from the error map shown in Figure 3-5 (e), but also quantitatively in the summary plot shown in Figure 3-5 (f). The plot reveals that for surfaces within 75° of normal the errors were $< 3\%$. However, for surfaces beyond 75° from normal, the error increased substantially. These results suggest MFPP is very robust for highly sloping surfaces. Furthermore, the use of the horizontal and angled fringe patterns available with the MFPP technique could lead to even higher accuracy. For example, in Figure 3-5 (e), the errors at the top and bottom of the hemisphere appear to be lower compared to the errors on the left and right side of the hemisphere. Since only the vertical fringe patterns were used to estimate these errors, we conclude that horizontal fringe patterns could lead to higher accuracies for the left and right sides of the hemisphere and the angled fringes to higher accuracy for areas in

between. Another source of error is that the Fourier phase modulation algorithm works on a global level. This could cause an error to spread throughout the entire phase map because of local issues like an abrupt change of the fringes due to the abrupt discontinuities in the surface (see Figure 3-6). In addition, due to the snapshot capability of MFPP, additional cameras and illuminators could be positioned around the object to capture the oblique surface features more accurately without any loss in overall acquisition speed.

3.5.4 Resolution

The lateral resolution of the MFPP system was estimated using a USAF resolution target consist of several bars, where the spacing between bars covered the expected resolution. This classical approach to resolution measurement allowed us to use FWHM and line profiles to estimate resolution directly. From these measurements, we estimated the lateral resolution be approximately 1 mm. This estimate was expected since the projected fringe period was 2 mm and lateral resolution is known to relate to half of the fringe period [40]. Axial resolution was estimated using a series of hemispherical targets of decreasing diameter. Although this resolution target is not standardized in the literature, it has the advantage of presenting a wide variety of oblique surfaces to the MFPP system for a range of target sizes. From our measurements, we estimated the axial resolution to be approximately 1 mm. As described for the lateral resolution, this estimate was expected due to the 2 mm fringe period. According to the MFPP system, half of the fringe period was equal to the dot size and the dot size was dependent on the magnification lens used in the illuminator and the lens pupil-object distance. Based on Figure 3-6 (e), only 10 pixels were enough to cover a single dot. Therefore, the system should be capable of reaching μm -scale resolutions by decreasing the illuminator magnification, decreasing the lens pupil-object distance (to produce smaller dots), and increasing the camera zoom (to allocate enough pixels to a dot). For large objects, the upper limit of measurements will be dependent on the phase-demodulation and phase unwrapping algorithms. For instance, for phase-demodulation algorithms that use a single wrapped phase map to calculate the absolute unwrapped phase map, such as the FT

method, any sudden changes in height that are larger than the fringe size will lead to phase ambiguity.

3.5.5 MFPP performance unaffected by object surface topography

In traditional FPP systems where a single fringe pattern in a specific direction is used, object topography affects the accuracy of the phase measurements. For example, when the fringe pattern is parallel to a feature with an edge, the feature may not be detected; however, a fringe perpendicular to the same edge will result in the detection of the feature. Furthermore, features with large slopes relative to the optical axis of the illuminator and the camera result in high-frequency fringe patterns that may be under-sampled by the camera [41]. In principle, MFPP can provide fringes in four different directions from a single snapshot, which greatly improves the chances that at least one fringe set will provide accurate local phase measurements (refer to Figure 3-10).

3.5.6 MFPP mitigated degrading effects of glare

Directional illumination of reflective surfaces tends to generate unavoidable glare in the acquired images. Glare can interfere with the fringe patterns, e.g. deformation of the original fringe shapes. Therefore, phase-demodulation algorithms, such as phase shifting and transform-based algorithms, can easily confuse glare as topographical features which increase errors. However, by having complementary fringe patterns, that have been captured at the same time and the same location, the glare is identical in both frames, but the fringe patterns are phase shifted. This ensures that glare will be diminished by subtracting the two patterns and the corresponding errors will be decreased. Figure 3-4 (b) and (c) show the effect of the glare in the retrieved phase maps while the DFP is free from those glare related errors.

3.5.7 *MFPP has greater robustness to under sampling*

The MFPP system uses a multispectral camera similar to work by Zhang et al (2018), but our system required only one projector with a single aperture [18]. The approach is simpler to implement since only one light source was required. Furthermore, projection of the multispectral pattern from a single point greatly simplified triangulation between

the projector, sensor, and object surface and resulted in robust phase-to-height conversion. Moreover, the methods that generate a grid pattern and extract orthogonal fringe patterns [3,4,11] are comparable to only one of the captured spectral bands whereas our method produces four. By having only one grid pattern, the gaps between two adjacent dots will be estimated by the FT filtering which can easily lead to incorrect fringe patterns and under-sampling. Alternatively, our method combines unique filter bands to generate complementary MFPs with higher dot density and thereby improving fringe quality.

3.5.8 Limitations of this study

Our implementation of MFPP used a single aperture projector and one multispectral camera separated by a well-defined angle. The setup inevitably produced shadows for some regions of objects due to the separation angle. The shadows resulted in phase ambiguities and poorer depth and height estimates in those regions. One potential avenue for improvement is to use multiple complementary projector/camera pairs so that shadows cast by the object for one projector receive illumination from a second projector. Using unique combinations of multispectral fringe patterns for each projector/camera pair would enable simultaneous operation without interference. Other limitations of the MFA projector are the fixed arrangement of the spectral dot pattern, balancing light output at each wavelength, and light throughput. The MFA has narrow spectral transmission characteristics at each band, which requires a high-power light source to sufficiently expose the camera. In our experiment, we used a 100 W QTH source to generate the desired pattern at a distance of 60 cm. Larger distances could be reached by replacing the QTH source with a high-power pulsed LED.

3.5.9 Implications for Future

With the development and rapid growth of applications for RGB-D cameras, that can capture both color and depth, MFPP could provide an alternative that can be implemented with simple components. Moreover, utilizing a simple projected light pattern instead of sequenced digital projections offers opportunities to significantly decrease the size of the setup. The MFPP system is suitable for miniaturization, which could enable its use in

space-constrained applications such as robotic surgery and mobile device applications such as color 3D video capture.

3.6 Software

Computations and figure creation (Figure 3-2, Figure 3-3, Figure 3-4, Figure 3-5, Figure 3-6, Figure 3-7, Figure 3-8, Figure 3-9, and Figure 3-10) were performed in MATLAB (Version: 2020b; <https://www.mathworks.com>; MathWorks, Natick, MA, USA). Some 3D renderings (**Error! Reference source not found.** (a), **Error! Reference source not found.** (c), and Figure 3-8 (a)) were created in Microsoft Power Point (Version: 365; <https://www.microsoft.com>; Microsoft Corporation, Redmond, WA, USA). One 3D rendering (**Error! Reference source not found.**(a)) was created in Ansys SpaceClaim (Version: 19.1; <https://www.ansys.com>; Canonsburg, PA, USA).

3.7 Acknowledgements

This work was supported by grants from the Natural Sciences and Engineering Research Council of Canada and the Canadian Institutes of Health Research to JJLC. The authors thank Spectral Devices Inc for providing the multispectral filter array and snapshot multispectral camera for this work.

3.8 Conflict of interest

Jeffrey Carson and Mohamadreza Najiminaini are co-founders, directors, and shareholders in Spectral Devices Inc., which supplied the multispectral filter array and the multispectral camera for this work. Parsa Omid and Mamadou Diop have no competing interests.

3.9 References

1. R. P. Gorthi SS, "Fringe projection techniques : Whither we are?," *Opt. Lasers Eng.* 48, 133–140 (2010).

2. S. Heist, P. Dietrich, M. Landmann, P. Kühmstedt, G. Notni, and A. Tünnermann, "GOBO projection for 3D measurements at highest frame rates : a performance analysis," *Light Sci. Appl.* **7**, 1–13 (2018).
3. L. Huang, C. S. Ng, and A. K. Asundi, "Dynamic three-dimensional sensing for specular surface with monoscopic fringe reflectometry," *Opt. Express* **19**, 12809–12814 (2011).
4. J. L. Flores, B. Bravo-medina, and J. A. Ferrari, "One-frame two-dimensional deflectometry for phase retrieval by addition of orthogonal fringe patterns," *Appl. Opt.* **52**, 6537–6542 (2013).
5. S. Lei and S. Zhang, "Digital sinusoidal fringe pattern generation: Defocusing binary patterns VS focusing sinusoidal patterns," *Opt. Lasers Eng.* **48**, 561–569 (2010).
6. Y. Gong and S. Zhang, "Ultrafast 3-D shape measurement with an off-the-shelf DLP projector," *Opt. Express* **18**, 19743–19754 (2010).
7. N. G. Heist S, Mann A, Kühmstedt P, Schreiber P, "Array projection of aperiodic sinusoidal fringes for high-speed three-dimensional shape measurement," *Opt. Eng.* **53**, 112208 (2014).
8. S. Heist, P. Lutzke, I. Schmidt, P. Dietrich, P. Kühmstedt, A. Tünnermann, and G. Notni, "High-speed three-dimensional shape measurement using GOBO projection," *Opt. Lasers Eng.* **87**, 90–96 (2016).
9. H. Zhang, Q. Zhang, Y. Li, and Y. Liu, "High Speed 3D Shape Measurement with Temporal Fourier Transform Profilometry," *Appl. Sci.* **9**, 4123 (2019).
10. M. Takeda, Q. Gu, M. Kinoshita, H. Takai, and Y. Takahashi, "Frequency-multiplex Fourier-transform profilometry : a single-shot three-dimensional shape measurement of objects with large height discontinuities and for surface isolations," *Appl. Opt.* **36**, 5347–5354 (1997).

11. N. Alcalá, "One shot profilometry using a composite fringe pattern," *Opt. Lasers Eng.* 53, 25–30 (2014).
12. O. L. H. Tong, A. Chamson-Reig, L. C. M. Yip, M. Brackstone, M. Diop, and J. J. L. Carson, "Structured-light surface scanning system to evaluate breast morphology in standing and supine positions," *Sci. Rep.* 10, 1–12 (2020).
13. W. Su, "Color-encoded fringe projection for 3D shape measurements," *Opt. Express* 15, 13167–13181 (2007).
14. C. H. G. Uo, X. I. L. In, A. H. U. Nduo, and J. U. N. Z. Ou, "Improved phase-measuring deflectometry for aspheric surfaces test," *Appl. Opt.* 55, 2059–2064 (2016).
15. M. T. Nguyen, Y. Ghim, and H. Rhee, "Single-shot deflectometry for dynamic 3D surface profile measurement by modified spatial- carrier frequency phase-shifting method," *Sci. Rep.* 9, 1–15 (2019).
16. Y. You, Y. Shen, G. Zhang, and X. Xing, "Real-Time and High-Resolution 3D Face Measurement via a Smart Active Optical Sensor," *Sensors* 17, 734 (2017).
17. T. Wakayama, "High-speed three-dimensional shape measurements using multiwavelength spatiotemporal phase shifting," *Opt. Eng.* 53, 112207 (2014).
18. C. Zhang, A. Breitbarth, C. Zhang, A. Brahm, A. Breitbarth, M. Rosenberger, and G. Notni, "Single-frame three-dimensional imaging using spectral-coded patterns and multispectral snapshot cameras," *Opt. Eng.* 57, 123105 (2018).
19. C. Zuo, S. Feng, L. Huang, T. Tao, W. Yin, and Q. Chen, "Phase shifting algorithms for fringe projection profilometry: A review," *Opt. Lasers Eng.* 109, 23–59 (2018).
20. X. Su and W. Chen, "Fourier transform profilometry : a review," *Opt. Lasers Eng.* 35, 263–284 (2001).

21. Q. Kemao, "Windowed Fourier transform for fringe pattern analysis," *Appl. Opt.* 43, 2695–2702 (2004).
22. J. Zhong and J. Weng, "Spatial carrier-fringe pattern analysis by means of wavelet transform: Wavelet transform profilometry," *Appl. Opt.* 43, 4993–4998 (2004).
23. M. Trusiak, K. Patorski, and K. Pokorski, "Hilbert-Huang processing for single-exposure two-dimensional grating interferometry," *Opt. Express* 21, 28359–28379 (2013).
24. Y. Xu, S. Jia, Q. Bao, H. Chen, and J. Yang, "Recovery of absolute height from wrapped phase maps for fringe projection profilometry," *Opt. Express* 22, 3188–3196 (2014).
25. J. Vargas, J. A. Quiroga, C. O. S. Sorzano, J. C. Estrada, and J. M. Carazo, "Two-step demodulation based on the Gram – Schmidt orthonormalization method," *Opt. Lett.* 37, 443–445 (2012).
26. M. Trusiak and K. Patorski, "Two-shot fringe pattern phase-amplitude demodulation using Gram-Schmidt orthonormalization with Hilbert-Huang pre-filtering," *Opt. Express* 23, 3640–3651 (2015).
27. J. Vargas, J. A. Quiroga, T. Belenguier, M. Servín, and J. C. Estrada, "Two-step self-tuning phase-shifting interferometry," *Opt. Express* 19, 638–648 (2011).
28. T. Chao and S. Liu, "Phase retrieval in two-shot phase-shifting interferometry based on phase shift estimation in a local mask," *Opt. Express* 25, 24368–24378 (2017).
29. F. Yang and X. He, "Two-step phase-shifting fringe projection profilometry: intensity derivative approach," *Appl. Opt.* 46, 7172–8 (2007).
30. T.-W. Hui and G. K.-H. Pang, "3D measurement of solder paste using two-step phase shift profilometry," *IEEE Trans. Electron. Packag. Manuf.* 31, 306–315 (2008).

31. D. Zheng and F. Da, "Gamma correction for two step phase shifting fringe projection profilometry," *Opt. - Int. J. Light Electron Opt.* 124, 1392–1397 (2013).
32. G. G. Padilla M, Servin M, "Profilometry with digital fringe - projection at the spatial and temporal Nyquist frequencies," *Opt. Express* 25, 22292–302 (2017).
33. Z. Zhong, H. Bai, M. Shan, Y. Zhang, and L. Guo, "Fast phase retrieval in slightly off-axis digital holography," *Opt. Lasers Eng.* 97, 9–18 (2017).
34. G. Heist, S., Kuehmstedt, P., Tuennermann, A. and Notni, "Theoretical considerations on aperiodic sinusoidal fringes in comparison to phase-shifted sinusoidal fringes for shape measurement," *Appl. Opt.* 54, 10541–10551 (2015).
35. M. Najiminaini, F. Vasefi, B. Kaminska, and J. J. L. Carson, "Nanohole-array-based device for 2D snapshot multispectral imaging," *Sci. Rep.* 3, 1–7 (2013).
36. M. Najiminaini, B. Kaminska, K. St. Lawrence, and J. J. L. Carson, "Bolus tracking with nanofilter-based multispectral videography for capturing microvasculature hemodynamics," *Sci. Rep.* 4, 1–9 (2014).
37. "Multispectral snapshot cameras,"
<https://www.spectraldevices.com/products/multispectral-snapshot-cameras>.
38. M. Servin, J. A. Quiroga, and J. M. Padilla, *Fringe Pattern Analysis for Optical Metrology, Theory, Algorithms, and Applications* (Wiley-VCH, 2014).
39. P. Zhou, X. Liu, and T. Zhu, "Analysis of the relationship between fringe angle and three-dimensional profilometry system sensitivity," *Appl. Opt.* 53, 2929–2935 (2014).
40. K. J. Gasvik, *Optical Metrology*, 3rd ed. (John Wiley & Sons, 2002).
41. V. M. Abzal A, Saadatseresht M, "Development of a new dual-pattern fringe projection scanner," *Photogramm. Rec.* 34, 63–84 (2019).
42. P. Omid, L. C. M. Yip, H. Wang, and M. Diop, "SoftwareX PhaseWare : Phase

map retrieval for fringe projection profilometry and off-axis digital holographic interferometry," *SoftwareX* 13, 100652 (2021).

43. P. Omid, H. Wang, M. Diop, and J. J. L. Carson, "Algorithm for phase-displacement conversion from reflection digital holographic interferometry," 25 (2019).
44. P. Jia, "Comparison of linear and nonlinear calibration methods for phase-measuring profilometry," *Opt. Eng.* 46, 043601 (2007).

Chapter 4

4 Single-shot 4-step phase-shifting multispectral fringe projection profilometry

Publication status: The chapter has been submitted as a paper to the journal of Optics Express.

4.1 Abstract:

Phase-shifting profilometry (PSP) is considered to be the most accurate technique for phase retrieval with fringe projection profilometry (FPP) systems. However, PSP requires that multiple phase-shifted fringe patterns be acquired, usually sequentially, which has limited PSP to static or quasi-static imaging. In this paper, we introduce multispectral 4-step phase-shifting FPP that provides 3D imaging using a single acquisition. The method enables real-time profilometry applications. A single frame provides all four phase-shifted fringe patterns needed for the PSP phase retrieval algorithm. The multispectral nature of the system ensures that light does not leak between the spectral bands, which is a common problem in simultaneous phase-shifting with color cameras. With the use of this new concept, custom composite patterns containing multiple patterns can be acquired with a single acquisition

4.2 Introduction

Fringe projection profilometry (FPP), also known as phase measuring profilometry (PMP), is a three-dimensional (3D) shape measurement method based on structured light [1]. The shape measurement in FPP relies on phase estimates from two-dimensional (2D) fringe patterns (FPs) and triangulation analysis. The method has four steps: (1) illumination of the object with one or more FPs, (2) recording of the distorted FPs with a

camera, (3) computation of the phase changes within the FPs with respect to FPs at a reference plane, and (4) conversion of the computed phase changes into a topographical elevation map of the object's surface.

The phase map computation from the FPs can be performed with both spatial and temporal phase stepping methods. Spatial phase stepping algorithms evaluate fringe deformation at each pixel by considering the surrounding pixels. This class of algorithms is also referred to as transform-based algorithms since mathematical transform functions such as Fourier, Wavelet, and Hilbert are implemented [2]. Spatial phase stepping methods can retrieve the phase from a single copy of a deformed FP, which can be advantageous for measuring time-varying surfaces. However, any shadowing caused by poor illumination unavoidably leads to uncertainty and error [3]. Alternatively, temporal phase stepping methods consider the phase of the FP at each pixel as a function of time. Since a typical 2D FP model has three unknowns (background, modulation intensity, and phase), calculation of the phase values requires at least three phase-shifted FPs. Indeed, phase-shifting profilometry (PSP) is another name for this class of algorithms. The main advantage of temporal phase stepping is the capability of pixel-wise phase measurements; however, the need for multiple acquisitions limits its application to static and quasi-static scenes.

Use of a multiple FPs leads to better topographical estimates [4]. Given that projecting a sequence of FPs is time-consuming and suboptimal for applications that require fast measurements, single-shot 3D shape measurement using composite patterns (CP) has been developed [5]. Composite patterns contain multiple FPs, which are distinguishable by some means. The CPs can be categorized as either grayscale or color [6] and a variety of combinations have been designed and evaluated, such as those based on combination of different FPs with different orientations [7–9], different spatial frequencies [10–14], and different spatial phases [15–20]. While many of these techniques have been developed to improve the accuracy and sensitivity of measurements for spatial phase-stepping algorithms, others have been designed to enable PSP algorithms to be applied to data collected when projecting a single structured light pattern.

With a technique based on amplitude modulation, it is possible to compile any number of patterns into a grayscale composite pattern; however, increasing the number of patterns results in reduced dynamic range of individual patterns and errors in the demodulation process [15,16]. On the other hand, color patterns encode the fringes by taking advantage of color in addition to the intensity of the projected light. One way to take advantage of this idea is to use a sinusoidal intensity FP composed with a color-coded stripe pattern [21–23]. The functionality of the color stripes is to identify the fringe order while that of the sinusoidal intensity FP is to provide dense relative depths. However, these methods only provide a single FP supported with color strips to reduce the phase retrieval error. There are other utilizations of the color information that help provide multiple FPs in a single frame. One way is to mix separate FPs produced in different color channels, e.g., red, green, and, blue [24,25]. These methods are subject to non-linear error introduced by non-linear responses of the color projectors and color cameras. The errors have been discussed in the literature and compensating methods to reduce them have been proposed [26]. Nevertheless, the error cannot be eliminated entirely even with compensation. Additionally, these techniques are sensitive to surface colors and suffer from lower SNR due to spectral division [15]. These issues, along with the color-band leakage problem, limit the accuracy of phase maps obtained with color CPs [27].

In this paper, we describe a multispectral CP that encodes multiple FPs by decomposing the light source into several spectral bands. Every band provides a unique pattern and when combined, they form a CP. The light is decomposed using a multispectral filter array (MFA) made from an array of bandpass filters manufactured on a glass substrate. The patterning of the MFA determines the CP structure; therefore, the technique allows for a variety of CP designs. Here, we present a new category of CP that contains four phase-shifted fringe patterns, whose phase map can be retrieved using PSP processing algorithms.

The manuscript is organized as follows. Section 2 describes the projection method and the phase retrieval procedure. Results of the application of the novel multispectral CP technique are presented in Section 3 for illustration. Section 4 concludes the article with a discussion on the technique and results.

4.3 Methods

4.3.1 Setup

A custom designed multispectral filter array (MFA; Spectral Devices Inc., London, Canada) was used to generate a CP that encompassed four phase-shifted FPs. The MFA was manufactured on a glass substrate and contained a repeating pattern of four adjacent bandpass filters that were each $11\ \mu\text{m}$ wide and $11\ \text{mm}$ long. The pattern was repeated 256 times across the device, resulting in a square device $11\ \text{mm}$ by $11\ \text{mm}$ (Figure 4-1 (a)). The filters were designed to have peak optical transmission at $580\ \text{nm}$ (F1), $660\ \text{nm}$ (F2), $735\ \text{nm}$ (F3), and $820\ \text{nm}$ (F4). The MFA was positioned in the path of a broadband light source (Figure 4-1 (b)), which resulted in a multispectral CP on the surface of the target object (Figure 4-1 (c)). The multispectral CP was recorded with a snap-shot multispectral camera with similar spectral response characteristics (MSC-AGRI-1-A, Spectral Devices Inc., London, Canada [28]). Raw images recorded with the MSC-AGRI-1-A were demosaiced into 4 images, each representing a distinct spectral band. Each set of 4 multispectral images from a single camera exposure resulted in 4 FPs, where one FP due to one filter pattern was $\pi/2$ phase-shifted with respect to the FP from the adjacent filter pattern, resulting in a set of FPs that were suitable for PSP phase retrieval algorithms.

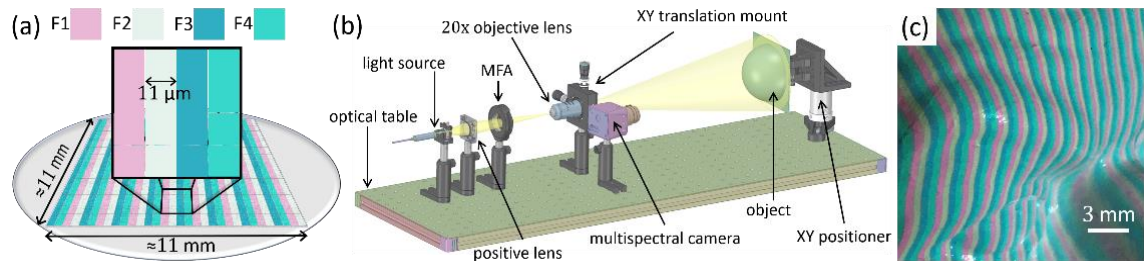


Figure 4-1: Multispectral pattern generation. a) Schematic of the MFA (not to scale). b) Rendering of the optical setup consisting of a halogen light source, MFA, lenses, the object, and snapshot multispectral camera. c) Color image (Apple iPhone-6s) of the CP projected onto the surface of a white plastic object.

4.3.2 Phase retrieval

Each FP represents a reflection of the light pattern (here, straight fringes) from the surface of the imaged object. The fringes are distorted due to the object's topography, and this can be mathematically modeled as [29]:

$$I(x, y) = A(x, y) + B(x, y) \cos[\phi(x, y)] \quad (4-1)$$

where, (x, y) denote the camera pixel coordinates, $A(x, y)$ and $B(x, y)$ are the background intensity and the modulation amplitude, respectively, which are associated with the object's surface reflectivity index, the ambient light, and the effects of the optics. The phase of the distorted FP is indicated as $\phi(x, y)$ which includes the original FP phase plus the phase modulation caused by the object's surface depth and height variations.

Traditional 4-step phase-shifting involves projecting 4 sinusoidal FPs in which the patterns are evenly phase-shifted, i.e., $\pi/2$. Correspondingly, the camera captures the distorted patterns as:

$$I_n(x, y) = A(x, y) + B(x, y) \cos[\phi(x, y) + (n-1)\pi/2] \quad (4-2)$$

where $n = 1, 2, 3, 4$ are the phase-shift indexes. For this notation, it has been assumed that the background intensity, modulation amplitude, and the object surface behavior is the same for all four acquired frames. Under such assumption, the phase can be calculated as [29]:

$$\phi = \arctan\left(\frac{\sin(\phi)}{\cos(\phi)}\right) = \arctan\left(\frac{I_4 - I_2}{I_1 - I_3}\right) \quad (4-3)$$

Hereinafter, the coordinate (x, y) has been eliminated to simplify the notations. The phase computed by this method produces a wrapped version of the phase map limited between $-\pi$ and π due to the properties of the arctan function. Therefore, there is a need for unwrapping to obtain the absolute value of the phase.

As mentioned earlier, the wrapped phase is computed under the assumptions that (1) the object is invariant and (2) all optical aspects of the illumination subsystem, image acquisition subsystem, and the target object behavior are unchanged during the four acquisitions. Since we acquire all 4 acquisitions simultaneously using multispectral illumination and multispectral imaging, the first assumption is met, i.e. the object is stationary for all 4 FP acquisitions. The second assumption is not fully met since with multispectral imaging there can be significant differences between spectral images of the FPs. This is because (1) the snapshot multispectral camera has different responses for different wavelengths and (2) the reflectivity of the object is not the same for each spectral band. In this case, we have:

$$I_n = A_n + B_n \cos[\phi + (n-1)\pi / 2] \quad (4-4)$$

Correspondingly, the arctan of the same ratio between the four phase-shifted patterns brings:

$$\begin{aligned} \arctan\left(\frac{I_4 - I_2}{I_1 - I_3}\right) &= \arctan\left(\frac{A_4 - A_2 + (B_4 + B_2)\sin(\phi)}{A_1 - A_3 + (B_1 + B_3)\cos(\phi)}\right) \\ &= \arctan\left(\frac{A_N + (B_N)\sin(\phi)}{A_D + (B_D)\cos(\phi)}\right) = \phi \end{aligned} \quad (4-5)$$

where $A_N = A_4 - A_2$, $B_N = B_4 + B_2$, $A_D = A_1 - A_3$, and $B_D = B_1 + B_3$. It can be seen that $\phi \neq \phi$, meaning any discrepancy in the background or modulation of the four bands will add errors to the retrieved phase map. On the other hand, by removing A_n s and equalizing B_n s, the error can be mitigated.

We propose a method based on the Lissajous figures and ellipse fitting (LEF) derived from research presented in [9] and [30] to decrease the aforementioned error. The Lissajous figure is a graph that plots two sinusoidal intensity profiles against each other in a 2D Cartesian coordinate system. When the profiles share the same frequency of repetition but have a non-zero phase offset, the graph is equivalent to an ellipse. By assuming that the profiles are parametrically represented as:

$$I_x = x_0 + \rho_x \cos \omega t \quad \text{and} \quad I_y = y_0 + \rho_y \cos(\omega t + \psi) \quad (4-6)$$

then based on the Pythagorean identity that $\cos^2 \omega t + \sin^2 \omega t = 1$, the ellipse can be derived as:

$$\frac{(I_x - x_0)^2}{\rho_x^2} + \frac{(I_y - y_0)^2}{\rho_y^2} - \frac{2 \cos \psi (I_x - x_0)(I_y - y_0)}{\rho_x \rho_y} = \sin^2 \psi \quad (4-7)$$

Therefore, by considering that the captured FPs are sequentially $\pi/2$ phase-shifted representations of the same sinusoidal pattern, it can be concluded that plotting of the Lissajous figure for every adjacent pair will produce an ellipse. To normalize, we take the four adjacent pairs (Figure 4-2 (a)) to plot the Lissajous figure four times. For each pair, two identical and synchronized sliding windows with center (x, y) and size (w, h) were used to select two corresponding parts of the two FPs (Figure 4-2 (b)). The size of the window pair was designed to ensure that it covered at least one fringe period and at least five pixels of the local FP. These conditions enabled the fitting of an ellipse to the intensity samples that enclosed at least one cycle of the local fringe pattern [30]. The intensities of the selected pixels were then plotted against each other (e.g., the Lissajous plot of the selected window pair for I_2 against I_1 is shown in Figure 4-2(c)). An ellipse was fitted to the points of the Lissajous plot (Figure 4-2 (d)) using the least square method by modeling the conical form of the ellipse as shown in Eq. (4-8).

$$c_1 I_x^2 + 2c_2 I_x I_y + c_3 I_y^2 + 2c_4 I_x + 2c_5 I_y + c_6 = 0 \quad (4-8)$$

The background, amplitude, and phase shift parameters of the two profiles were then computed as [31]:

$$\left\{ \begin{array}{l} x_0 = \frac{c_2 c_5 - c_3 c_4}{\delta} \quad \& \quad \rho_x = \frac{\sqrt{-c_3 \Delta}}{\delta} \\ y_0 = \frac{c_2 c_4 - c_1 c_5}{\delta} \quad \& \quad \rho_y = \frac{\sqrt{-c_1 \Delta}}{\delta} \\ \psi = \arccos\left(\frac{-c_2}{\sqrt{c_1 c_3}}\right) \end{array} \right. \quad \text{where} \quad \left\{ \begin{array}{l} \delta = \begin{vmatrix} c_1 & c_2 \\ c_2 & c_3 \end{vmatrix} \\ \Delta = \det \left(\begin{bmatrix} c_1 & c_2 & c_4 \\ c_2 & c_3 & c_5 \\ c_4 & c_5 & c_6 \end{bmatrix} \right) \end{array} \right. \quad (4-9)$$

The two normalized quadratic profiles were defined as $I'_x = (I_x - x_0) / \rho_x$ and $I'_y = (I_y - y_0) / \rho_y$ in which the Lissajous figure produces a unit circle with the center located at $(x'_0, y'_0) = (0, 0)$ as shown in Figure 4-2 (e). The process was repeated for all pixels to generate pixel-wise normalization for each FP pair resulting in two normalized frames for each I_n ($n = 1, 2, 3, 4$). A pixel-wise averaging was performed on each pair of normalized frames and resulted in the final normalized FP (Figure 4-2 (k-n)) suitable for phase extraction.

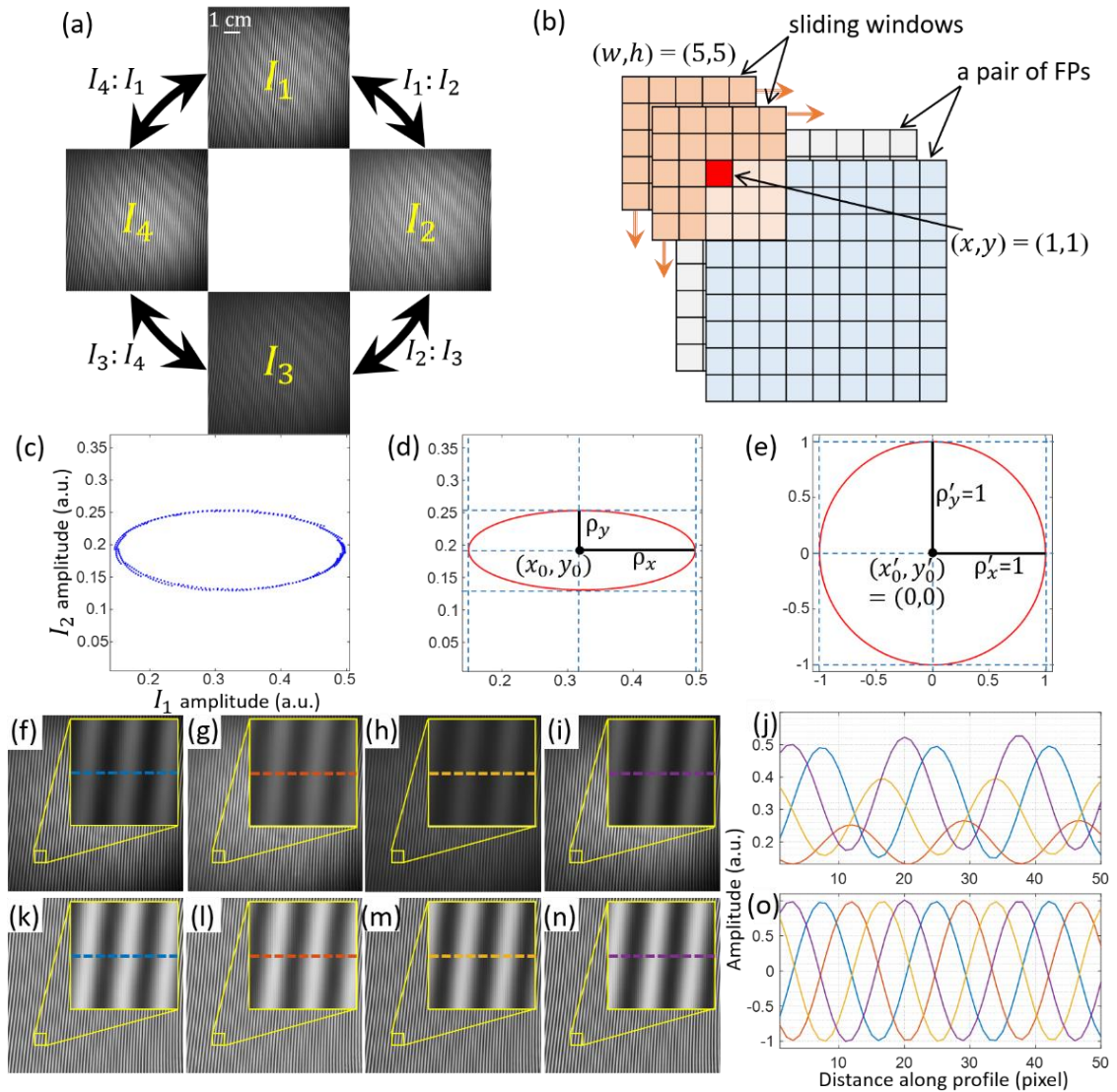


Figure 4-2: Normalization process for phase extraction from four spectral fringe patterns. a) Four adjacent pairs of FPs. b) Schematic of a pair of identical windows

sliding over a pair of adjacent FPs. c) Example of intensity plots of I_2 against I_1 for a sliding window (25,25) pixels in size and centered at (100,400). d) Ellipse fitted with least squares method to data in panel (c). e) Normalized fitted ellipse computed from data in panel (d). f-i) Four FPs captured with the multispectral camera for a flat surface after filtering with a gaussian low pass filter. j) Intensity profiles along the dashed lines within the regions indicated in the magnified parts of (f-i). k-n) The normalized FPs corresponding to data in panels (f-i). o) Intensity profiles along the dashed lines within the regions indicated in the magnified parts of (k-n).

Due to the design of the MFA, the FPs are expected to cover 4 phase-steps in increments of $\pi/2$ resulting in normalized Lissajous plots. However, with measurements, there are always some errors in the phase shift. Figure 4-3 shows examples of the normalized fitted ellipses for the four possible pairs with the value of the estimated phase shift among the FPs for the specific window and the data represented in Figure 4-2. The term $I_m : I_n$ refers to plot I_n against I_m . In this example, the maximum error was almost 17 degrees, which was significant and could easily affect the phase map retrieved with Eq. (4-3). The discrepancies could be caused by measurement and geometric errors, including those caused by optics used to expand the patterns and camera lens effects [32,33].

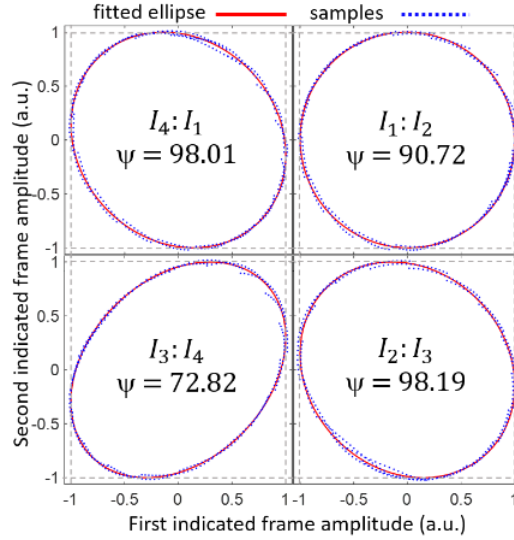


Figure 4-3: Example of the phase step estimation for all four FP pairs based on the normalized Lissajous figure.

To cope with measurement and geometric errors, we used the actual phase shift information in the phase map calculation. Since the phase shift steps were not necessarily evenly spaced, the FPs were represented as:

$$I_n = A + B \cos[\phi + \psi_n] \quad (4-10)$$

where ψ_n represents the phase step for $n = 1, 2, \dots, N (N \geq 3)$. The phase can be calculated as [34]:

$$\phi = \arctan \left(\frac{\sum_{k=1}^N \sum_{l=1}^N \sum_{n=1}^N I_n [\cos(\psi_k) - \cos(\psi_l)] [\cos(\psi_k) \sin(\psi_l) + \cos(\psi_n) \sin(\psi_k) + \cos(\psi_l) \sin(\psi_n)]}{\sum_{k=1}^N \sum_{l=1}^N \sum_{n=1}^N I_n [\sin(\psi_k) - \sin(\psi_l)] [\cos(\psi_k) \sin(\psi_l) + \cos(\psi_n) \sin(\psi_k) + \cos(\psi_l) \sin(\psi_n)]} \right) \quad (4-11)$$

In our case, we utilized four-step phase-shifting ($N = 4$), where ψ_1 was considered zero and ψ_2 , ψ_3 , and ψ_4 were the estimated phase-step values calculated using Eq. (4-9) between $I_1 : I_2$, $I_2 : I_3$, and $I_3 : I_4$ respectively. Therefore, for every pixel coordinate, the surrounding pixel values and Lissajous figure principal axis gave an estimation of the actual phase shift, which was later used in Eq. (4-11) to retrieve the phase map more accurately.

4.4 Results

To test the performance of the preprocessing method, we designed a simulation in two parts. First, to evaluate the performance of the equalization step and then, to test the performance of the angle offset detection step. For the first part, we simulated a set of 4 phase-shifted fringe patterns each containing 5 vertical fringes in a frame of 50 by 50 pixels, accompanied by zero-mean Gaussian white noise with a variance of 0.001. Every other frame had phase shifts fixed at 90 degrees. The background was changed from 0 indicating there was no background for all four frames up to a value of 20 which indicated the amplitude of the next frame was 20 times that of the previous frame (first frame amplitude set to a non-zero value). The modulation amplitude changed from 0, the ideal case, when all frames had the same dynamic range, to 20, when the next frame had an amplitude 20 times that of the previous one. The set of 4 frames was constrained to be within the range $[0, 1]$ for each iteration prior to feeding the frames to the normalization process described in Figure 4-2, to normalize every frame to the range of $[-1, 1]$. Using this method, the (15,15) windows were used to ensure that each window would cover a full fringe. The mean square error (MSE) between the results and a set of ideal fringe patterns was used as the performance indicator. Based on the error indicator, the normalization method proved to be perfect when the background and modulation amplitudes differ by less than 5 times between two nearby FPs (Figure 4-4 (a)).

For the second simulation, the 4 phase-shifted frames were designed the same way as in the previous simulation, but the background for all frames was set to 0, the modulation amplitude was the same, and the range was set to $[-1, 1]$. In an iteration, shifts in phase between adjacent frames have been altered. Between the 1st and 2nd frames, the phase shifts ranged from 45 degrees to 135 degrees (i.e. -45 degrees to +45 degrees off from the ideal). One-third of the designed offset was allocated to each other phase shift during each iteration, to maintain the total phase shift to 360 degrees for the sets of FPs. Figure 4-4 (b) compares the measured phase shifts between the first 2 frames with the simulated phase shifts (including offsets) between them. A comparison of measured phase shifts to the ideal values revealed that the error is always within a range of 0 to 4 degrees, which did not impact the phase measurements appreciably.

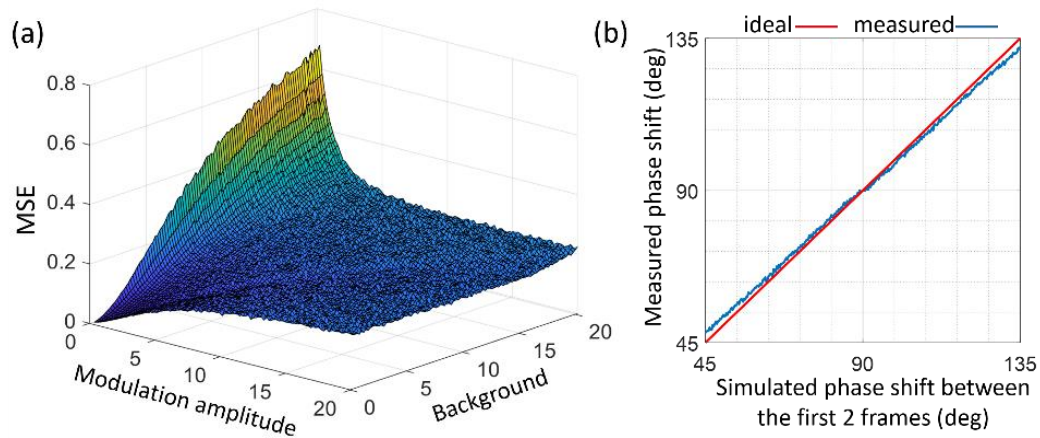


Figure 4-4: Simulations to test the performance of the pre-processing explained in the method section for a) normalization and b) angle offset detection.

To test the performance of the proposed normalization technique with our setup, the imaged object was set to be a flat rigid surface. Each raw output image from the multispectral camera was demosaiced into 4 spectral images using vendor-supplied software. Each spectral image contained a non-distorted FP related to a specific wavelength and all four FPs constructed a 4-step phase-shifted set of FPs. Figure 4-5 shows the phase map retrieved with different methods including through computation of Eq. (4-3) for non-normalized FPs (low pass filter only), Eq. (4-3) for normalized FPs, and Eq. (4-11) for normalized FPs. Since the object was a rigid flat surface, it was expected that the absolute phase map showed a ramp where every fringe produced $2 \times \pi$ linear value change. The calculated phase map with Eq. (4-3) for non-normalized patterns showed significant error in the wrapped phase (Figure 4-5 (a)) and subsequently in the unwrapped phase (Figure 4-5 (b)) due to the existence of the intensity biased in the original (i.e., acquired) FPs. Employing the normalization process over the FPs before employing Eq. (4-3) improved the wrapping and unwrapping (Figure 4-5 (d) and (e), respectively); however, the phase maps still showed a periodic error over the phase map alongside the normal of the fringes. This error was a result of the phase offset of the FPs and could be mitigated with the third method, where the actual phase shifts were estimated through Eq. (4-11) (Figure 4-5 (g-i)). Comparing the line profiles to the ideal case illustrated these errors more clearly in terms of scope and variations (Figure 4-5 (j)).

The green line, which indicated the difference between the third method and the ideal flat surface, showed the smallest error. Nevertheless, it also showed a slight variation due to the non-ideal nature of the target surface and the presence of systematic errors such as internal noise of the camera and light fluctuations.

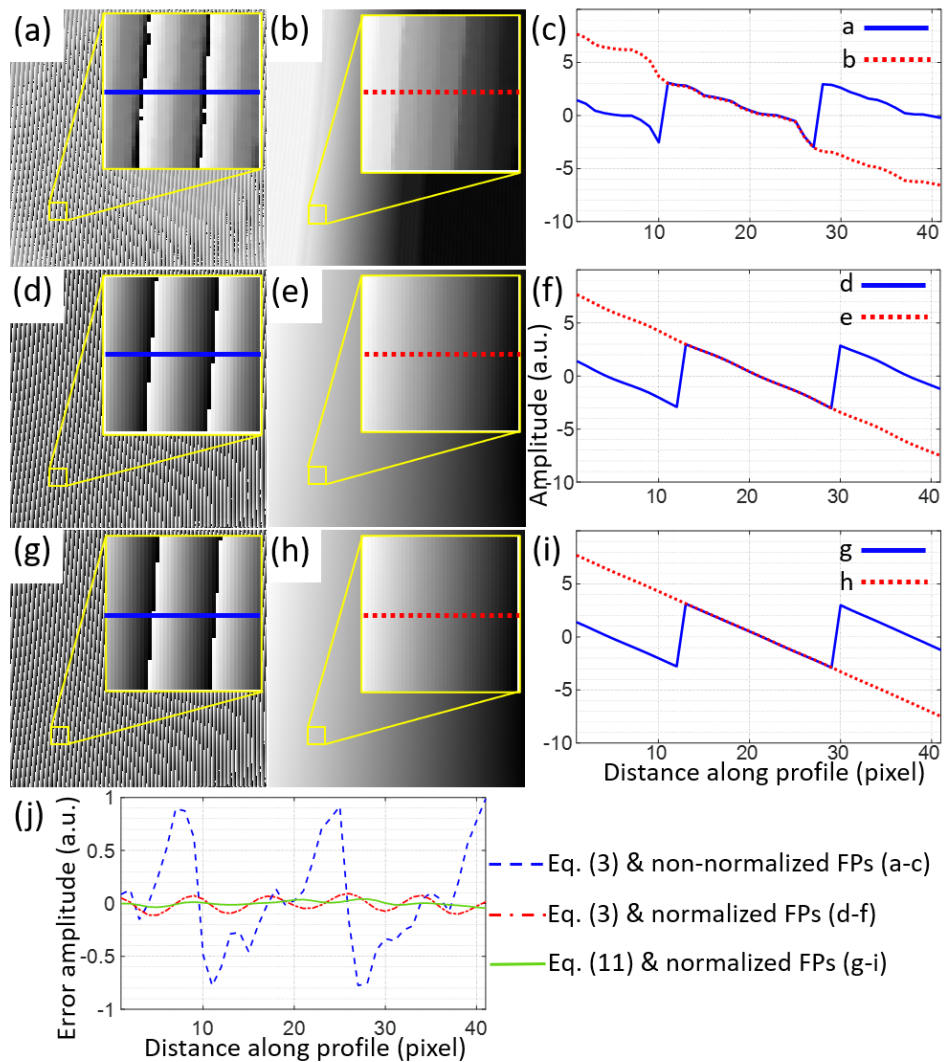


Figure 4-5: Phase retrieval process for a flat object. Wrapped phase map (a), unwrapped phase map (b), and line profiles obtained using Eq. (4-3) with FPs before normalization (c). d-f) Same as (a-c) after normalization over FPs. g-i) Same as (a-c) using Eq. (4-11) and FPs after normalization. j) Comparison of the profiles obtained using the different phase retrieval methods to the ideal case (flat imaged object) which shows the phase error.

Multiple objects were measured with the multispectral system, and the results were processed and shown in Figure 4-6. The figure illustrates the raw images taken by the multispectral camera, the measured wrapped phase maps, the height maps, and 3D representations of each object. The height maps were obtained by removing the background from the absolute unwrapped phase map and then converting to height. To remove the background in each experiment, the object was replaced with a reference flat plane (e.g., the object used in Figure 4-5), the absolute phase map of the reference was calculated and subtracted from the calculated phase map of the object. The resultant background-removed phase map was converted into a height map using a nonlinear calibration method described by Jia et al. (2007) [35]. Complex targets were selected for each experiment to demonstrate the robustness of the system. The first target was a paper cube with one corner facing the camera (Figure 4-6 (a-d)). The cube tested the system against an object with multiple flat faces each with a different surface normal to the projector/camera baseline. The gently sloped surface feature (Figure 4-6 (b) left of center) was characterized with fewer fringes and was prone to under sampling errors. On the other hand, features with steeper slopes were sampled with a greater number of fringes and less error (Figure 4-6 (b) top right and center right). Figure 4-6 (e-h) shows the results for a plastic head phantom. With this phantom, the system was tested to illustrate how well it can detect fine details of an object as well as coarse features. Note that the reflectiveness of the phantom material caused glare which led to noise in the results. The final two objects were two different gestures of a male hand showing the back of the hand (Figure 4-6 (i-l)) and the hand holding two ping-pong balls (Figure 4-6 (m-p)). The two experiments were designed to assess the capability of the system to image an object that has complex responses to the spectral bands, like human skin. As shown in Figure 4-6 (m), the CP reflection from the skin is less intense than that of the plastic ping-pong balls. However, even with diverse reflection conditions, the system succeeded in decomposing the FPs.

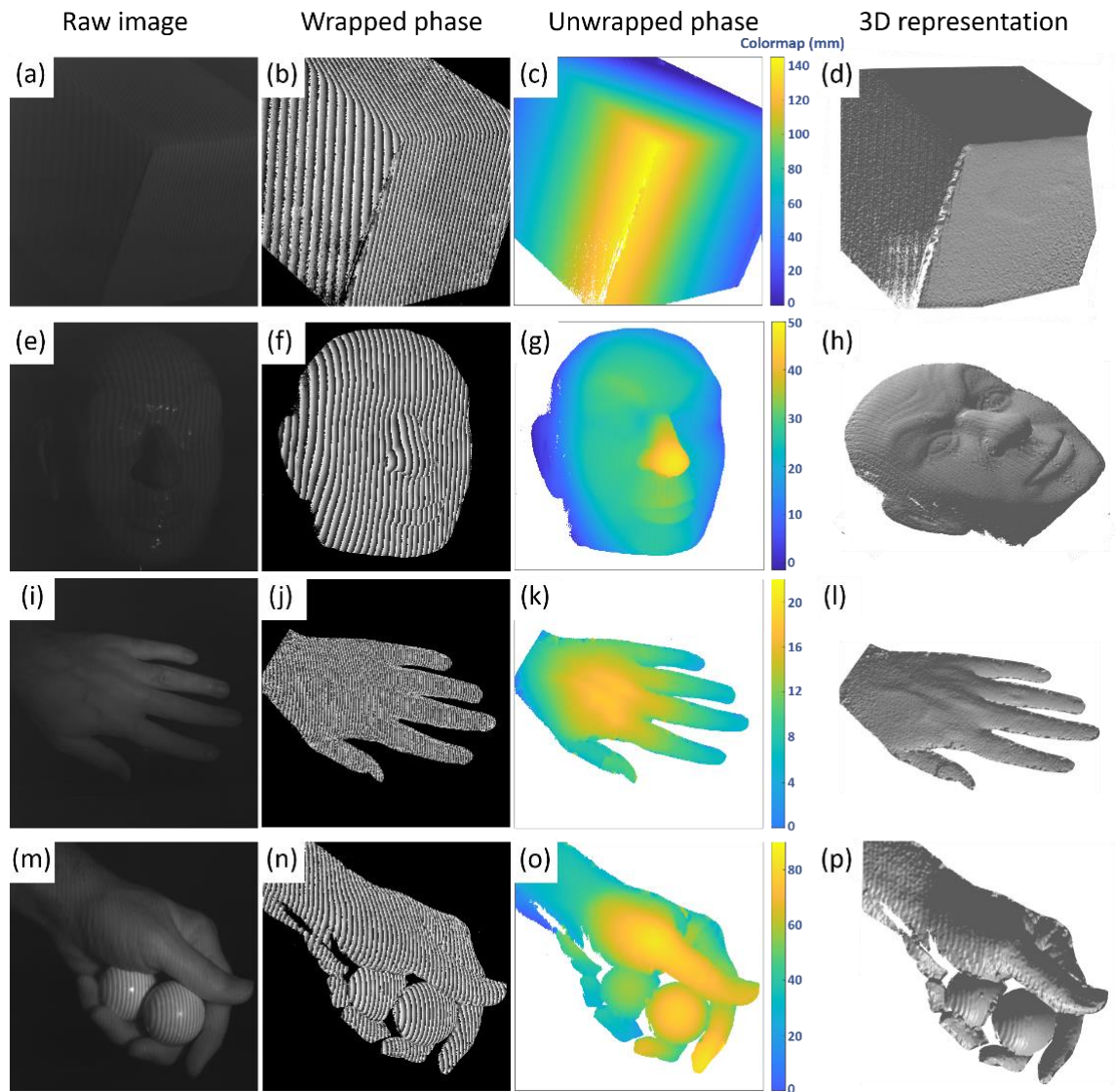


Figure 4-6: 3D imaging of complex objects. The left column shows the raw images captured by the multispectral camera before demosaicing. The second column shows the wrapped phase maps. The third column shows the color-coded height maps. The right-most column shows 3D visualizations of the height map. a-d) A cube object, e-h) a plastic head phantom, i-l) back surface of a hand, and m-p) a hand holding two ping-pong balls.

4.5 Discussion and conclusion

4.5.1 Overview

This work introduces a novel multispectral CP that delivers four phase-shifted FPs in a single frame. In addition, a multispectral camera was used to capture the frame in one snapshot. The resulting single-shot imaging system is capable of phase-shifting FPP with high temporal resolution and precise pixel-wise phase retrieval. However, the acquired FPs had different modulation and background intensities, causing non-negligible phase offsets between the FPs which led to errors in the process of phase retrieval. We implemented a normalization method based on the Lissajous figure to eliminate the background and equalize the modulation. Moreover, a numerical calibration was performed to estimate the exact phase steps between the FPs and compensate for the effect of the phase offset error.

4.5.2 Major findings

The multispectral CP method presented in this paper relied on PSP algorithms to retrieve the phase map of the object. Because of this, the measurement was pixel-wise and less sensitive to fringe quality compared to spatial phase stepping methods. In addition, due to the nature of the PSP algorithms, all processing took place without reliance on human intervention. This achievement, along with the fact that our method captured 4 phase-shifted FPs simultaneously, contributed to the effectiveness of the technique.

Characterization of objects (Figure 4-6) demonstrated that the method was successful in localizing errors and preventing them from spreading. Locally erroneous pixels like the shadowed area in Figure 4-6 (m) and the glare area in Figure 4-6 (e) could easily spread to other pixels in a spatial phase-stepping algorithm, but in our case the errors were kept highly localized. Furthermore, the system was insensitive to variable responsivity between FP channels even for difficult surfaces such as human skin (Figure 4-6 (i) and (m)), whose reflection properties are not the same for all spectral bands.

4.5.3 Comparison to previous works

In comparison to other CP platforms that allow for single-shot PSP, our method offers several advantages. As opposed to grayscale CPs based on amplitude modulation [15,16], multispectral CPs can expand the number of patterns in a single CP without compromising the dynamic range. Moreover, the data generated by our method is much easier to process since it does not require demodulation. It only requires a demosaicing procedure to separate the different FPs. Contrary to color camera approaches [24,25], multispectral cameras give access to a greater number of unique color channels. Therefore, the camera can be customized according to the application and the target. For instance, the system can use invisible patterns for security applications. Additionally, the bandwidth of multispectral cameras can be significantly narrower compared to standard color cameras greatly lowering crosstalk between spectral channels. Crosstalk is one of the primary sources of phase noise in color CP methods [27].

4.5.4 Procedure achievements

This paper presents a four-step phase-shifting FPP normalization method modeled after a well-known technique. For the case where both background and modulation amplitude vary 500% from one FP to the next, simulation results (Figure 4-4 (a)) show that our method is highly effective at removing background and retrieving the modulation amplitudes for 4 phase-shifted frames. A method based upon the parameters already calculated for the normalization method was used in order to estimate the exact phase shift from one FP to the next. We observed that even if the phase difference between 2 nearby FPs has an error by up to 45 degrees from the expected (90 degrees), the algorithm could still detect the phase offset with an error less than 4 degrees (Figure 4-4 (b)). It is noteworthy that although the current method was designed specifically for a four-step phase shift protocol, the technique could be generalized to estimate phase shift between any two FPs.

4.5.5 Limitations

An issue that can be seen from the results presented in Figure 4-6 (d, h, and p) is under-sampling errors. This can impact the retrieved phase map when the number of phase shifts is not enough to sample the object variation or the fringes are not perfectly sinusoidal [36,37]. The problem is especially evident on surfaces with steep slopes related to the baseline of the camera-projector. One possible solution for this problem is to increase the number of spectral bands in the MFA. Furthermore, due to the narrow bandwidth of the MFA, light transmission was reduced compared to white light approaches. This required a more powerful light source be used in order to project enough light onto the object so that the camera could form a high-quality image. We used a 100 W QTH source to generate the desired pattern at a distance of almost 50 cm in our experiment. Using a more powerful light source, however, could yield better images and shorter exposure times.

4.5.6 Future works

The snapshot capability of the system allows for robust 3D imaging of dynamic objects since only one camera exposure is needed to obtain the full phase-shifted data set. With this feature, the camera is less sensitive to vibrational noise since the exposure time of the camera can be reduced to compensate. Taking advantage of the fact that the speed of the multispectral CP 3D imaging is limited only by the camera frame rate, the system should be extremely useful for real-time 3D measurements related to mobile devices, robotics, and 3D color video.

4.6 Funding.

This work was supported by grants from the Natural Sciences and Engineering Research Council of Canada and the Canadian Institutes of Health Research to JJLC and MD.

4.7 Acknowledgments.

The authors thank Spectral Devices Inc for providing the multispectral filter array and the snapshot multispectral camera for this work.

4.8 Disclosures.

Jeffrey Carson and Mohamadreza Najiminaini are co-founders, directors, and shareholders in Spectral Devices Inc., which supplied the multispectral filter array and the multispectral camera for this work. Parsa Omid and Mamadou Diop have no competing interests.

4.9 References

1. J. Salvi, S. Fernandez, T. Pribanic, and X. Llado, "A state of the art in structured light patterns for surface profilometry," *Pattern Recognit.* 43, 2666–2680 (2010).
2. P. Omid, L. C. M. Yip, H. Wang, and M. Diop, "SoftwareX PhaseWare : Phase map retrieval for fringe projection profilometry and off-axis digital holographic interferometry," *SoftwareX* 13, 100652 (2021).
3. X. S. and W. Chen, "Fourier transform profilometry: a review," *Opt. Lasers Eng.* 35, 263–284 (2001).
4. W. Yin, S. Feng, T. Tao, L. Huang, M. Trusiak, Q. Chen, and C. Zuo, "High-speed 3D shape measurement using the optimized composite fringe patterns and stereo-assisted structured light system," *Opt. Express* 27, 2411 (2019).
5. Z. H. Zhang, "Review of single-shot 3D shape measurement by phase calculation-based fringe projection techniques," *Opt. Lasers Eng.* 50, 1097–1106 (2012).
6. C. Y. Liu and C. Y. Wang, "Investigation of Phase Pattern Modulation for Digital Fringe Projection Profilometry," *Meas. Sci. Rev.* 20, 43–49 (2020).
7. L. Huang, C. Ng, and A. K. Asundi, "Dynamic 3D measurement for specular reflecting surface with monoscopic fringe reflection deflectometry," *Opt. InfoBase Conf. Pap.* 19, 12809–12814 (2011).
8. J. L. Flores, B. Bravo-Medina, and J. A. Ferrari, "One-frame two-dimensional

- deflectometry for phase retrieval by addition of orthogonal fringe patterns," *Appl. Opt.* 52, 6537–6542 (2013).
9. M. T. Nguyen, Y. S. Ghim, and H. G. Rhee, "Single-shot deflectometry for dynamic 3D surface profile measurement by modified spatial-carrier frequency phase-shifting method," *Sci. Rep.* 9, 1–15 (2019).
 10. W.-H. Su and H. Liu, "Calibration-based two-frequency projected fringe profilometry: a robust, accurate, and single-shot measurement for objects with large depth discontinuities," *Opt. Express* 14, 9178 (2006).
 11. M. Takeda, Q. Gu, M. Kinoshita, H. Takai, and Y. Takahashi, "Frequency-multiplex Fourier-transform profilometry : a single-shot three-dimensional shape measurement of objects with large height discontinuities and surface isolations," *Appl. Opt.* 36, 5347–5354 (1997).
 12. C. A. García-Isáis and N. Alcalá Ochoa, "One shot profilometry using a composite fringe pattern," *Opt. Lasers Eng.* 53, 25–30 (2014).
 13. C. A. García-Isáis and N. Alcalá Ochoa, "One shot profilometry using phase partitions," *Opt. Lasers Eng.* 68, 111–120 (2015).
 14. G. Du, M. Wang, C. Zhou, S. Si, H. Li, Z. Lei, and Y. Li, "One shot profilometry using iterative two-step temporal phase-unwrapping," *Opt. Appl.* 47, 97–110 (2017).
 15. C. Guan, L. G. Hassebrook, and D. L. Lau, "Composite structured light pattern for three-dimensional video," *Opt. Express* 11, 406 (2003).
 16. Y. He and Y. Cao, "A composite-structured-light 3D measurement method based on fringe parameter calibration," *Opt. Lasers Eng.* 49, 773–779 (2011).
 17. H. M. Yue, X. Y. Su, and Y. Z. Liu, "Fourier transform profilometry based on composite structured light pattern," *Opt. Laser Technol.* 39, 1170–1175 (2007).

18. S. Yang, Z. Hairong, L. Zhipei, and J. Jun, "Influence of sampling on composite structured light pattern," 5th Int. Conf. Inf. Technol. Appl. Biomed. ITAB 2008 conjunction with 2nd Int. Symp. Summer Sch. Biomed. Heal. Eng. IS3BHE 2008 171–174 (2008).
19. Y. You, Y. Shen, G. Zhang, and X. Xing, "Real-time and high-resolution 3D face measurement via a smart active optical sensor," *Sensors (Switzerland)* 17, (2017).
20. Y. C. Wu, Y. P. Cao, Z. F. Huang, M. T. Lu, and D. L. Chen, "Improved composite Fourier transform profilometry," *Opt. Laser Technol.* 44, 2037–2042 (2012).
21. Philip Fong and F. Buron, "Sensing Deforming and Moving Objects with Commercial Off the Shelf Hardware," 101–101 (2006).
22. H. J. Chen, J. Zhang, D. J. Lv, and J. Fang, "3-D shape measurement by composite pattern projection and hybrid processing," *Opt. Express* 15, 12318 (2007).
23. W.-H. Su, "Color-encoded fringe projection for 3D shape measurements," *Opt. Express* 15, 13167 (2007).
24. J. L. Flores, J. A. Ferrari, G. García Torales, R. Legarda-Saenz, and A. Silva, "Color-fringe pattern profilometry using a generalized phase-shifting algorithm," *Appl. Opt.* 54, 8827 (2015).
25. I. Trumper, H. Choi, and D. W. Kim, "Instantaneous phase shifting deflectometry," *Opt. Express* 24, 27993 (2016).
26. M. Wu, N. Fan, G. Wu, S. Zhang, and F. Liu, "An inverse error compensation method for color-fringe pattern profilometry," *J. Opt. (United Kingdom)* 22, (2020).
27. Y. Wan, Y. Cao, X. Liu, T. Tao, and J. Kofman, "High-frequency color-encoded fringe-projection profilometry based on geometry constraint for large depth range," *Opt. Express* 28, 13043 (2020).

28. "Multispectral snapshot cameras,"
<https://www.spectraldevices.com/products/multispectral-snapshot-cameras>.
29. C. Zuo, S. Feng, L. Huang, T. Tao, W. Yin, and Q. Chen, "Phase shifting algorithms for fringe projection profilometry: A review," *Opt. Lasers Eng.* 109, 23–59 (2018).
30. F. Liu, Y. Wu, F. Wu, N. König, R. Schmitt, Y. Wan, and Y. Xu, "Precise phase demodulation of single carrier-frequency interferogram by pixel-level Lissajous figure and ellipse fitting," *Sci. Rep.* 8, 1–11 (2018).
31. T. Požar and J. Možina, "Enhanced ellipse fitting in a two-detector homodyne quadrature laser interferometer," *Meas. Sci. Technol.* 22, (2011).
32. P. De Groot, "Phase-shift calibration errors in interferometers with spherical Fizeau cavities," *Appl. Opt.* 34, (1995).
33. Y. Takahashi, "Effect of Phase Error in Phase-Shifting Interferometer," 888, 11–16 (2019).
34. G. A. Ayubi, I. Duarte, and J. A. Ferrari, "Optimal phase-shifting algorithm for interferograms with arbitrary steps and phase noise," *Opt. Lasers Eng.* 114, 129–135 (2019).
35. P. Jia, "Comparison of linear and nonlinear calibration methods for phase-measuring profilometry," *Opt. Eng.* 46, 043601 (2007).
36. Y. Surrel, "Measurements By the Use of Phase Stepping," *Appl. Opt.* 35, 51–60 (1996).
37. S. Ri, Q. Wang, P. Xia, and H. Tsuda, "Spatiotemporal phase-shifting method for accurate phase analysis of fringe pattern," *J. Opt. (United Kingdom)* 21, (2019).

Chapter 5

5 Algorithm for phase-displacement conversion from reflection digital holographic interferometry

Publication status: The chapter has been published as a paper in the Practical Holography XXXIII: Displays, Materials, and Applications. International Society for Optics and Photonics (<https://www.spiedigitallibrary.org/conference-proceedings-of-spie/10944/109440Q/Algorithm-for-phase-displacement-conversion-from-reflection-digital-holographic-interferometry/10.1117/12.2507566.short?webSyncID=7620c89a-0ce4-6e9e-6ec7-a49dab6a0cba&sessionGUID=d059329a-d883-c9d9-02bc-9993ced268be&SSO=1&tab=ArticleLinkCited>).

5.1 Abstract

Our group has developed a digital holographic interferometry camera based on an off-axis dual-beam setup. A single hologram acquired with the camera represents the phase and intensity distributions of light reflecting off the surface of an object. Our goal was to develop an algorithm that converted the acquired hologram into a 3D representation of the object. First, to determine the phase excursion of the object, a discrete Fresnel transform reconstruction was applied to a high-pass-filtered version of the hologram. The reconstructed phase map contained both the spatial carrier fringes due to the off-axis geometry of our setup and the phase information related to the object's surface. Next, we developed a reliable 2D spatial carrier fringe removal technique that was capable of separating out the object's phase information from the carrier fringes. Last, the object phase map was calibrated to convert the phase information to height information based on the geometrical parameters of the system. The system was evaluated using a silicon-etched lateral-axial resolution target based on a USAF design. The system achieved 33 nanometer axial resolution and sub-pixel lateral resolution over a wide field of view of more than 10 mm x 10 mm. The algorithm will enable the digital holographic camera to be used for non-destructive testing of surface morphology at nanometer scales. With

repeated acquisitions, the algorithm has the potential to estimate nanometer-scale dynamic vibrations of an object's surface.

5.2 Introduction

Digital holographic interferometry (DHI) is an imaging technique that allows 3D non-contact surface measurements [1], deformation measurements [2], and dynamic vibration measurements [3]. DHI is a digital photo-recording of the interference between a coherence light wave (reference beam) and a scattered version of the same wave from an object (object beam). The scattered wave contains information on the object's surface characteristics.

The complex-amplitude distribution of the object wave can be reconstructed numerically using the recorded holograms based on diffraction theory. It contains both the intensity and the phase information of the object. To obtain 3D surface measurements of an object, the phase is extracted and converted to surface displacement information. Phase extraction techniques are dependent on the geometry of the DHI recording setup. Generally, the recording can be performed in-line (on-axis) or off-axis [4]. In-line DHI, first proposed by Gabor [5], uses the same optical axis for the reference and object beams. Off-axis DHI, first proposed by Leith [6], utilizes a small tilt between the optical axes of the reference and object beams. The reconstructed image contains three terms: zero order, real, and virtual image terms. The first term provides the non-diffracted part of the interferogram and is equivalent to the DC component. The other two terms contain conjugate information called twin images. For the in-line configuration, the three terms overlap. In order to extract the phase, a phase shift device in one of the optical beams is required and at least two holograms must be captured with the phase steps due to the phase shifter [7]. The off-axis configuration provides interference fringes that include a carrier signal and spatially modulated scattered signal. The carrier signal separates the twin images symmetrically in relation to the DC part. The amount of separation is affected by the off-axis angle in the setup. However, the angle limits the maximum measurable object spatial frequency [8] and must fulfill the Shannon sampling theorem [9]. The sensitivity of the reconstructed image is related to the number of pixels

which include the virtual or real term information. The off-axis setup typically uses one-ninth of the number of pixels that an in-line setup uses [10]. Moreover, off-axis configurations extract the phase information with just a single hologram, contrary to the in-line setup which need multiple holograms to extract the phase. Therefore, the off-axis setup has higher temporal sensitivity and can be used for rapid dynamic deformation measurements.

In this paper, we describe an algorithm that converts a single hologram into a 3D representation of the object. We tested the algorithm using a digital holographic recording system based on an off-axis dual-beam setup developed in our lab. The system was designed to measure the surface roughness of reflective objects. The field of view was greater than 100 mm² and the sensitivity approached 10 nm axially and several microns laterally.

5.3 Method and results

5.3.1 Digital holographic interferometry recording

For DHI, we used a Helium-Neon laser at 633 nm (Thorlabs). The beam was filtered and expanded to enable adjustment of the power and collimation of the beam. A polarized beam splitter was used to divide the beam into reference and object beams. The object beam scattered off the object and interfered with the reference beam on the surface of a CCD sensor producing a hologram. The angle between the reference and scattered object beams was 2.3°. The CCD sensor had 1040×1376 pixels with 6.45 μm pixel size in both x and y.

The sensor captured the intensity of the interference, which was represented by the following equation:

$$\begin{aligned} I_H(x, y) &= |O(x, y) + R(x, y)|^2 = (O(x, y) + R(x, y))(O(x, y) + R(x, y))^* \quad (5-1) \\ &= |O(x, y)|^2 + |R(x, y)|^2 + O(x, y)R^*(x, y) + R(x, y)O^*(x, y) \end{aligned}$$

Where $O(x, y)$ and $R(x, y)$ indicate the object and reference beams respectively and $*$ denotes the conjugate complex. The two first terms on the right side of the equation are

the autocorrelation of the object and reference waves, show the zero order. The third term is the real image, and the last term represents the virtual image.

5.3.2 Numerical reconstruction

The function of the digital holography reconstruction, introduced by Goodman and Lawrence [11], is to provide a focused image of the object from the recorded hologram. That is to distinguish the object wave $O(x, y)$ from the recorded interference pattern $I_H(x, y)$, in equation(5-1). The hologram is a digitally sampled image of the interference. The diffraction model of the hologram at the reconstruction plane is represented with the Fresnel–Kirchhoff integral. The reconstruction contains both the intensity and the phase information of the object wave. To solve the numerical integral, Verrier and Atlan have categorized the off-axis digital hologram reconstruction methods into two general families based on the number of Fast Fourier Transforms (FFT) [9]. The first family are the Fourier based approaches, which use only one FFT and are suitable for cases where there is a great distance between the object and the image sensor. The second family are called the convolutional-based approaches, which use two or three FFTs and are suitable for reconstruction of the hologram recorded near the object. These methods provide qualitative images as well as quantitative phase information of the object, amplitude-contrast and phase-contrast images, respectively. In the reconstruction process, the reference wave is called reconstruction wave and the distance between the reconstruction plane and the sensor is the reconstruction distance (d). The parameter d is equal to the optical path length, i.e., the distance between the object and the sensor. A positive d indicates that the focus of the reconstruction is of the real image, in front of the hologram. A negative d indicates that the focus is of the virtual image located behind the hologram [12]. For our system situation, we applied a single FFT algorithm to provide amplitude and phase contrast focused in front of the hologram. The phase information was used to provide a 3D representation of the object. In the process, an object with nanometer scale surface roughness was tested.

The first step of the algorithm was to compute the reference wave. A perfectly collimated wave can be formulated as:

$$R(x, y) = A_R \exp \left[\frac{i(2\pi)}{\lambda} (x\Delta x + y\Delta y) \right] \quad (5-2)$$

Where A_R represents the intensity value and $(\Delta x, \Delta y)$ represents the sensor pixel size. By applying this estimation for the reference, any aberration in the collimated reference wave leads to an aberration in the reconstruction. The next step was to multiply the reference with the hologram and apply the FFT as an equivalent of the Fresnel diffraction integral. The resultant complex amplitude included three terms. We used a high-pass filtered version of the hologram in the algorithm to remove the DC component and recover the twin images. By this method, the zero term did not disturb the twin images. Figure 5-1 (a) shows a hologram of a reflective USAF target. Figure 5-1 (b) shows the amplitude of the reconstruction of the zero-padded hologram shown in Figure 5-1 (a). Both amplitude (Figure 5-1 (c)) and phase (Figure 5-1 (d)) information of the object can be recovered by applying a proper filter to the reconstructed complex matrix. The filter must cover the focused part of Figure 5-1 (b), which indicates the real image. The recovered phase encompassed the carrier phase induced by the off-axis angle. The carrier phase emerged as linear fringes, with orientation and frequency related to the off-axis angle direction and value, respectively. The roughness of the surface changes the direction of these fringes (Figure 5-2 (b)). Therefore, to detect the roughness, the fringe behavior should be detected. The calculated phase in Figure 5-1 (d) has low contrast due to several reasons, including nonlinearity of the sensor, nonuniform illumination, and nonuniform reflectivity of the object's surface. To obtain higher quality fringes, we must apply a fringe enhancement technique on the calculated phase [13]. The phase can be formulated as:

$$f(x, y) = A(x, y) + B(x, y) \cos(\varphi(x, y) + \omega_x x + \omega_y y) + n(x, y) \quad (5-3)$$

where (x, y) is the image coordinate, $f(x, y)$ is the 2D intensity pattern, $A(x, y)$ is the low-frequency background offset, $B(x, y)$ is fringe amplitude, $\varphi(x, y)$ is phase distribution, (ω_x, ω_y) is carrier frequency, and $n(x, y)$ is the noise. Poor quality fringe patterns have local contrast values less than 1, where contrast is defined as:

$$V(x, y) = B(x, y)/A(x, y) \quad (5-4)$$

To enhance the contrast, the value should be normalized to 1. This can be done simply by defining the fringe pattern as:

$$f_{enhanced}(x, y) = \frac{1}{2} + \frac{f(x, y) - \langle f(x, y) \rangle}{f_M(x, y) - f_m(x, y)} \quad (5-5)$$

where $\langle f(x, y) \rangle$, $f(x, y)$, and $f_m(x, y)$ are the local average, maximum, and minimum of the fringe pattern over a selected window. The window is centered at (x, y) and its size is set based on the local period of the \cos function. A sample of the result is shown in Figure 5-2 (d) and corresponds to the original phase shown in Figure 5-2 (a). Comparing the magnifications of the original phase and the enhanced phase in Figure 5-2 (c) and (f), it is clear that the enhanced phase allows better tracking of fringes. By using collimated imaging, 3D visualization of the unwrapped enhanced phase shows a tilted plate modulated with the object roughness (Figure 5-3). The tilt value and the plate size are dependent on the off-axis angle value and the beam size, respectively. The carrier phase should be removed to obtain the object phase.

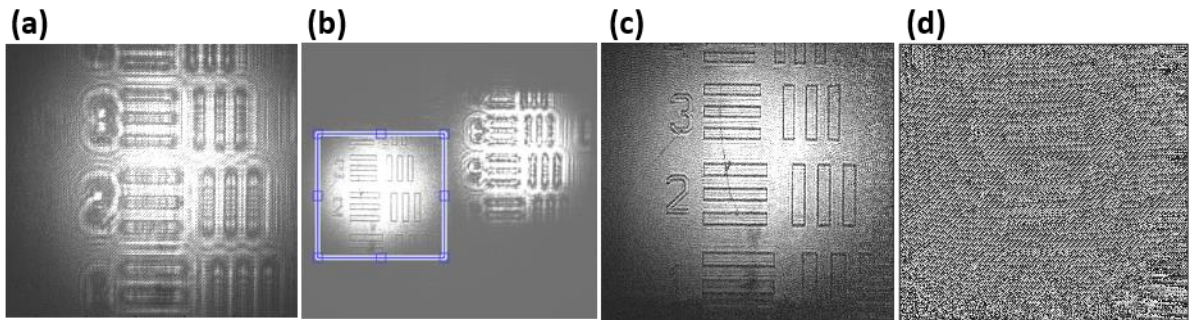


Figure 5-1: Single FFT reconstruction for off-axis holographic interferometry. a) A raw hologram. b) The reconstruction of the high-pass-filtered raw hologram, which contains the twin images as well as the weakened zero-order information. c) The amplitude image of the indicated part of the reconstructed image in (b). d) The phase image of the indicated part of the reconstructed image in (b).

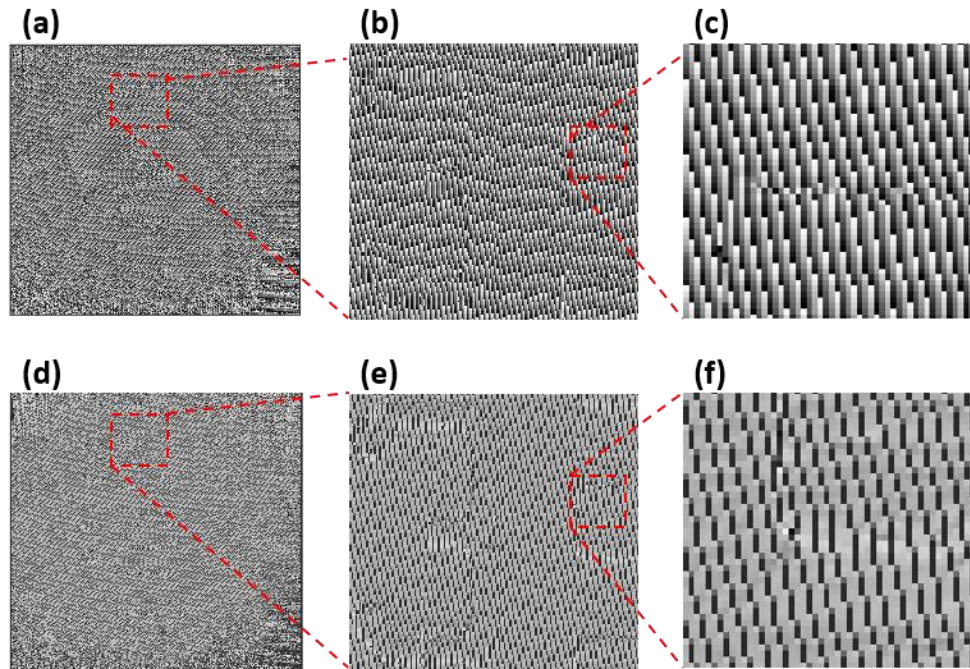


Figure 5-2: a) The original phase pattern acquired from the FFT reconstruction. Panels (b) and (c) show magnified areas indicated by the red dashed boxes. d) The contrast-enhanced image of the fringe pattern shown in panel (a). Panels (e) and (f) show magnified areas indicated by the red dashed boxes.

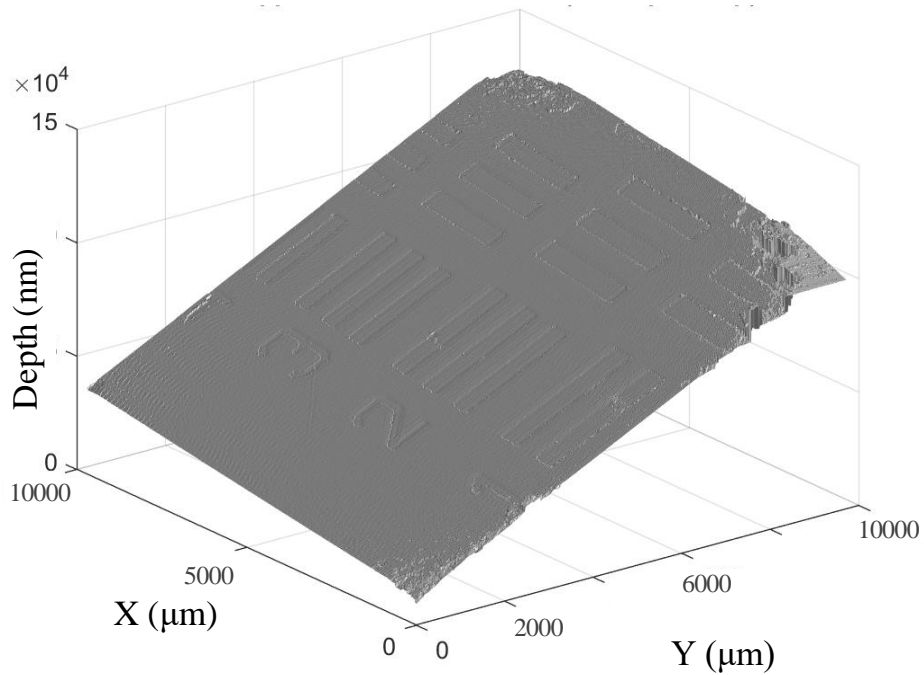


Figure 5-3: 3D visualization of the enhanced phase pattern shown in Figure 5-2(d).

The next step was demodulation of the fringe pattern. Numerous methods have been proposed to analyse the interferometry modulated fringes [14–16]. We applied the FFT technique to demodulate the object phase from the enhanced acquired phase. The fringe pattern was re-written based on Euler's rule as:

$$f(x, y) = A(x, y) + \frac{1}{2}B(x, y)\exp(i\varphi(x, y))\exp(i(\omega_x x + \omega_y y)) + \frac{1}{2}B(x, y)\exp(-i\varphi(x, y))\exp(-i(\omega_x x + \omega_y y)) + n(x, y) \quad (5-6)$$

The high carrier frequency provided effective separation of the first three terms on the right side of Eq. (5-6) in the Fourier domain. The spectra representing the second or third terms were shifted to the origin and the inverse Fourier transform was applied to remove the carrier frequency and preserve the phase distribution. A Hamming window was used during filtering. The output of the inverse Fourier transform contained the phase distribution of the object surface. The phase data was calculated using an inverse tangent

function on the reconstructed output. Hence, the recorded phase distributions wrapped and were limited to the range $[-\pi, \pi]$ (Figure 5-4 (c)). Since, phase can take any value based on variations on the sample surface, a 2D unwrapping procedure was used to obtain the real phase (Figure 5-4 (d)). In the experimental setup, illumination non-uniformity at the target influenced the phase distribution calculated with Fresnel transform procedure. Figure 5-5 (a) shows the 3D visualization of the unwrapped phase. The unevenness of illumination led to a stationary aberration in the phase that appeared as an uneven background in the unwrapped phase. The aberration can be seen in the 3D visualization in Figure 5-5 (a) and its line profile is shown in Figure 5-5 (b). Comparing Figure 5-3 to Figure 5-5 (a) revealed that the carrier phase was successfully removed; however, the background phase due to the non-uniform illumination remained. The background was removed by applying an automatic 2D polynomial background estimation and subtraction on the unwrapped phase. Figure 5-6 (a) and (b) show the estimated background and the unwrapped phase without the background, respectively. The 3D visualization of the new phase map and line profile for $Y = 5000 \mu\text{m}$ are shown in Figure 5-7 (a) and (b), respectively. From these data, it is apparent that the background phase artifact due to the uneven illumination was effectively removed.

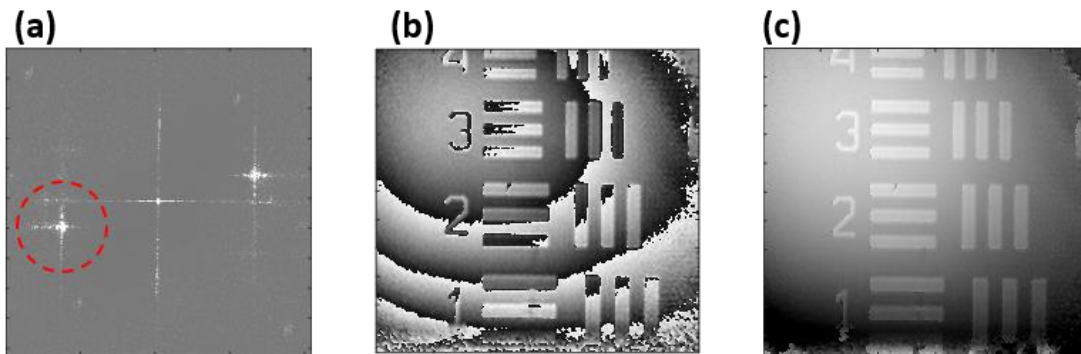


Figure 5-4: The process of phase carrier removal. a) Fourier domain of the enhanced phase map shown in Figure 5-2 (d) and the Hamming window filter to select the spectrum (dashed red circle). b) The phase acquired after applying the inverse Fourier transform to the origin-shifted and filtered spectrum. c) The 2D unwrapped phase from panel (b).

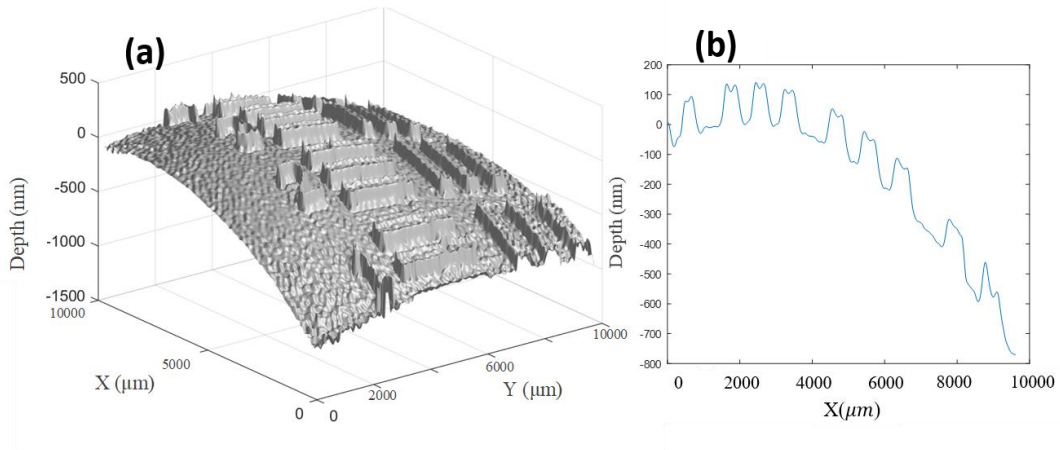


Figure 5-5: a) 3D visualization of the unwrapped phase shown in Figure 5-4 (c). b) The line profile from $Y = 5000 \mu\text{m}$ in (a).

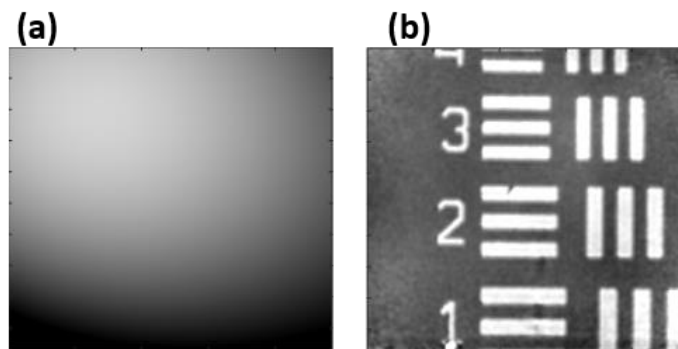


Figure 5-6: a) Estimated background phase for the unwrapped phase in Figure 5-4 (c). b) The estimated object phase computed by subtraction of the estimated background from the unwrapped phase in Figure 5-4 (c).

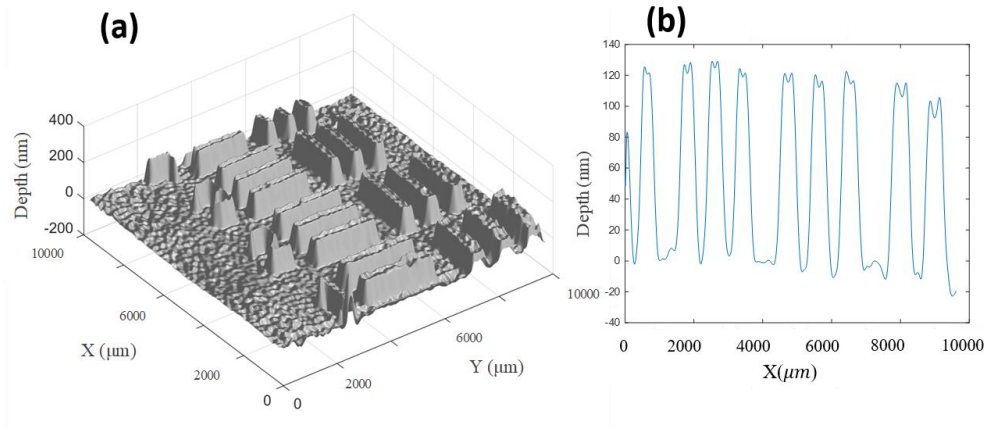


Figure 5-7: a) 3D visualization of the unwrapped phase shown in Figure 5-6 (b). b) The line profile from $Y = 5000 \mu\text{m}$ in (a).

To evaluate the lateral-axial resolution of the system, we tested the system with a silicon-etched gold standard target (GST) based on a USAF resolution target. The target was equally divided into four quadrants. Each of the target quadrants had the same pattern of bars and squares, but each quadrant was etched to a different depth of 123 nm, 82 nm, 33 nm, or 10 nm. The device was coated with 80-nm thick gold and the manufactured depth accuracy was within ± 3 nm and lateral accuracy was approximately ± 500 nm. The experimental holographic interferometry system had a $10 \text{ mm} \times 10 \text{ mm}$ field of view and the target was $50 \text{ mm} \times 50 \text{ mm}$. To measure the complete target at 25 measurements were required. As shown in Figure 5-8 (a), the system was able to detect the quadrant with 33 nm etch depth. The 82 nm and 123 nm etch depths were less challenging and easily detected by the system (data not shown). However, the features with 10 nm etch depth were just at the limit of detectability (data not shown).

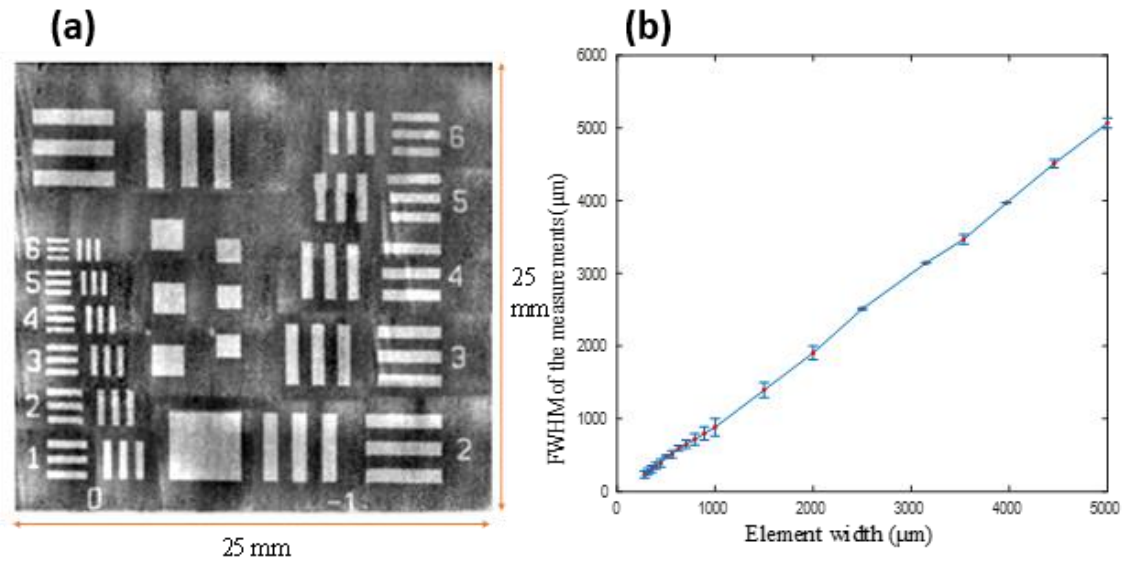


Figure 5-8: a) A scanned image of the target quadrant with 33 nm etch depth. b) The full width at half maximum (FWHM) of the minor axis of each bar shown in panel (a).

5.4 Discussion and conclusion

We developed an algorithm to convert off-axis, reflection-based holograms into 3D representations of objects. The algorithm has been tested on data acquired with a wide-field digital holographic interferometry system. As a first step, the algorithm reconstructed the object wavefront from the acquired holograms in order to calculate the intensity and the phase maps of the object. The intensity provided a clear image of the object, whereas the phase provided a linear open fringe map, indicating the phase of the fringes has been modulated by the morphological features of the object. For this reason, the algorithm attempted to demodulate the phase of the fringes in order to determine the morphological features. The phase demodulation used in this algorithm was based on Fourier transform method. The quality of the phase map was directly influenced by the quality of the fringe pattern provided by the algorithm. So, before applying phase demodulation, the algorithm enhanced the fringe map through a normalization process.

Using the setup equipment described in the method section, the algorithm could provide micrometer-scale lateral resolution and nanometer-scale axial resolution. Using this method, macroscopic surfaces can be non-destructively tested at microscopic resolutions.

5.5 References

1. T. Kreis, "Application of digital holography for nondestructive testing and metrology: A review.," *IEEE Trans. Ind. Informatics* 12(1), 240–247 (2016).
2. and F. M. S. S. Schedin, G. Pedrini, H. J. Tiziani, "Simultaneous three-dimensional dynamic deformation measurements with pulsed digital holography," *Appl. Opt.* 38, 7056–7062 (1999).
3. T. Kakue, T., Endo, Y., Nishitsuji, T., Shimobaba, T., Masuda, N. and Ito, "Digital holographic high-speed 3D imaging for the vibrometry of fast-occurring phenomena," *Sci. Rep.* 7(1), p.10413. (2017).
4. K. C. Ozsoy-Keskinbora C, Boothroyd CB, Dunin-Borkowski RE, van Aken PA, "Hybridization approach to in-line and off-axis (electron) holography for superior resolution and phase sensitivity.," *Sci Rep.* 2014;47020. (2014).
5. D. Gabor, "Apparatus for producing images of small objects by photographic means," (1947).
6. E. N. Leith and J. Upatnieks, "Reconstructed wavefronts and communication theory," *J. Opt. Soc. Am.* 52, 1123–1130 (1962).
7. I. Y. and T. Zhang, "Phase-shifting digital holography," *Opt. Lett.* **22(16)**, 1268–1270 (1997).
8. P. O. J. ptner Schnars Thomas M. Kreis, "Digital recording and numerical reconstruction of holograms: reduction of the spatial frequency spectrum," *Opt.*

Eng. 35(4), 977–982 (1996).

9. and M. A. Verrier, Nicolas, "Off-axis digital hologram reconstruction: some practical considerations," *Appl. Opt.* 50.34, H136-H146. (2011).
10. Y. I., "Phase-Shifting Digital Holography. In: Poon TC. (eds) *Digital Holography and Three-Dimensional Display.*," in *Springer, Boston, MA* (2006).
11. J. W. G. and R. W. Lawrence, "Digital image formation from electronically detected holograms," *Appl. Phys. Lett.* 11, 77–79 (1967).
12. and C. D. Cuhe, Etienne, Pierre Marquet, "Simultaneous amplitude-contrast and quantitative phase-contrast microscopy by numerical reconstruction of Fresnel off-axis holograms," *Appl. Opt.* 6994–7001 (1999).
13. and X. L. Y. L. Z. Cai, Q. Liu, "A simple method of contrast enhancement and extremum extraction for interference fringes," *Opt. Laser Technol.* 35, 295–302 (2003).
14. and F. J. C. M. Servin, J. L. Marroquin, "Demodulation of a single interferogram by use of a two-dimensional regularized phase-tracking technique," *Appl. Opt.* 36, 4540–4548 (1997).
15. E. Y. and S. S. Cha, "Two-Dimensional Regression for Interferometric Phase Extraction," *Appl. Opt.* **37**, 1370–1376 (1998).
16. M. A. O. K. G. Larkin, D. J. Bone, "Natural demodulation of two dimensional fringe patterns. I. General background of the spiral phase quadrature transform," *J. Opt. Soc. Am. A* 18, 1862–1870 (2001).

Chapter 6

6 Summary

6.1 Overview

This chapter summarizes the contributions of the studies presented in Chapters 2 to 5 of the thesis. This includes investigating and interpreting the results, and discussion of future research. Finally, the chapter ends with a conclusion section, linking the results to the objectives and goals presented in the introductory chapter.

6.2 Contributions

Chapters 2–5 present individual studies that have been formatted in journal article style. Chapter 2 describes the PhaseWare software that permits retrieval of phase information from either FPP systems outputs or off-axis DHI systems outputs. Chapters 3 and 4 present a new method for FPP that utilizes multispectral filter arrays to generate composite fringe patterns and multispectral camera to capture the pattern reflected from the surface of the objects. Chapter 5 illustrates an example of using PhaseWare to extract phase information from interferograms taken from an off-axis DHI system. The following section describe the contributions of each chapter in more detail.

6.2.1 Processing software

The goal of all the FPP and off-axis DHI analyses presented in this thesis was to derive a phase map and extract information from those phases. Estimation of phase maps for FPP systems can be performed by spatial or temporal phase retrieval algorithms, and off-axis DHI systems require an extra step of processing to reconstruct the interferogram before finding the phase map. As a result of the shortage of software available in research-oriented environments, the procedure involves complex stages of data processing and requires advanced skills in data analysis. That was the primary motivation to develop an

easy-to-use software platform that is freely available to any users with or without expert knowledge in coding and algorithms.

- *Chapter 2*

Chapter 2 introduced PhaseWare, the software package that provides phase map retrieval for FPP and off-axis DHI systems based on the MATLAB platform. The package includes the most commonly used techniques and combines pre-processing, phase extraction, and post-processing in a pipeline architecture design and can generate reports for later use. The software design allows users to incorporate user-supplied algorithms (add-ons) at any stage. This ability to add custom algorithms allows users to adapt the software to suit their hardware circumstances, improve upon existing algorithms, and test new approaches. Chapter 2 provides examples for FPP processing and off-axis DHI processing. In addition, Chapter 2 provides links to the metadata of the software, including its codes and a user manual.

- *Major contributions*

The PhaseWare software package is the first comprehensive phase retrieval software for FPP and off-axis DHI. The software provides an easy-to-use graphical interface to several commonly used algorithms and techniques in the field of non-contact optical measurements. The software aims to simplify data processing and image reconstruction. PhaseWare can retrieve a phase map from a single image frame, thereby obtaining surface morphology of the imaged scene. It is also possible to track phase changes through a set of image frames to estimate deformation and motion.

Researchers who are experts and non-experts in the field of fringe pattern phase retrieval can use this software package. A new designed system or a new processing algorithm can be evaluated using this tool.

- *Limitations and Future Work*

PhaseWare only covers spatial phase retrieval algorithms (i.e., carrier-based algorithms) that require a single frame to produce a phase map. Single-shot applications can make use

of these algorithms but that could lead to error in the results. There is also a second type of algorithm called temporal phase retrieval, which uses a sequence of phase-shifted fringe patterns. Due to the requirement that the imaged scene must be motionless during fringe pattern collection, multi-fringe algorithms can only render static and semi-static scenes, albeit with much higher accuracy. In principle, a user could extend PhaseWare to include temporal phase retrieval algorithms thereby allowing users to better match the processing, based on the number of phase-shifted fringes in the input data and the inter-fringe phase step. In addition, adaptive phase step detection functions could be implemented for the retrieval of phase maps, especially in situations in which the phase steps between the fringes are uncertain or in error.

ESPI processing is not currently supported by the available version of the software, although it could be upgraded so it can handle ESPI data as well. Since ESPI systems provide speckle interferograms, the signals do not reveal any fringes which are needed by the phase retrieval algorithms in PhaseWare. Thus, in order to extract the phase map, speckle interferograms must undergo further processing to produce a correlation fringe pattern.

6.2.2 FPP

In Chapters 3 and 4, multispectral fringe projection profilometry (MFPP) has been introduced. This novel method consisted of multispectral illumination to project a multispectral composite pattern (MCP) onto an object and a multispectral camera to detect a reflection of the MCP off the object. Each MCP contained multiple fringe patterns that resemble the patterns that conventional FPP systems use (i.e., monochrome fringe patterns), but with the advantage that all patterns are simultaneously acquired. These features are particularly useful for dynamic objects when they need to be scanned with an FPP system.

- *Chapter 3*

The setup explained in this chapter enabled us to detect 8 unique monochrome fringe patterns representing 4 distinct directions in a single snapshot. For each direction, the

camera could detect two π -phase-shifted fringe patterns. Each pair of fringe patterns were used to compute a differential fringe pattern that corrects for illumination offsets and mitigated the effects of glare from highly reflective surfaces. This new multispectral method can solve many practical problems related to conventional FPP and doubles the effective spatial resolution. It is suitable for high-quality, fast 3D profilometry at video frame rates. However, the system uses carrier-based phase retrieval algorithms. As explained in Chapter 1, carrier-based algorithms produce lower quality phase retrieval when compared to multi-step phase-shifting algorithms. Therefore, the new MCP presented in Chapter 4 was designed to provide 4-step phase-shifting profilometry in a single shot.

- *Chapter 4*

In Chapter 4, a new multispectral composite pattern that included 4 monochrome fringe patterns in a single frame acquisition has been introduced. The 4 fringe patterns in this study were $\pi/2$ -phase-shifted with respect to one another. This property enabled me to use multi-step phase-shifting algorithms to retrieve a phase map. In this chapter, the technology was described, and its applicability was assessed experimentally. In addition, a pre-processing procedure based on the Lissajous figure normalization, adapted to 4-step phase-shifting, was introduced. The technique normalizes the distinct acquisitions in different spectral bands.

- *Major findings*

The technology introduced in Chapters 3 and 4 opens a new category of single-shot composite patterns for FPP called MCP. Composite patterns in FPP are used to increase the accuracy of 3D measurements or to speed up measurements by generating more fringe patterns in a shorter period of time. MCP could be a very effective solution to accomplish this goal. This system allows for robust imaging of dynamic objects since only one snap-shot image needs to be captured. Two different ways to compose different fringe patterns are discussed earlier; one for enhancing the results for carrier-based algorithms (spatial phase stepping algorithms), the other for enabling multiple-phase step algorithms (temporal phase stepping algorithms). This novel concept could also be

extended to generate a tailored composite pattern by combining multiple custom-shaped fringe patterns (e.g., fringe patterns in different directions, different phase shifts, different frequencies, or a combination of them).

CMP can expand the number of patterns in each CP without sacrificing dynamic range, which is a major problem with grayscale composite patterns. Using a multispectral camera for MFPP offers more color channels than RGB cameras which are limited to only 3 channels. With this, more patterns can be generated, and even particular color channels can be used such as infrared, for specific applications such as secure systems with invisible light pattern to illuminate the objects. In addition, the multispectral feature of the system guarantees the absence of leakage between the spectral bands, another problem for simultaneous phase-shifting with color cameras. With all these benefits, in addition to the fact that simple devices can be used to create an MCP, this new method can supersede the traditional composite pattern generation techniques. Also, since this system consists of no moving parts and is based on MEMS technology, it can be miniaturized for space-constrained applications, such as robotic surgery and imaging inside cavities.

- *Limitations and Future Work*

An issue with the two MCPs that are presented in this thesis is how they use strips as fringe patterns. For most applications, this type of fringe pattern provides weaker sampling than sinusoidal fringe patterns. The problem is most noticeable when the target for the measurement is an object with steep slopes with respect to the camera-projector's baseline. Increasing the number of spectra in the MFA would be one possible way of solving this problem. Another approach is to slightly defocus the MCP at the object plane. By doing this, the edges of the fringe pattern will be blurred, forming sinusoidal shapes.

There can also be an issue with multispectral cameras responding differently to different wavelengths like when the multi-step phase retrieval algorithms are used. This has the effect of generating a different background to different fringe patterns as well as adding

some offsets to phase shifting between the fringe patterns. This issue was addressed in Chapter 4 using adaptive normalization.

Finally, the narrow wavelengths of the MFA require an extremely bright light source to fully expose the camera. This issue can potentially be solved by using high-power pulsed LEDs.

6.2.3 Off-axis DHI

- *Chapter 5*

The approach taken in Chapter 5 transforms interferograms acquired with an off-axis DHI system into 3D representations of reflective objects. This approach is an illustration of PhaseWare's capabilities. We developed a silicon-etched lateral-axial resolution target based on a USAF design to evaluate the system. Photograph of the target along with a detailed diagram of the target are shown in Figure A-2 in Appendix A.

- *Major findings*

This algorithm permits the use of a digital holographic camera for non-destructive testing of surface morphology at nanometer scales. Additionally, it illustrates the steps in the processing algorithm intuitively.

- *Limitations and Future Work*

The study investigated only static objects. A more comprehensive study is illustrated in Appendix A, where the results of static and dynamic objects have been examined with a more optimized off-axis DHI setup but very similar to the setup used in the Chapter 5.

6.3 Conclusion

This work established a phase retrieval software (PhaseWare) that is compatible with FPP systems and off-axis DHI systems. The software can also perform off-axis DHI interferogram reconstruction. PhaseWare can extract a single phase-map from a single source frame to create a 3D surface profile of reflective objects or extract multiple phase-maps from multiple source frames to determine the displacements and deformations of

the objects. This software is the first to have the ability to provide phase retrieval from fringe patterns by several well-known algorithms in the literature, as well as all needed pre- and post-processing steps. Additionally, the user has the option of importing their own algorithms for every part of the software, allowing them to compare their new algorithms with those of known algorithms.

We have further developed a method for creating composite patterns using multispectral technology suitable for FPP systems. These patterns can easily be customized, and two different designs were developed and examined in this thesis. The first design composes four pairs of complementary π phase-shifted fringe patterns in different directions. Through this design and by using spatial phase stepping algorithms, the object surface can be sampled more efficiently, and the effects of glare reduced significantly. This design could be useful in biomedical imaging of eye structures that have highly reflective surfaces. However, it is essential for eye imaging applications to include appropriate invisible spectrums to protect the eyes from any potential damaging. The subsequent design was composed of a pattern that consists of four phase-shifted straight fringe patterns. Through this pattern, temporal phase stepping algorithms could be used using only one frame. This class of algorithm could provide more accurate and pixel-wise phase maps with lower reliability to the fringe quality, the problems with the spatial phase stepping algorithm. This new design could be beneficial for biomedical applications requiring accurate dynamic 3D imaging while the objects are rough and may obscure the camera field-of-view by shadows and the light quality may be inadequate to provide high-quality fringe patterns. Our system offers significant advantages over the existing single-frame FPP systems, such as a higher dynamic range for individual fringe patterns (compared to methods using grayscale multiplexing), and isolation between different fringe patterns in case of leakage (compared to methods using color cameras). Additionally, our designs each can provide four fringe patterns at the time (the first design can provide four pairs of fringe patterns in four different directions, and the second can provide four phase-shifted fringe patterns in one direction), which is one extra pattern compared to similar methods based on RGB color patterns. Furthermore, the idea of the multispectral fringe projection profilometer could yield more fringe patterns and

more complex composite patterns by utilizing more spectral channels in the filter array and the camera.

Appendix A

Dynamic surface tracking with off-axis digital holographic interferometry

This appendix describes the surface tracking capability for off-axis digital holographic interferometry (DHI) system. The DHI system was based on the setup explained in the Chapter 5 and the results were processed with PhaseWare (explained in Chapter 2). DHI was built by Hui Wang, who also collected the raw data.

- Setup

The system was comprised of a laser with long coherence length, a large-format camera, and an interferometer based on a Mach-Zehnder design. The He-Ne laser (Thorlabs, HNL 100L) featured an output wavelength of 632.8 nm and a coherence length of 200 mm. The laser output beam was 1.5 mm in diameter at 10 mW power. The camera head (IO Industries, Flare 48M30-CX) featured a large CMOS sensor with 7920×6004 pixels (47.5 MP) at a pixel pitch of 4.6 μm in each direction. The total sensor area was 36.4 mm \times 27.6 mm (45.7mm in diagonal). The field of interest (FOI) was adjustable and could be varied from a full field of view to several pixels. Under free run conditions, the camera provided 23 frames per second (FPS) at full field of view. Notably, faster recording up to 120 FPS was available by selecting a region of interest (ROI) at the expense of lower spatial resolution. Video recording capabilities were provided by a digital video recorder (IO Industries, DVR Express Core 2).

- Phase demodulation algorithm:

An interferogram is formed by the interference between the wave fronts in the object and reference arms and is digitally sampled by a camera. The interferogram encodes phase information as well as density information that can be decoded with a phase retrieval algorithm. Interferometry off-axis introduces a spatial carrier frequency fringe pattern from the small angle between the reference arm and the object. In this case, a single

interferogram could reveal sufficient data to determine the phase-map, similar to FPP systems. The phase-map contains morphological information about the object surface. One phase-map can provide a 3D profile of the surface while a sequence of phase maps for a non-stable object can be used to measure the displacement and deformation of the surface. Figure A-1 shows a flowchart of the algorithm that was used to compute phase-maps for the off-axis interferometry measurements. The algorithm consisted of low-level steps (boxes with solid lines) that when combined, provided higher-level functions (dashed boxes). The algorithm began with a raw interferogram collected directly from the camera, a reference interferogram, the laser wavelength, and the distance between the object and the camera. The reference interferogram was captured beforehand from a flat surface and was used to suppress effects of the optical defects and non-uniformity in the illumination in the processed interferograms. The interferogram was cropped, followed by removal of the DC offset, and zero-padded to optimize the pixel size in the reconstruction [40]. Afterward, Fresnel transform reconstruction was performed, which included extraction of the phase and the amplitude of the interferogram based on the single FFT reconstruction method [41,42]. After cropping the focused part of the reconstructed data, for the prepared example the focused part is the real image, it is possible to wrap the phase, estimate the carrier phase, and unwrap the phase to get the absolute phase value for the object. Defects in the optical equipment and illumination nonuniformities affected the measured phase-maps and were corrected by subtracting the unwrapped phase map acquired for the reference interferogram from the unwrapped phase map acquired for the object. The final corrected unwrapped phase map was then used to visualize the object surface in 3D.

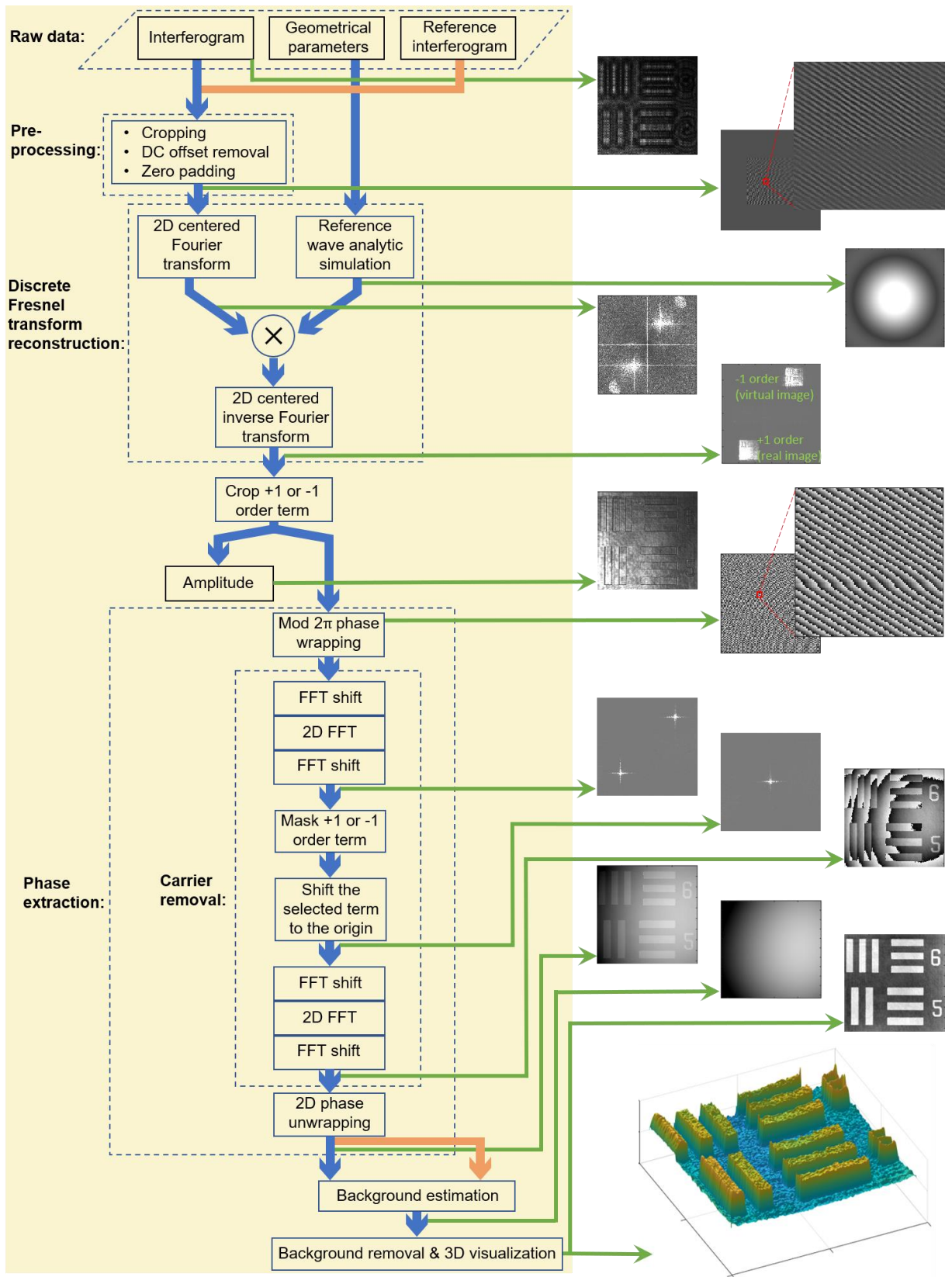


Figure A-1: Flowchart of the phase demodulation algorithm (left) with example data (right). Green arrows indicate step at which example data is obtained. The algorithm contains 4 high level functions, including pre-processing, reconstruction, phase extraction, and carrier removal (indicated as dashed boxes).

- Evaluation of surface profile and deformation

Three types of experiments were carried out in order to evaluate the approach and estimate its accuracy in an open environment. First, we designed a reflective resolution target, aiming to assess the ability to distinguish the minimum surface topography. Afterwards, we further tested the approach by investigating the dynamic movement on a scattering phantom surface, because in a realistic application the measured surface is usually not optical smooth and difficult to maintain in a static state. The last experiment was carried out for the purpose of monitoring fast motion on a scattering surface.

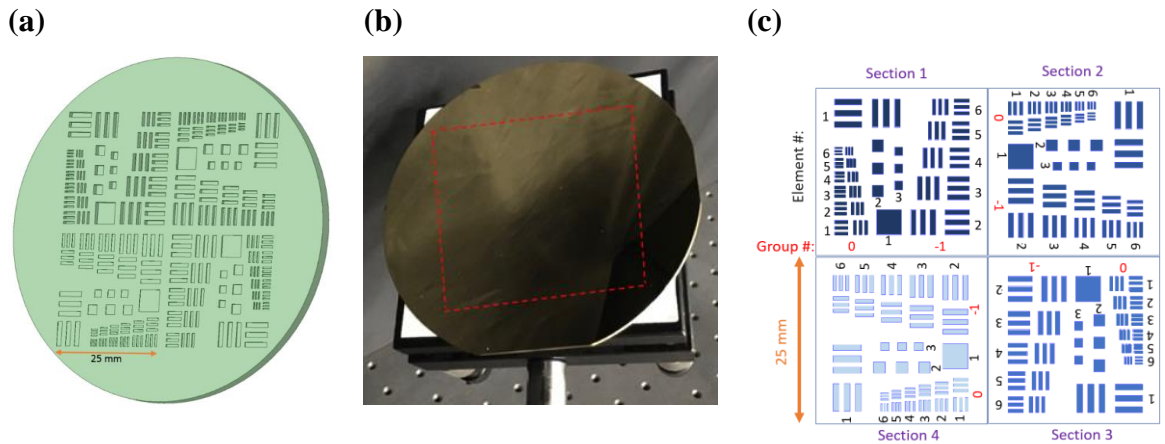
1. *Measurements of surface profile*

Lateral and axial resolution was estimated by using a custom 1951 United States Air Force (USAF) resolution target. The target was fabricated on a 4-inch silicon wafer (1- μm thick thermal silicon oxide layer). Surface patterns were created by photolithography and reactive ion etching on the thermal silicon oxide surface. The process was repeated a total of 4 times to generate one pattern in each quadrant of the wafer. The amount of etching was different for each quadrant, resulting in etch depths of 10, 33, 82, and 123 nm. Afterward, 100 nm of gold was deposited on the surface of the patterned silicon wafer with electron beam physical vapor deposition (EB-PVD). Manufacturing accuracy for this target was 6 nm axially and 500 nm laterally. The manufacturing of this product was performed by Spectral Devices Inc., London, Canada.

The target was designed to have an optical smooth surface that equally divided into four symmetrical areas (Figure A-2 (a) and (b)). The location and indication of the bars and squares is shown in Figure A-2 (c). For example, the six bars located in the bottom-left of Section 1 are marked (G0, E1), where G is the group number and E the element number. Each section contained several groups of elements with different widths (Figure A-2 (d)).

Light reflected from the non-etched surface (i.e. 0 nm depth) had a phase difference compared to that of light reflected from the etched areas. We assessed the performance of the holographic interferometer and the reconstruction algorithm by measuring the phase changes and knowledge of the etch depth.

The resolution target was mounted on a 3-axis stage. The center of the target was illuminated by the object beam over an area approximately 50 mm in diameter. Since each patterned quadrant measured 25 mm×25 mm, the illumination coverage enabled full field imaging on a complete section. The camera exposure was 1 ms and full frame images (48MP) of each section were collected.



(d)

Element #:	Width of each element (μm)			Section #:	Depth of each section (nm)
	Group -2	Group -1	Group 0		
1	5000	1000	500	1	123
2	2000	891	445	2	82
3	1500	794	397	3	33
4		707	354	4	10
5		630	315	Background	0
6		561	281		

Figure A-2: Resolution target for measuring the axial and lateral resolution of an interferometer system. (a) Schematic of the target. (b) Photograph of the target on a stage. (c) Pattern of etched areas (Section 1: 123 nm; Section 2: 82 nm; Section 3: 33

nm; Section 4: 10 nm; and Background: 0 nm). (d) Table of feature sizes measured as the smallest in-plane dimension.

The reconstruction algorithms were subsequently applied to the holograms that acquired by our optical assembly. The reconstruction results of the holograms acquired from each quadrant along with the evaluation of the axial and lateral resolution can be appreciated in Figure A-3. To increase the computer processing speed, the hologram images were cropped to the size of the patterns. After reconstruction, each 2D visualization featured a wide field of view that measured 25mm in both x and y dimensions. It should be pointed out that the original raw image has a full field of view, almost twice the size as the one depicted in Figure A-3 (a). The axial resolution, which is the minimum depth that can be distinguished by the system from the background, i.e. the target surface, to the very bottom of the etched pattern was depicted in Figure A-3 (a). Here we only report on the evaluations of the three parallel bars located at coordinate (G0, E1) on each quadrant. In Figure A-3 (a), the two dimensions height maps in the short dash lines box illustrate the bar depth that was obtained from the reconstructed 3D surface map originating from the holograms. The red solid lines show the section where the presented height profile was taken from. The red dotted lines indicate the designed depth value.

To evaluate the system's lateral resolution, the width of elements on each quadrant were assessed and are compared with their corresponding deviation value in the error bars presented in Figure A-3 (b). The elements in each group, including the gap between two adjacent elements are numerally reconstructed. Here we randomly picked elements with coordinates at (G-1, E1) and (G0, E6) on each quadrant (examples in green elliptical circle in Figure A-3 (a)) for illustration. In each element, ten widths were calculated, including six elements and four intervals. Error bars in Figure A-3 (b) show the results from measuring the full width at half maximum (FWHM) and the corresponding expected values on each quadrant, which are 1000 μm and 281 μm , respectively.

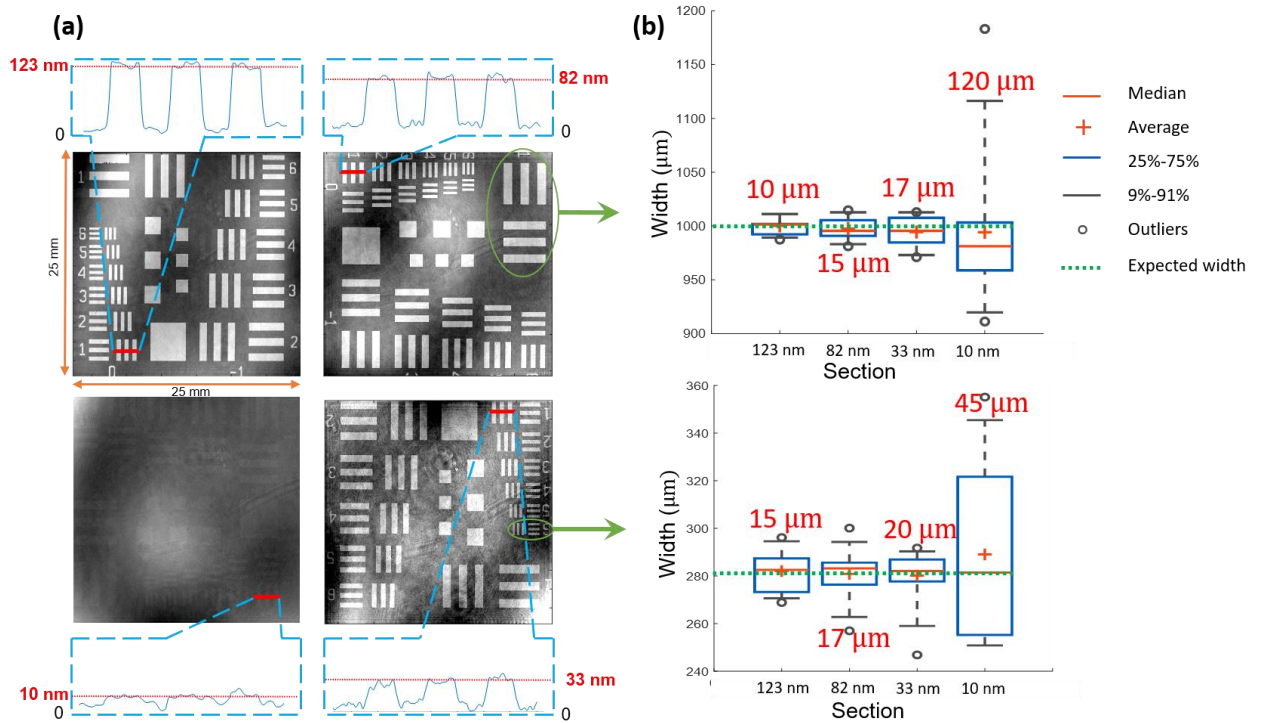


Figure A-3: Scanned reconstruction for the target with the DHI system. a) Shows four reconstructed phase maps corresponding to the four different sections in the USAF target. Four line-profiles indicating the phase information for the same group of elements in the four different sections are shown. b) Shows two examples of the FWHM measurements for the element 1, group -1 (with the width = 1000 μm) and element 6, group 0 (with the width = 281 μm).

2. *Measurements of dynamic out of plane displacements on a scattering surface*

Many objects feature a rough surface, which scatters the object beam and makes detection of the reflected light challenging. To test our system on a scattering surface, we manufactured a polydimethylsiloxane (PDMS) phantom. The phantom consisted primarily of 1% Intralipid™ (Fresenius Kabi Canada Ltd.). A piezoelectric speaker was placed centrally near the bottom of a cylindrical container with the active surface facing upward. Approximately 50 ml liquid was poured into the container and left undisturbed at room temperature for 48 h to cure. The cylindrical shape PDMS phantom measured 85 mm in diameter and had a thickness of 20 mm (Figure A-4). The phantom was positioned

with its top surface perpendicular to the incident object beam. A function generator was connected to the speaker to send continuous signals that evoked surface deformations. Different frequencies and voltages were applied to investigate the relationship between amplitude, frequency, and displacement.

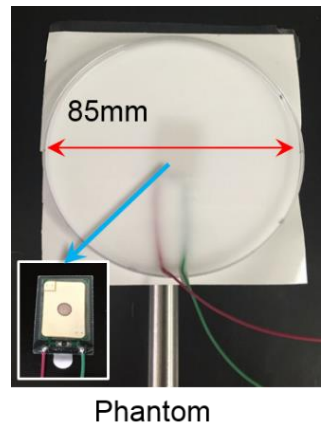


Figure A-4: Phantom for dynamic displacement measurement experiment

The system's behavior of monitoring dynamic displacement that carried out on a PDMS phantom surface is manifested in Figure A-5. The displacements were evoked by an imbedded piezoelectric speaker, which was further driven by a function generator. Figure A-5 shows the measurement results from experiments where the function generator produces five different voltages at three different frequencies. The results basically show displacement tracking from a single pixel located in the center of the surface that moved along the optical axis.

An amplitude and frequency analysis were conducted by fitting sinusoidal curves to the measured displacement signals. The figure shows red colors representing measured signals and blue colors representing fitted sinusoidal curves. In the below part of the figure, the sinusoidal curves' value for frequency and amplitude (peak) are printed in blue.

The results clearly show that the amplitude of the displacements is proportional to the voltage of the function generator. The higher voltages may also cause the displacements to wrap. Since we used a laser with a wavelength of 632.8 nm, displacements close to

half of this value can cause wrapping. Wrapping is visible in the top-left panel (i.e., 1 Hz and 8 V) as well as the one below that (i.e., 5 Hz and 8 V). Decreasing the voltage reduces the amplitude. The lowest amplitude that was successfully detected was 7.3 nm, which corresponds to panel 1 Hz, 1 V. Results indicate that at the same voltage, a higher frequency produces smaller amplitude. That makes sense since the signal generator is able to give the signal with lower frequency more energy. For this reason, the curve fittings fail since the displacements of the signal generator with 1 V for 5 Hz and 10 Hz are smaller than the sensitivities of our system.

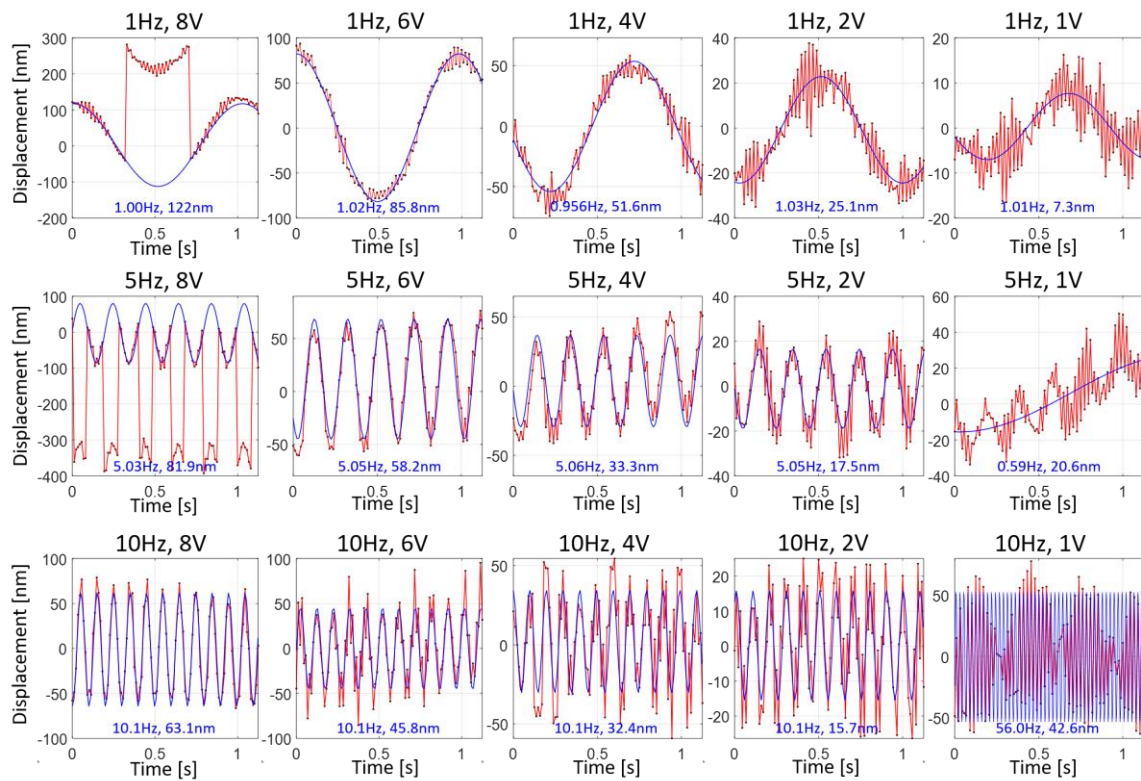


Figure A-5: Dynamic displacement measurement. shows fifteen examples the measured displacement for a single pixel of the camera (at the center of the field of view) by changing the piezoelectric power and frequency (1 Hz, 5 Hz, and 10 Hz). Power was controlled by adjusting the waveform amplitude from 1 to 8 volts.

3. *Measurement of fast transient out of plane waves on a scattering surface*

Fast occurring events on a scattering surface can occur when an object experiences external force. We carried out an experiment to record the fast transmission of a waveform on a scattering surface. Approximately 500 ml of Intralipid was poured into a container that had dimensions of 118 mm \times 91 mm \times 57 mm. The piezoelectric speaker was attached centrally to the longer side of the box. The object beam illuminated the liquid surface. Scattered light was collected with a large rectangular mirror placed facing the beam splitter 1 at a 45° tilt (Figure A-6). Light was projected on to the center of the surface so that the disturbance from the waves that bounced back from the side walls did not affect the measured waveforms. A single pulse was sent to evoke a waveform that propagated from the speaker to the other side of the tank. The camera was triggered by the pulse and automatically stop after 1s. The experiment was run for different frequencies and voltages. The circle in Figure A-6 roughly indicates where the illumination beam is. Waves originating from the piezoelectric speaker will travel along the arrow direction.

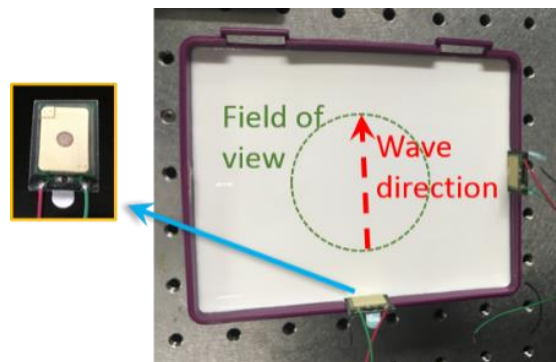


Figure A-6: Phantom for transient wave detection experiment (right). Piezoelectric speaker (left)

Figure A-7 summarizes the results of recording non-periodic transient events on a scattering surface. Figure A-7 (a) shows the reconstructed height map of the red dashed line indicated in Figure A-6. In Figure A-7 (a), the wave peak appeared in four frames, indicated out by the yellow arrows. To facilitate with easy visualization, the 3D map of

waveform transmission can be appreciated in Figure A-7 (b). Likewise, the arrows indicated the same wave peak captured in different frames, which was a strong evidence showing the system's ability to record fast events with nanometer-scale displacement.

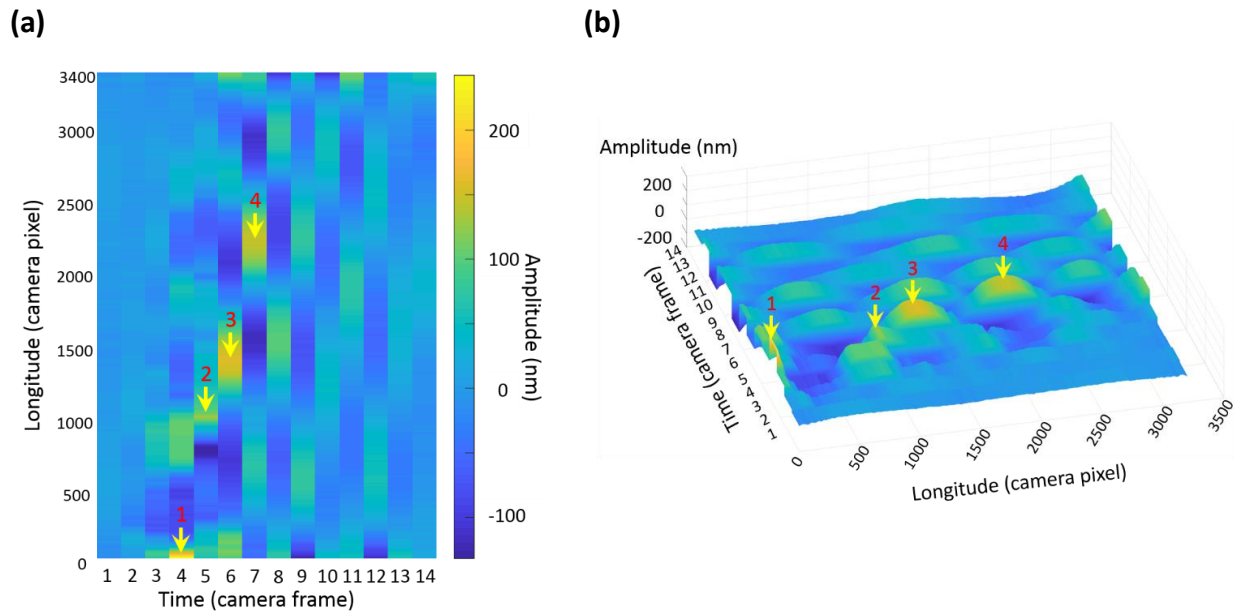


Figure A-7: The transient wave detection. a) A transient wave measured along a path corresponding to the red dashed line in Figure A-6. The x-axis indicates the time axis, y-axis indicates the camera pixel along the path, and the color indicates the amplitude of the displacement. b) A 3D visualization of the transient wave measured with the system for different times corresponding to panel (a). The x-axis indicates the camera pixel, the y-axis indicates the time axis, and the z-axis indicates the amplitude. Color scale identical to color scale in panel (a).

- [1] Yuchen Zhaoa, Redouane Zemmamouche, Jean-François Vandenrijt, Marc P. Georges, “Accuracy concerns in digital speckle photography combined with Fresnel digital holographic interferometry” *Optics and Lasers in Engineering*, 104:84-9, (2018).
- [2] P. Omid, H. Wang, M. Diop, J.J.L. Carson, “Algorithm for phase-displacement conversion from reflection digital holographic interferometry” In *Practical Holography XXXIII: Displays, Materials, and Applications*, vol. 10944, p. 109440Q. International Society for Optics and Photonics (2019).
- [3] A. Verrier, Nicolas, “Off-axis digital Hologram reconstruction: some practical considerations,” *Appl. Opt.*, vol. 50.34, p. H136–H146., (2011).

Curriculum Vitae

Name:	Parsa Omidi
Post-secondary Education and Degrees:	<p>University of Isfahan Isfahan, Iran 2007-2011 B.Sc.</p> <p>Iran University of Science & Technology Tehran, Iran 2012-2015 M.Sc.</p> <p>The University of Western Ontario London, Ontario, Canada 2016-2021 Ph.D.</p>
Related Work Experience	<p>Teaching Assistant The University of Western Ontario 2016-2020</p> <p>University of Isfahan 2009-2011</p>

Publications:

P. Omidi, M. Najiminaini, M. Diop, and J.J.L. Carson. "Single-shot detection of 8 unique monochrome fringe patterns representing 4 distinct directions via multispectral fringe projection profilometry" *Scientific Reports*, (2021).

P. Omidi, L.C.M. Yip, H. Wang, M. Diop, and J.J.L. Carson. "PhaseWare: Phase map retrieval for fringe projection profilometry and off-axis digital holographic interferometry" *SoftwareX*.13, 100652, (2021).

P. Omidi, M. Najiminaini, M. Diop, J.J.L. Carson. "Single-shot 4-step phase-shifting multispectral fringe projection profilometry" *Optics Express*, (2021) **[submitted]**.

B.G.H. Janssen, M. Najiminaini, Y. M. Zhang, **P. Omidi**, J.J.L. Carson.

"Multispectral Intravital Microscopy for Simultaneous Bright-field and Fluorescence Imaging of the Microvasculature" *Applied Microscopy*, (2021).

P. Omidi, M. Zafar, M. Mozaffarzadeh, A. Hariri, X. Haung, M. Orooji, and M. Nasiriavanaki. "A novel dictionary-based image reconstruction for photoacoustic computed tomography" *Appl. Sci.* 8 (9) 1570, (2018).

P. Omidi, H. Wang, M. Diop, and J.J.L. Carson. "Algorithm for phase-displacement conversion from reflection digital holographic interferometry" *Practical Holography*

XXXIII: Displays, Materials, and Applications. Vol. 10944. International Society for Optics and Photonics, (2019).

L. C. M. Yip, **P. Omid**, I. Kosik, A. Chamson-Reig, M. Brackstone, and J. J. L. Carson. "Development of a scanning photoacoustic tomography system for tumor margin assessment in breast conserving surgery" Advanced Biomedical and Clinical Diagnostic and Surgical Guidance Systems XVII. Vol. 10868. International Society for Optics and Photonics, (2019).

H. Wang, **P. Omid**, M. Diop, and J.J.L. Carson. "Holographic camera for non-contact measurement of nanoscale surface heights" Practical Holography XXXIII: Displays, Materials, and Applications. Vol. 10944. International Society for Optics and Photonics, (2019).

P. Omid, M. Diop, J.J.L. Carson, and M. Nasiriavanaki. "Improvement of resolution in full-view linear-array photoacoustic computed tomography using a novel adaptive weighting method" Proc. SPIE 10064, Photons Plus Ultrasound: Imaging and Sensing (2017).

A. Hariri, **P. Omid**, and M. Nasiriavanaki. "Resting-State Functional Connectivity Measurement in the Mouse Brain using a Low-Cost Photoacoustic Computed Tomography" in Frontiers in Optics (2016).